UNIVERSITÀ DI PARMA

DOTTORATO DI RICERCA IN
"FISICA"

CICLO XXX

Synchronization, heterogeneity and inhibitory hubs in neural networks with synaptic plasticity

Coordinatore:
Chiar.mo Prof. Cristiano Viappiani

Tutor:
Dr. Alessandro Vezzani

Dottorando: Elena Bertolotti

Anni 2014/2017

Synchronization, heterogeneity and inhibitory hubs in neural networks with synaptic plasticity

Ph.D. thesis
University of Parma

Candidate: Elena Bertolotti
Coordinator: Prof. Cristiano Viappiani
Tutor: Dr. Alessandro Vezzani

February 2018

A thesis submitted in partial fulfillment of the requirements for the degree of Doctor of Philosophy in Physics.
Thesis not yet defended.

Version: February 5, 2018
Author's email: elena.bertolotti1@fis.unipr.it

"Marco Polo descrive un ponte, pietra per pietra.

- Ma qual è la pietra che sostiene il ponte? - chiede Kublai Kan.

- Il ponte non è sostenuto da questa o quella pietra, - risponde Marco, - ma dalla linea dell'arco che esse formano.

Kublai Kan rimane silenzioso, riflettendo.

Poi soggiunge: - Perché mi parli delle pietre? È solo dell'arco che mi importa.

Polo risponde: - Senza pietre non c'è arco."

Italo Calvino, "*Le città invisibili*"

Preface

The work presented in this dissertation was carried at the Department of Mathematical, Physical and Computer Sciences at the University of Parma from November 2014 to October 2017, under the supervision of Alessandro Vezzani, in collaboration with Raffaella Burioni.

Chapter 4 is based on a paper in preparation.

Chapter 5 is the result of a collaboration with Matteo di Volo (Post doc, CNRS, France) and it is based on a recently pubblished paper:

> *Bertolotti E., Burioni R., di Volo M. & Vezzani A. (2017). Synchronization and long-time memory in neural networks with inhibitory hubs and synaptic plasticity. Physical Review E, 95(1), 012308.*

All the results presented in this work have been obtained through numerical simulations of an original C++ code. The graphic elaboration of data and plots has been performed with MATLAB software.

Abstract

How brain can perform highly specialized and differentiated functions at the same time, generating collective dynamics among its elements, is a very intriguing question. From the point of view of Statistical Physics, brain is the complex system by definition, since we cannot explain its macroscopic behaviour as a simple sum of its microscopic units dynamics.

Within this system, a phenomenon which largely affects brain functions is synchronization. Synchronization is one of the most fundamental and surprising dynamical states, observed in oscillatory systems belonging to many different research branches, such as engineering, physics, chemistry, life sciences and social life. In particular, in neural tissues, synchronization emerges as collective oscillations, where all units of a macroscopic population evolve in a coherent way. In recent years great efforts have been performed in experimental and theoretical neurosciences to interrelate the synchronous regimes detected in different brain areas with specific cognitive functions, such as memory and learning processes, but also with neural pathologies. The onset of synchronous phases has been shown to depend on many factors, such as the connections structures and the presence of inhibitory components.

Due to their high complexity, numerical simulations of neural networks are able to correctly reproduce the collective phases detected in real neuronal ensembles, providing an useful investigation method to advance predictions about the dynamical properties of neural tissues, which have to be experimentally tested.

In this framework, in this thesis we investigate theoretically and numerically the role played by heterogeneity and the interplay between inhibition and connectivity structure, in defining synchronization properties and the capacity of storing information of a neural population. As a model of neural network we consider a system of integrate-and-fire neurons coupled through a synaptic mechanism characterized by a short-term plasticity. Since all neurons are identical units, the only source of heterogeneity will be encoded by the connectivity pattern. In particular, we take advantage of a mean field formulation of this model, which allows us to preserve the structural heterogeneity of our systems and it turns out to be extremely efficient in reproducing the dynamics of the model in the limit of large connectivity. Furthermore, to emphasize the role of heterogeneity, we introduce a single-site degree correlation, setting the same input and output connectivities for each neuron.

In the purely excitatory case, as synaptic coupling strength increases, a synchronization phase transition occurs from a quasisynchronous regime to an asynchronous one, while increasing the connections heterogeneity makes in general the network less synchronizable. However, considering broad distributions is not the only determinant factor in driving the networks synchronization, as clearly appears in scale-free topologies. Indeed, a "Gaussian synchronization condition" emerges: in order to have a synchronizable network the degree distribution peak should be high enough, that is it should contain enough neurons with similar degrees.

In an excitatory and inhibitory networks, where in particular inhibitory neurons are highly connected (hubs), we tune the fraction of inhibitory neurons present in the system and their connectivity level. What clearly emerges is that the hub character of inhibitory neurons is a fundamental ingredient to produce a highly synchronous regime in correspondence of an inhibitory fraction equal to 10-30%, which is the experimentally observed range of values. Furthermore, around this regime of complete synchronization we find an interesting metastable dynamical phase, which show long-time memory of external inputs applied to the network.

Contents

List of Figures v

Introduction and motivations 1

1 Synchronization in coupled self-oscillatory systems 5
1.1 What is synchronization? . . . 5
1.2 Historical notes and known examples . . . 6
1.3 Preliminary concepts . . . 7
1.4 Two simple case studies . . . 9
1.5 Systems of N coupled oscillators . . . 12
1.6 The Kuramoto model . . . 12

2 Synchronization in neuroscience 17
2.1 Elements of neural systems physiology . . . 17
2.2 Experimental measures of neural activity . . . 22
2.3 Synchronization evidences in experimental neuroscience . . . 24
2.4 Synchronization on computational neuroscience . . . 29

3 Dynamics of neural networks with synaptic plasticity 33
3.1 Defining our neural network . . . 33
3.2 Single neuron dynamics (LIF model) . . . 36
3.3 Short term synaptic plasticity (TUM model) . . . 39
3.4 Neural dynamics with finite connectivity . . . 42
3.5 Heterogeneous mean field formulation with single-site degree correlation . . . 45

4 The role of heterogeneity in driving synchronization 53
4.1 The paradox of heterogeneity on neural networks . . . 53
4.2 Simple case: synchronization transitions with Gaussian degree distribution . . . 54
4.3 Synchronization transitions with power law degree distributions . . . 60
4.4 Modified power law degree distributions . . . 63
4.5 An homogeneity constraint . . . 66

5 The role of inhibitory hubs in driving synchronization 73
5.1 Inhibitory component and hubs in neural networks . . . 73
5.2 Synchronization effect of inhibitory hubs . . . 75
5.3 Balance regime . . . 78
5.4 Long-time memory after an external stimulus . . . 81

General conclusions 87

Appendix A A short introduction to graph theory and complex networks 91

Appendix B Master stability function approach 105

Appendix C More about the Kuramoto model **107**

Appendix D Beyond the heterogeneous mean field formulation **115**

Bibliography **121**

List of Figures

1.1 Example of a limit cycle . . . 7
1.2 Example of a self-sustained oscillator . . . 8
1.3 Synchronization and phase-locking . . . 9
1.4 Example of Arnold tongues . . . 10
1.5 Beating regime . . . 11
1.6 Kuramoto model for phase oscillators . . . 14
1.7 Kuramoto transition form asynchronous to synchronous regime . . . 15

2.1 Different types of neurons . . . 18
2.2 Action potential of a neuron . . . 19
2.3 Chemical synapse . . . 20
2.4 Firing patterns of a neuron . . . 22
2.5 First human EEG tracing . . . 23
2.6 Brain oscillations . . . 25
2.7 Neural synchronization detections at different spatial scales . . . 26
2.8 Synchronization patterns in cortical areas of awake cats . . . 27
2.9 Synchronized 'up' and 'down' states of striatal spiny neurons . . . 28
2.10 Phase and inter-spike interval of a neuron . . . 30

3.1 Connectivity patterns of a cortical column . . . 34
3.2 Example of a raster plot . . . 35
3.3 The Hodgkin-Huxley model for single neurons . . . 37
3.4 LIF model for single neurons . . . 38
3.5 TUM model for short term synaptic plasticity . . . 40
3.6 Partial synchronization in a network of excitatory LIF neurons with short term synaptic plasticity . . . 46
3.7 Partial synchronization in a network of excitatory and inhibitory LIF neurons with short term synaptic plasticity . . . 49

4.1 Partially synchronous and asynchronous dynamics for a Gaussian distribution . . . 56
4.2 Synchronization properties for a Gaussian distribution as a function of the coupling . . . 57
4.3 Synchronization phase transitions for a Gaussian distribution as a function of its heterogeneity . . . 58
4.4 Gaussian distribution with positive and negative connectivity . . . 59
4.5 Synchronization transitions for power law distributions as a function of the coupling . . . 62
4.6 Synchronization phase diagram for power law distributions . . . 63
4.7 Power law distributions with a different initial cutoff . . . 64
4.8 Gaussian distribution with a power law tail . . . 67
4.9 Synchronization phase diagram for Gaussian + power law distributions . . . 69
4.10 Synchronization transitions for Gaussian + power law distributions as a function of the coupling . . . 70

5.1 Double Gaussian distribution . . . 76
5.2 Raster plots and $\langle ISI_k \rangle$ for a double Gaussian distribution with excitatory and inhibitory neurons . . . 77
5.3 Synchronization phase transitions for a double Gaussian distribution with excitatory and inhibitory neurons . . . 78
5.4 Weights of the E and the I component in driving the dynamics . . . 80
5.5 Metastable partially synchronous state . . . 81
5.6 A synchronizing external stimulus on an excitatory and inhibitory network . . . 82
5.7 Transient dynamics at the stimulus offset . . . 83
5.8 Response of the network to external stimuli applied at different times and with different intensity. . . . 85

A.1 Representation of a directed, undirected and weighted graphs . . . 93
A.2 Examples of undirected graphs . . . 97
A.3 Watts-Strogatz model . . . 100
A.4 Small-world graph properties . . . 101
A.5 Barabási-Albert model . . . 103
A.6 Degree distribution for the BA model . . . 103

B.1 Master stability function . . . 106

C.1 Bifurcation of the Kuramoto model . . . 112
C.2 Synchronization transition in SW networks . . . 113

D.1 Comparison between the finite connectivity and the HMF dynamics . . . 116
D.2 Stability of the synchronous state in finite connectivity simulations . . . 118
D.3 Dynamics of finite connectivity networks after the application of an external stimulus . . . 119

Introduction and motivations

How can neural ensembles of our brain, made of neurons, synapses and few other relatively simple elements, give rise to complex physiological and cognitive functions? How can highly similar anatomical structures produce an extremely wide range of tasks, necessary for life, from voluntary or involuntary movements of muscles to the continuous decoding of external sensory stimuli? And how can the same neural assemblies, present in the brain for instance in primates, at variance of them, provide us consciousness or allow us to observe reality, to interpret and represent it, filtering it through our senses and creating masterpieces, such as for instance amazing frescoes, musical components, poems or the Standard Model Lagrangian? Finding answers to these questions is probably one of the most intriguing researches for neuroscientists, far from being completed. From the point of view of Physics and especially of Statistical Physics, this issue is what makes brain the complex system by definition, since we cannot even hope to explain its macroscopic behaviour as a simple sum of its microscopic elements dynamics.

In this context it has been observed and proved in many ways that synchronization is a phenomenon which largely affects brain functions [1]. Synchronization is one of the first nonlinear effects in systems of coupled oscillators and one of the most fundamental dynamical patterns, since it emerges in many different fields of science, such as in engineering, physics, chemistry, life sciences and medicine, economics and social life [2]. Many features of our every day life are related to synchronous events, although we are not aware of it: synchronization processes among different electronic devices (smartphones, tablets or computers) through an Internet connection, synchronization directives among threads on a parallel computing algorithm or synchronization of peacemaker heart cells. Beyond these dissimilar examples, the common factor which emerges is that in oscillatory systems synchronization always appears through collective oscillations, where all units evolve in a coherent way.

Since neurons are intrinsically oscillatory objects, due to the fact that they periodically produce electrical signals, called action potentials, and then reset, we expect that any neural ensemble, which consists of neurons coupled through synapses [3], may display synchronous patterns. The persistent interchanges of these electrical inputs or impulses among neurons, which continuously receive, process and send them, give rise to the fundamental electrical activity, at the base of any brain mechanism and function. Actually, in recent years great efforts have been performed in experimental and theoretical neurosciences to try to interrelate synchronous signals detected in different brain areas with specific cognitive functions, such as memory [4] and learning processes [5], but also with neural pathologies and disorders states, such as epileptic seizures or Parkinson's disease [6]. In the future, a better understanding of these synchronization phenomena might also provide suggestions or methods for treating these diseases. The onset of synchronous phases has been shown to depend on many factors and among them the connections structures, as the emergence of scale-free topologies or small-world connectivity patterns [7] or the presence of hubs (neurons with a large number of connections [8]), and the presence of inhibitory components, in particular in the dynamics of inhibitory interneurons [9], seem to play a fundamental role.

Due to the high complexity of these neural systems, numerical simulations of neural networks, more or less realistic from the biophysical point of view, appear as an useful investigation method, to advance predictions about the dynamical properties of neural tissues, which have to be experimentally tested. Through mathematical models which describe the dynamics of neural elements, as neurons, synapses and action potentials, neural networks are able to reproduce the collective activity of a neural population. Their strength is that in most cases it is not really necessary to consider very details biological models, highly dimensional or exact in capturing the microscopic behavior of each cells, but rather simple mathematical equations serve the purpose.

In this thesis we focus mainly on two main goals. First, we investigate theoretically and numerically the role played by the heterogeneity in driving the synchronization properties of the network and, more precisely, the phase transitions from synchronous to asynchronous regimes. Then, we add to the system an inhibitory component to discuss the interplay between connectivity structure and inhibition in defining synchronization and functional properties of the neural population.

As a model of neural network we consider a system of integrate-and-fire neurons coupled through a synaptic mechanism characterized by a short-term plasticity [10], on random uncorrelated networks. Such a model shows a wide range of dynamical configurations and it has been especially designed from the beginning to describe the dynamics of neurons of the cortical columns, which are the main neural populations of the cerebral cortex, the largest external part of the brain. Since all neurons are identical units, the only source of heterogeneity of our networks will be encoded in the connectivity pattern, that is in the number of connections (degree) of each node. Therefore a network will be termed heterogeneous if it includes nodes with very low and very high degree. In particular, we take advantage of a mean field formulation of this model, called heterogeneous mean field (HMF), which has been initially introduced for epidemic dynamics in social network [11] and recently applied on this model of neural network [12]. This approach lets us preserve the structural heterogeneity of our systems and it turns out to be extremely efficient in correctly reproducing the dynamics of networks in the limit of large system size (numbers of neurons) and especially of large connectivity.

The HMF allows us to directly control the heterogeneity in the network connectivity through the width of the probability distribution function for the nodes degree, so that broader distributions will correspond to higher heterogeneity. For instance, for Gaussian degree distributions the heterogeneity is tuned by the standard deviation, while for scale-free distributions by the exponent of the power law.

Furthermore, in order to emphasize the role of heterogeneity, we introduce a single-site degree correlation for all neurons, setting the amount of nodes from which a neuron receives action potentials equal to the amount of nodes to which it sends its impulses.

In purely excitatory networks, that is in networks with only excitatory neurons, we see how the heterogeneity in the network connectivity strongly influences network synchronization. In general, as expected [13], an increase of heterogeneity makes the network less synchronizable. However, especially if one wants to consider scale-free topologies, the heterogeneous character of the system is no longer sufficient, but other factors seem to drive synchronization transitions: from one side the distribution peak should be well separated from $k = 0$, on the other side it should be high enough, that is it should contain enough neurons with similar degrees.

If we further consider inhibitory neurons, in addition to the excitatory component, the synchronization scenario is even more complex. In these excitatory and inhibitory networks, we investigate not only synchronization transitions but also a functional property of the system and more precisely how the system processes external inputs. In order to discuss the cooperation between heterogeneity and inhibition, inhibitory neurons are also hubs, since they have a number of links much higher than the average connectivity, and we can tune how many inhibitory neurons are present and how strong is their hub character, that is their relative connectivity with respect to the rest of the network. As a function of these two main parameters we observe a wide range of dynamical configurations, from quasisychronous to totally synchronous and asynchronous states. In particular, for a specific fraction of hub inhibitory neurons the network displays interesting balance regimes and highly metastable states, which are highly efficient in storing information about external stimuli applied to the network.

The thesis is organized as follows. In the first Chapter we give a brief introduction to synchronization in systems of coupled oscillators. Since over the years a wide literature has been written about this topic, here we focus only on general definitions and basic concepts of synchronization, starting from some historical notes and simple study cases. Particularly, a paragraph concerns the Kuramoto model, which provide us a very effective approach to measure synchronization level in a oscillatory system.

A deepening about this model and in particular its mean field formulation in the thermodynamic limit can be found in Appendix C, while Appendix B is a brief note about the master stability function approach for analyzing the stability of synchronization states. Appendix A is a general introduction to graph theory and complex networks: here we give some basic definitions and properties of networks, which we sometimes need in this thesis.

In Chapter 2 we describe neural networks and, in particular, neurons and synapses, from the biological point of view. We give also a view of the most important experimental techniques, which have been used to detect synchronous phases, and some experimental evidences of synchronization in real neural tissue. Then, we list some relevant results concerning the emergence of synchronization phenomena in computational neuroscience.

Chapter 3 is devoted to the detailed description of our model of neural network: we introduce the integrate-and-fire equation for the membrane potential of the single neuron and a phenomenological model for the short term synaptic plasticity, the event-driven map algorithm, that we use to simulate the network dynamics, and the heterogeneous mean field formulation of the model.

Finally, in Chapters 4 and 5 we discuss our results about the role of heterogeneity in purely excitatory networks (Chapter 4) and the interplay between heterogeneity and inhibition in excitatory and inhibitory networks (Chapter 5) in driving the synchronization and functional properties of the system. An extension of this last Chapter can be found in Appendix D, where we compare the mean field formulation of the model with the dynamics of the finite connectivity network.

Chapter 1

Synchronization in coupled self-oscillatory systems

In this work synchronization is the main dynamical phenomenon we investigate on our networks. Thus, in this first Chapter we present a general introduction of this non-linear phenomenon, focused on what we will need to understand next chapters and, particularly, our results. Starting from some historical remarks, known examples and basic concepts about synchronization, we describe how a simple system consisting of a single oscillator with an external periodic forcing or of two coupled oscillators can become synchronous. Then, we consider more complex cases of systems with many oscillators and especially the Kuramoto model for synchronous-asynchronous phase transitions, whose order parameter will be largely used in our results (Chapters 4 and 5).

1.1 What is synchronization?

In the scientific community, synchronization is probably one of the oldest known and studied non-linear phenomena and one of the most interesting effects of oscillating phenomena [14]. From the first observations of synchronous systems and, in particular, from the 20^{th} century, this complex dynamical process has been largely investigated, but nevertheless many problems still remain open [15].

"Synchronization" comes from two Greek words: $\sigma\upsilon\nu$ (*syn*), which means "the same, common", and $\chi\rho o\nu o\zeta$ (*chronos*), which means "time". Therefore the adjective "synchronous" can be translated with the expression "same or common time". Extending this definition, Pikovsky and co-workers [2] define synchronization as an adjustment of rhythms of oscillating objects due to their weak interaction or as an adjustment of the time scales of oscillations due to interaction between the oscillating processes [14]. A further definition is given by Barrat et al. [11], who state that in systems of coupled oscillators synchronization appears as the emergence of a coherent behavior, when the elements of the system follow the same dynamical pattern.

Nowadays it is well known that synchronization phenomena can appear in three different types of systems: in coupled self-oscillatory systems, in chaotic systems and in excitable systems with noise [14]. Considering all these systems, many different synchronization states have been observed [2, 11, 16]:

- Complete or identical or full synchronization is a perfect locking of the trajectories of two systems.
- Generalized synchronization appears when the output of a system is associated to a given function of the output of the other system.
- Phase synchronization is a locking of the phases with a weak correlation in the amplitudes. The case in which the two systems lock their phases and amplitudes, but with the presence of a time lag, is called lag synchronization.

- Intermittent lag or imperfect phase synchronization implies that the two systems show most of the time a lag or phase synchronization, with intermittent bursts of local asynchronous behavior or temporary phase displacements.
- Finally, an almost synchronization appears when the difference between a subset of the variables of one system and the corresponding subset of variables of the other system asymptotically tends to zero.

In particular, for systems of coupled oscillators, which we consider in this work, we can globally distinguish between external synchronization and mutual synchronization [15]. The first one occurs when the initial oscillatory system is driven by an external periodic force and its frequency hooks the driving signal. Otherwise, mutual synchronization concerns two or many coupled oscillatory units, when they begin to oscillate with the same frequency, which is not simply a linear sum of all the frequencies: indeed, if one oscillator accelerates or decelerates compared to the common frequency, the others force it to slow down or to hurry up.

1.2 Historical notes and known examples

Synchronization of oscillations was observed for the first time in 1665 by the Dutch physicist Christian Huygens, who saw that two pendulum clocks hanging from the same beam periodically rearranged their rhythms to oscillate in anti-phase [17]. He correctly guessed that this "sympathy of two clocks", as he called it, had been produced by an imperceptible motion of the common frame or, translating it into a modern terminology, by the coupling between these single units.

Some years later, the German physician Engelbert Kaempfer observed synchronization in a swarm of fireflies, which periodically lit up and turned off synchronously [18].

In a different biological system, in 1729 the French astronomer and mathematician Jean-Jacques Dortous de Mairan noticed that the leaves of a beam plant, put both in a natural environment and in a dark room, daily oscillated in accordance with the change of day into night [2]. Starting from those observations, nowadays it is known that all biological systems are regulated by internal biological clocks that follow the change between day and night and that are called circadian rhythms (from two Latin words: *circa* = about and *dies* = day).

About two centuries later, in 1920, Eccles and Vincent discovered the synchronization property of two coupled triode generators (electrical devices that produce an alternating current) [19] and from these results Appleton and Van der Pol started to systematically study synchronization, laying the first steps for a better understanding [20, 21].

Finally, in the 40s, Lord Rayleigh described a phenomenon of synchronization in two different organ-pipes, which close to each other sounded in unison [22], and later in optics synchronization of lasers was discovered [23] and it was used to obtain a power stronger than that obtained by a single laser.

From these and other similar observations, it gradually became clear that different synchronous phenomena could appear in systems which seem to have nothing in common and, therefore, a unified theory to describe them was necessary. Nowadays, it is well known that both simplest systems of few units and ensembles with thousands of elements, belonging to different science fields, from physics to economics, form engineering to life sciences, from chemistry to social life, can synchronize. Indeed, synchronization events have been observed in pacemaker heart cells, in insulin-secreting cells of the pancreas and in cells of the mammalian small intestine, in swarms of crickets that chirp in unison, in ecological systems, in arrays of microwave oscillators and in arrays of super-conducting Josephson junctions [2, 14, 15, 24, 25].

Finally, regarding this work, also neural ensembles in the brain can display rhythmic activity due to synchronized firing of neurons, as we will explain in the next Chapter. The first who

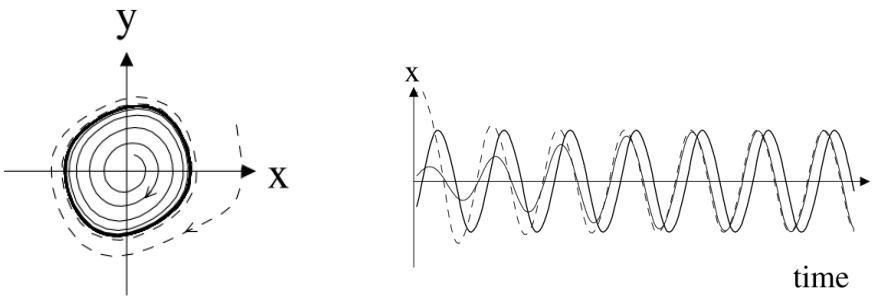

(a) (b)

FIGURE 1.1: (a) The closed bold curve in the phase plane is an example of a limit cycle. For a self-sustained oscillator, the limit cycle is a simple attractor: if a perturbation forces the system to move out of this limit cycle, the system will be attracted back towards that curve, following a given trajectory, as for example the thin solid curve or the dashed one. Image from [2]. (b) Time plot of these trajectories. Image from [2].

became interested in the spontaneous emergence of synchronous dynamics in neural systems was Norbert Wiener in the 60s, during his research on the brain waves (see Section 2.2). According to him, those waves could be produced by a coherent behavior of neurons [26]. Some years later, Arthur Winfree tried for the first time to mathematically approach synchronization problems and with his simulations he showed that in a large population of coupled oscillators with distributed natural frequencies a phenomenon similar to a thermodynamic phase transition from asynchronous to synchronous regimes could occur for sufficiently strong couplings [27].

1.3 Preliminary concepts

First of all, to describe synchronization we need to consider an ensemble of oscillators. An oscillator is a dynamical system in which one of its variables, let's say $x(t)$, is a periodic function of time, as for example the angular position $\theta(t)$ for a pendulum clock. Many objects in nature can display such a behavior, from planets to cell membranes in human tissues. A simple one dimensional oscillator is described by the following first-order differential equation [2, 24]:

$$\dot{x}(t) = f(x), \tag{1.1}$$

where $\dot{x}(t) = \frac{dx(t)}{dt}$ and $f(x)$ is a generic function of time, such that $x(t)$ is stable periodic solution, that is $x(t+T) = x(t)\ \forall t$. The time interval T is called period: it is the time interval needed to make a complete oscillation cycle, whose waveform can assume any kind of shape, and its inverse is the oscillation frequency f (number of oscillation cycles per time unit). We also define the angular frequency $\omega = 2\pi f = 2\pi/T$. As this angular frequency can change because of an external action on the oscillator or its coupling with other units, we will call natural frequency the frequency of the isolated oscillator.

Considering a single oscillator, its two variables or coordinates $x(t)$ and $y(t)$ (angular position of a pendulum and its velocity for example) lie on a space, called phase space, and any $y(t)$ vs. $x(t)$ plot is called phase portrait of the system. Because of the periodic dynamics of the system, this phase portrait always corresponds to a closed curve, called limit cycle [24] (Fig. 1.1(a)). The simplest form for a limit cycle is a circle, which is obtained when the coordinate $x(t)$ is sine function, as for example

$$x(t) = A\sin(\omega_0 t + \phi_0), \tag{1.2}$$

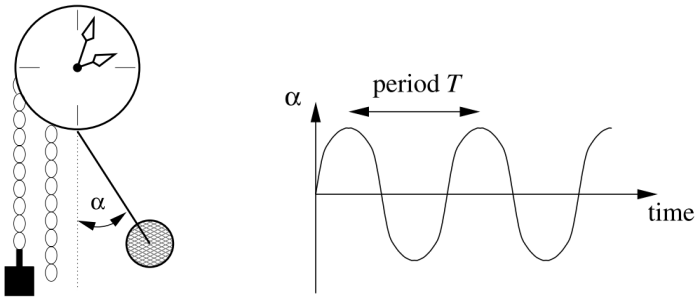

FIGURE 1.2: (a) The pendulum clock is an example of a self-sustained oscillator. The internal source of energy is represented by the potential energy of the lifted weight, which is transformed into the oscillatory motion of the pendulum. Image from [2]. (b) The angular position of a pendulum (its angle α with respect to the vertical) is a periodic function in time with period T; the maximum value of α is the oscillation amplitude. Image from [2].

where ω_0 is the angular frequency, ϕ_0 is the initial phase shift and A is its amplitude.

Now, if for example we considered the angular position of an isolated pendulum clock and its angular velocity, we cannot state that these two quantities, referred to the motion of the single oscillator, are synchronous. Rather we need to have at least two oscillatory systems with their own natural frequency. Then, connections among these single units should be added to set up a weak coupling regime, that is a regime where the coupling term is weak enough to let the oscillators influence each other and not to deprive the single components of their individuality.

In particular, about synchronization, we are interested in a subset of nonlinear systems with a periodic dynamics called self-sustained oscillators or self-oscillatory systems, which were initially introduced by Andronov, Vitt and Khaikin in 1937 [28]. A self-sustained oscillator is characterized by the following features [2]:

1. It is a nonlinear system with an internal source of energy or power that is transformed into oscillatory movement, so that it oscillates by itself and not because of repetitive kicks from outside, and an energy dissipation term during motion.

2. The oscillation shape is determined by the parameters of the system and not by the initial conditions.

3. The oscillation is stable to at least small perturbations.

In a coupled system, if even just one among the oscillators was missing one of these features, we could observe something similar to synchronization, but it would be only a resonance or adjustments of rhythms.

One of the most famous self-sustained oscillator is described by the van der Pol equation, a second-order differential equation which corresponds to a nonlinear damped oscillator [24]. Examples of self-oscillators are the classical pendulum clock (Fig. 1.2(a)), fireflies with their rhythmic flashes, circadian rhythms which exist also in absence of 24-hour external cycles of day and night [14]. On the contrary, tidal waves movements do not represent a self-oscillating system, as they are caused by the daily variation of gravitational lunar field, without which they would disappear [2].

In addition to this description of self-sustained oscillators, we need to define the concept of coherence and phase locking. Coherence occurs when two signals show a fixed phase relationship with each other or with another reference signal. If in particular these signals are produced by two mutual coupled oscillators i and j with respective frequencies f_i and f_j and

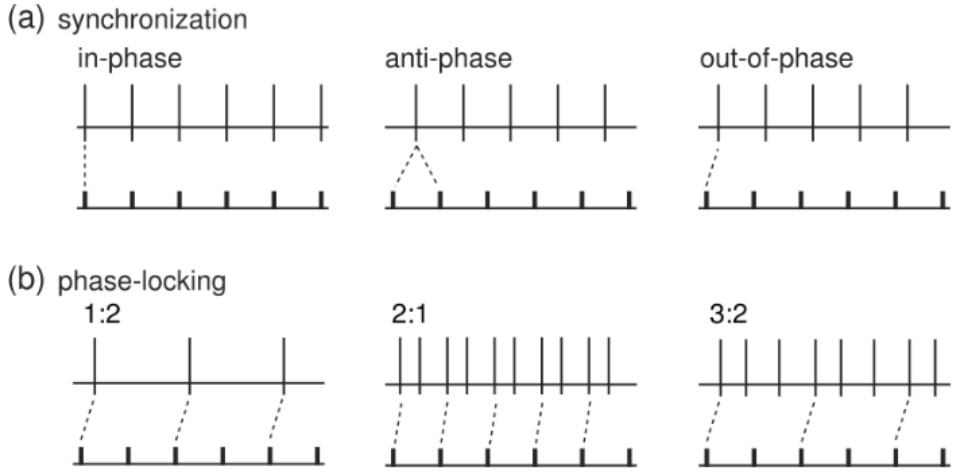

FIGURE 1.3: Schematic representation of synchronization and $m : n$ phase-locking between two oscillators, which are characterized by periodic pulsed signals. Image adapted from [29].

they maintain a fixed phase difference, independently by their amplitudes, they are said to be phase locked or to display phase locking or entrainment [1]. More precisely, a strict phase locking implies a constant phase shift:

$$|m\phi_i(t) - n\phi_j(t)| = const, \tag{1.3}$$

where $\phi_i(t)$ and $\phi_j(t)$ are the phases of the two oscillators and m and n are integers. In particular, if $const = 0$ and $m = n = 1$, we get an in-phase locking; if $const = \pi$ and $m = n = 1$, an anti-phase locking. If $m \neq n \neq 1$, it is said that the oscillators are $m : n$ phase locked. A non-strict phase locking implies only a bounded phase shift:

$$|m\phi_i(t) - n\phi_j(t)| < const. \tag{1.4}$$

In a larger system, these two oscillators i and j are considered synchronous if both a frequency entrainment (weak condition), that is $Mf_i = Nf_j$ (where M and N are integers), and a phase locking (strong condition) are fulfilled [15]. The difference between phase-locking and synchronization is represented in Fig. 1.3.

Strictly speaking, in this work we will consider synchronization as a $1 : 1$ phase locking. If all the oscillators in a system satisfy these conditions, then we will have a total synchronization; otherwise, if only a subset of the elements is synchronous, we will call it cluster or partial synchronization.

1.4 Two simple case studies

To treat synchronization phenomena in a more quantitative way, let's start considering a single self-sustained oscillator driven by a periodic external force. As a small perturbation influences only its phase and not its amplitude, we can more conveniently describe its motion using its phase as a coordinate. This phase $\phi(t)$ will oscillate according to the oscillator natural angular frequency ω_0, constant in time, as reported in the following equation [15]

$$\dot{\phi}(t) = \omega_0. \tag{1.5}$$

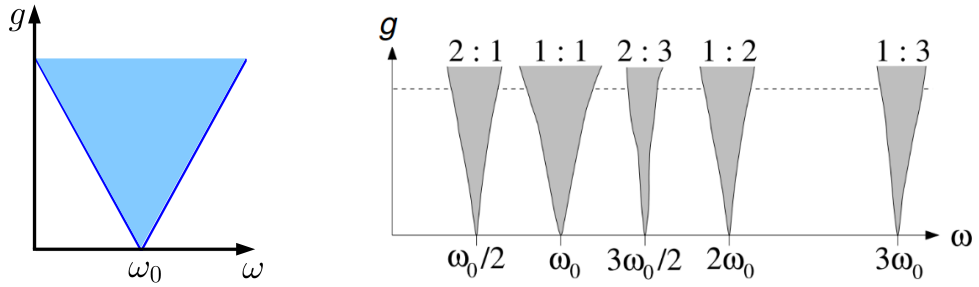

FIGURE 1.4: (a) A typical Arnold tongue plot, with the frequency ω as a function of the coupling g; ω_0 is the oscillator natural frequency. The colored (non-colored) region corresponds to the $1:1$ synchronous (asynchronous) regime; the blue lines represent the conditions expressed in Eq. (1.9). (b) Examples of generalizations of Arnold tongues for $m:n$ synchronization. The numbers on the top of each tongue show the order of locking. Image from [2].

If now we apply a small perturbation with a periodic external force of frequency ω, the previous equation will become:

$$\dot{\phi}(t) = \omega_0 + gq(\phi - \omega t), \tag{1.6}$$

where g is the amplitude of the external force ($g \ll 1$, as the perturbation has to be small) and q is a generic 2π-periodic function of phases ϕ and ωt, which for simplicity can be a sine function. Defining the difference between the phase of the initial oscillator and the phase of the external force as $\theta = \phi - \omega t$ and its derivative with respect to time $\dot{\theta} = \dot{\phi} - \omega$ and replacing them in Eq. (1.6), we obtain:

$$\dot{\theta} = -\Delta + g \sin\theta, \tag{1.7}$$

where $\Delta = \omega - \omega_0$. In order to achieve a synchrony or a phase locking between the oscillator and the external force, we want $\theta(t)$ to be constant in time, that is $\dot{\theta} = 0$. This is equivalent to looking for the stable steady-state solution $\bar{\theta}$ of Eq. (1.7):

$$\bar{\theta} = \arcsin\left(\frac{\Delta}{g}\right), \tag{1.8}$$

which exists only if

$$\left|\frac{\Delta}{g}\right| < 1 \;\rightarrow\; \omega_0 - g < \omega < \omega_0 + g. \tag{1.9}$$

This means that a synchronous solution of this system exists when the coupling term is large enough and in particular only if the forcing term oscillates in a quite similar way to what the initial oscillator does on its own. This condition defines in the g vs. ω plane a synchronization area, called Arnold tongue, whose typical representations for the $1:1$ synchronization and the more general $m:n$ synchronization are reported in Fig. 1.4.

We can now repeat this analysis in a more general system of two weakly coupled oscillators, whose dynamical equations are [2]

$$\begin{aligned} \dot{\phi}_1(t) &= \omega_1 \\ \dot{\phi}_2(t) &= \omega_2, \end{aligned} \tag{1.10}$$

where $\phi_1(t)$ and $\phi_2(t)$ are their respective phases and ω_1 and ω_2 their respective natural frequencies. Adding a weak coupling between these units means considering in both the previous equations a further term represented by a generic 2π-periodic function of the two phases and

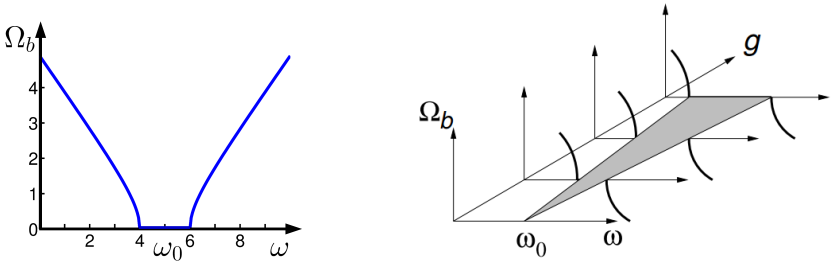

(a) (b)

FIGURE 1.5: (a) Beating frequency Ω_b as a function of ω, for the coupling function $q(\theta) = \sin\theta$ and for a fixed value of the coupling strength $g = 0.5$ and of the oscillator natural frequency $\omega_0 = 5$. The central region where Ω_b is zero is the synchronous area. (b) The family of Ω_b vs. ω plots for different values of the coupling g produces the grey area which corresponds to the synchronization region or Arnold tongue. Image adapted from [2].

proportional to the coupling constant $g \ll 1$:

$$\begin{aligned} \dot{\phi}_1(t) &= \omega_1 + g q_1(\phi_2 - \phi_1) \\ \dot{\phi}_2(t) &= \omega_2 + g q_2(\phi_1 - \phi_2), \end{aligned} \tag{1.11}$$

As above, without loss of generality, we can define the difference between the two phases $\theta = \phi_2 - \phi_1$ and its time derivative $\dot{\theta} = \dot{\phi}_2 - \dot{\phi}_1$. Then, subtracting the first equation from the second, we obtain:

$$\dot{\theta} = \Delta + g q(\theta), \tag{1.12}$$

where $\Delta = \omega_2 - \omega_1$ and $q(\theta) = q_2(-\theta) - q_1(\theta)$, which in the simplest case of sine functions ($q_1(\theta) = q_2(\theta) = \sin\theta$) becomes $q(\theta) = -2\sin\theta$. Now, to obtain a phase locking, i.e. a regime where the difference between the two phases is fixed in time ($\dot{\theta} = 0$), we find the stable steady-state solution

$$\bar{\theta} = \arcsin\left(\frac{\Delta}{2g}\right), \tag{1.13}$$

which imposes a condition similar to Eq. (1.9): synchronization appears when the frequency mismatch $|\Delta|$ is less than some critical coupling value $2g$. This produces an analogous synchronization region (Arnold tongue) to Fig. 1.4(a). Out of this synchronization area, we can observe a transition from the synchronous regime to a so-called beating regime, characterized by the disappearance of the steady state solutions and by a beating frequency Ω_b [15]

$$\Omega_b = 2\pi \left(\int_0^{2\pi} \frac{d\theta}{2gq(\theta) - \Delta} \right)^{-1}, \tag{1.14}$$

which in our simple sinusoidal case can be written as:

$$\Omega_b = \sqrt{\Delta^2 - 4g^2}. \tag{1.15}$$

This last expression of the beating frequency Ω_b is represented in Fig. 1.5(a), where the central horizontal plateau corresponds to the synchronous area of the Arnold tongue at fixed value for the coupling g, as reported in Fig. 1.5(b). In particular, in Fig. 1.5(a) a null value for Ω_b means that we are in the synchrony region, while non-null values mean that we are escaping the synchrony region.

1.5 Systems of N coupled oscillators

We can now extend the previous analysis to a larger system of N coupled oscillators.

When we have to manage more than 2 oscillators, we need to define how to connect them. If for each oscillator we add a coupling term towards all the other units, then we will build an all-to-all system, but many other more or less simple patterns are possible if each oscillator in the system is connected only to a subset of the other elements. In general, in a system of N single units the underlying links scheme, which sets to whom each element is connected, forms an interaction network. A short introduction to graph and network theory with some basic concepts, useful for this work, can be found in Appendix A. Here, let's only define the $N \times N$ Laplacian matrix of the connections: the generic element L_{ij} (with $i \neq j$) of this matrix is null if no link exists between the $i-$th and $j-$th unit, while it is equal to -1 if i and j are connected by a link; moreover, L_{ii} represents the total number of connections owned by unit i and consequently $\sum_{j=1}^{N} L_{ij} = 0$.

Then, as in Eqs. (1.11), the general evolution equations for a system of N identical coupled oscillators can be written as [11]

$$\dot{\phi}_i(t) = F(\phi_i) + g \sum_{j=1}^{N} L_{ij} q(\phi_j), \quad i = 1, ..., N, \tag{1.16}$$

where F and q are generic functions of the phase, equal for all the oscillators, and the sum is over all the j units of the network. Here, we have considered a linear coupling proportional to the constant g: each unit i is coupled to a linear superposition of function $q(\phi_j)$ of the j oscillators linked with i.

A global synchronization of this system would lead all the oscillators to evolve according to a common periodic function $s(t)$, so that $\phi_i(t) = s(t)\ \forall i$, with $\dot{s}(t) = F(s)$, is a solution of the previous equations, whose stability can be studied using the *master stability function (MSF)* approach (see Appendix B). What clearly emerges from this formulation and in particular from the resulting stability condition is a fundamental relation between the spectral properties of the system connectivity, given by the eigenvalues ratio of the Laplacian matrix, and the properties of the oscillators, represented by their coupling. This means that if we consider a particular class of oscillators with given properties and we only change the connectivity patterns among them, we could directly influence the emergence of synchronization, as if the nature of the oscillators in a system was not as significant as network topology.

1.6 The Kuramoto model

The analytical approach to synchronization proposed in 1984 by Yoshiki Kuramoto represents a significant step in the understanding of synchronization in large ensembles [30], as it lets us treat the spontaneous emergence of collective behavior in those systems and describe the transition a system can perform from a synchronous state to an asynchronous one as a function of the coupling strength among its self-oscillating units. A very wide bibliography can be found about this model, starting from the original work by Kuramoto [31], to later publications, as for examples [2, 11, 15, 30, 32–36], from which we were mainly inspired in writing this section.

Starting from Winfree's approach (Section 1.2) on phase transitions for large populations of interacting oscillatory units, Kuramoto began to work out his famous model in the 80s [35, 36].

As in the previous section, we start considering the general case of a system of N coupled oscillators, each one characterized by an angular phase ϕ_i and a natural frequency ω_i ($i = 1, ..., N$). In order to analytically treat such a system, as Winfree and Kuramoto guessed, we need to use a mean field approach: for this reason we assume an all-to-all interactions network

with a purely sinusoidal coupling. Then, the system dynamics is represented by the following set of non-linearly coupled equations:

$$\dot{\phi}_i = \omega_i + \frac{g}{N}\sum_{j=1}^{N}\sin(\phi_j - \phi_i), \tag{1.17}$$

where the natural frequencies are distributed according to a given probability density function $P(\omega)$, which for simplicity is assumed to be unimodal and symmetric about its mean frequency Ω, like for example a Gaussian distribution (See Appendix C for more details). Taking advantage of the rotational symmetry of the model, this mean frequency can be easily set to $\Omega = 0$, redefining $\phi_i \to \phi_i + \Omega t$ for all i, as if we went into a rotating frame at frequency Ω. The coupling constant $g \geq 0$ is divided by the number N of oscillators, so that the model remains well-defined in the thermodynamic limit ($N \to \infty$).

As we want to describe a synchronization transition, we need to define the following order parameter, called Kuramoto parameter:

$$R(t)e^{i\psi(t)} = \frac{1}{N}\sum_{j=1}^{N} e^{i\phi_j(t)}. \tag{1.18}$$

This macroscopic quantity can be interpreted as the collective rhythm produced by the whole population. If we represent in the complex plane the phase of i-th oscillator as a point on a circumference of unit radius, then an ensemble of N oscillators will correspond to a set of points variably distributed on this circumference (violet points in Fig. 1.6) and the left term in Eq. (1.18) will represent the complex average value of the position of those points. This midpoint (yellow point in Fig. 1.6) is characterized by a phase ψ and a distance R from the center (module of the complex number), that measures the degree of coherence in the collective behavior of the oscillators. Indeed, if they evolve in a incoherent way (Fig. 1.6(b)), their phases will be uniformly distributed on the circumference at any time and their average will be close to the center: this is the asynchronous state of the system and it corresponds to very small values for the module R of the Kuramoto parameter, or to $R \to 0$. On the other hand, if a subset of oscillators begins to show a phase locking (Fig. 1.6(c)), they will be concentrated in a small arc of the circumference and their average will be far from the center: this is the synchronous state and the resulting R tends to be equal to the circumference radius, or $R \to 1$. The more synchronous the oscillators are, the more R increases, until it becomes equal to 1 in the full synchronized state (Fig. 1.6(d)).

Thanks to the definition of the Kuramoto parameter in Eq. (1.18), using the mean field quantities

$$\begin{cases} R(t)\cos\psi(t) = \frac{1}{N}\sum_{j=1}^{N}\cos\phi_j(t) \\ R(t)\sin\psi(t) = \frac{1}{N}\sum_{j=1}^{N}\sin\phi_j(t), \end{cases} \tag{1.19}$$

we can rewrite Eq. (1.17) as

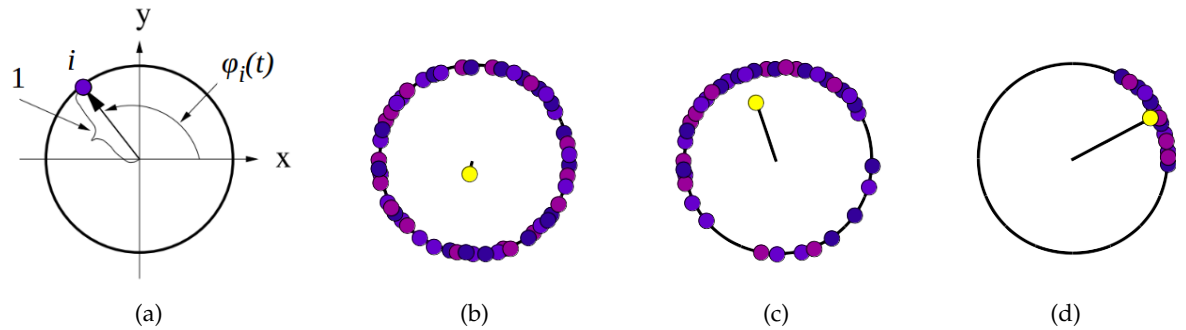

FIGURE 1.6: (a) Representation of the phase $\phi_i(t)$ of oscillator i in the complex plane. At each time and for each oscillator, $\phi_i(t)$ belongs to this unitary radius circumference. Image adapted from [2]. (b) Asynchronous regime: oscillators phases are uniformly distributed on the circumference and $R(t) \to 0$. (c) Partially synchronous regime: some phases are locked at a given value and $0 < R(t) < 1$. (d) Fully synchronous regime: all phases are concentrated in a small arc of the circumference and $R(t) \to 1$.

$$\dot{\phi}_i = \omega_i + \frac{g}{N}\sum_{j=1}^{N}(\sin\phi_j\cos\phi_i - \cos\phi_j\sin\phi_i) \tag{1.20}$$

$$= \omega_i + g\left(\cos\phi_i\frac{\sum_{j=1}^{N}\sin\phi_j}{N} - \sin\phi_i\frac{\sum_{j=1}^{N}\cos\phi_j}{N}\right) \tag{1.21}$$

$$= \omega_i + gR\left(\cos\phi_i\sin\psi - \sin\phi_i\cos\psi\right) \tag{1.22}$$

$$= \omega_i + gR\sin(\psi - \phi_i), \tag{1.23}$$

where now each oscillator seems to be isolated from the other units: it evolves according to its natural frequency ω_i and it is coupled to the rest of network through a mean field term proportional to the effective coupling Rg.

During the evolution of the system, it can happen due to instabilities that a nonzero mean field term drives two oscillators to synchronize. Consequently, as in a nucleation process of a phase transition, this small coherent subset generates a finite contribution to the mean field and, since the coupling depends on the parameter R, a positive feedback mechanisms between this coupling and the coherence level begins to establish. In this way a partial synchronization regime emerges with a synchronous or locked group and an asynchronous or unlocked one. The first group consists of those oscillators, whose natural frequency ω is near to the mean frequency Ω: they lock together at that frequency and with the average phase $\psi(t)$. All the other oscillators, which belong to the tails of $P(\omega)$, do not get locked and they keep their own rhythm. If otherwise the system properties cannot support a positive feedback, as for example occurs when the initial coupling g is too weak, the oscillators continue to behave as uncoupled elements, as the mean field term is not be able to influence quite significantly their dynamics, and the coherent group gradually disappears.

With the enhancement (reduction) of the coherent population in the system, the effective coupling gR continues to grow (decrease) and this attracts (rejects) other oscillators to the synchronized group, until $R(t)$ reaches its asymptotic value (Fig. 1.7(a)), that is $R(t) \xrightarrow[t\to\infty]{} R_\infty$, with $\mathcal{O}(N^{-1/2})$ fluctuations.

Various numerical simulations have proved that R_∞ depends only on the constant g and not on the initial conditions: indeed, given a coupling g, the system with fixed $P(\omega)$ evolves

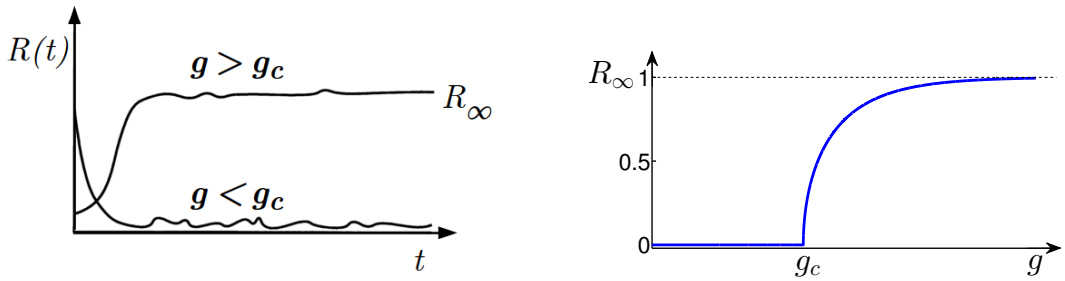

(a) (b)

FIGURE 1.7: (a) Example of typical time evolutions of $R(t)$, which can result from numerical simulations of the Kuramoto model. Image adapted from [36]. (b) A typical Kuramoto phase transition from an asynchronous regime with $R_\infty = 0$ to a synchronous one with $R_\infty \to 1$, as a function of the coupling g among the oscillators. The analytical expression of this function is shown in Appendix C.

towards a globally attracting state, which can be either totally synchronous if $g > g_c$ or asynchronous if $g < g_c$, as shown in Fig. 1.7(b). The first case corresponds to $R_\infty = 1$, the second one to $R_\infty = 0$. Thus, as a function of the coupling in the system, we actually obtain a first order phase transition between two different synchronization regimes, whose order parameter is $R(t)$ and critical point $g = g_c$.

A further discussion about the Kuramoto model and its extension to the thermodynamic limit can be found in Appendix C.

In the next Chapter, we describe how the fundamental elements of a neuronal system, namely neurons and synapses, work and in particular what is the role of synchronization in neuroscience and how to detect it from the computational point of view.

Chapter 2

Synchronization in neuroscience

Synchronization has been shown to be of great relevance in neural systems. Indeed, since the elementary processing unit of the central nervous system (neuron) and in particular its membrane potential has an oscillatory behavior, a neuron can be thought as a phase oscillator and specifically as a self-sustained oscillator and therefore it is natural to expect the onset of synchronization phenomena in networks of coupled neurons and in any living nervous systems.

Since the dynamical systems investigated in our work are neural networks, in this Chapter we first describe them from a biological point of view, looking at their main constituent elements and at the most known experimental techniques, which have been used to observe them and to analyze their dynamical behaviors. We then report some results about *in vivo* and *in vitro* experiments on different neural tissues, in which synchronization seems to play a fundamental role, allowing those systems to perform specific cognitive and sensory functions. Finally, we provide a brief review of some relevant results concerning synchronization phenomena in numerical simulations of neural networks.

2.1 Elements of neural systems physiology

Neurons are the fundamental discrete elements of any nervous systems and the main dynamical units for processing information, since they continuously receive, elaborate, generate and transmit specific electrical signals, which are the basis of any cognitive, sensory, metabolic and motor function of a living system.

According to one of the most recent estimate, the number of neurons in a human brain is about 86 billion. Together with them, there is about the same number of non-neuronal cells, called glial cells or glia, which seem to play an important regulatory role, as energy supply and structural stabilization of brain tissue, without being directly involved in information processing [37–39]. In particular, in the cerebral cortex or neocortex, which is the largest region of the mammalian brain and in particular it is its thick external layer (made of a neural tissue called gray matter), with a high density of neurons, synapses and glial cells, the density of neurons is about 10^4 neurons/mm^3 [3]. Each cortical neuron can typically manage thousands of synapses and its cell body ranges in diameter from about 10 to 50 μm [40].

There exist different types of neural cells (see for instance in Fig. 2.1), which can be classified according to their shape or to the functions they perform, but all of them are typically characterized by three main elements, called soma, axon and dendrites [29, 41]. The soma is the cell body and it is the central processing unit of the cell: electrical input signals, coming from the other close neurons and collected by the receptive prolongations of the nerve cell, called dendrites, are transmitted to the soma, which elaborates and integrates them. If the total input exceeds a certain threshold, then an output signal, called action potential, is generated. This response is sent to the other cells through a different type of nerve filament, called axon. An axon is typically larger than a dendritic branch, since its diameter is of the order of magnitude of micrometer. It has an average of 180 synapses/mm, while in the dendritic tree we find, on

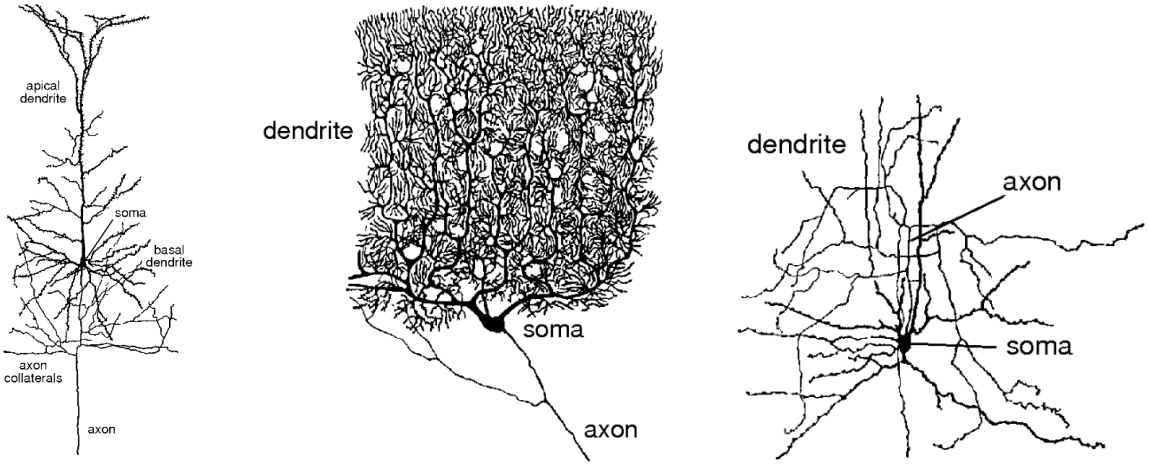

(a) (b) (c)

FIGURE 2.1: (a) A cortical pyramidal neuron, which is a typical excitatory neuron of the cerebral cortex. Image adapted from [40]. (b) A Purkinje neuron of the cerebellum. Image adapted from [40]. (c) A stellate neuron, a typical inhibitory neuron of the cerebral cortex. Image adapted from [40].

average, 2 synapses/μm, and it can both send signals to close neurons and cross macroscopic regions of the brain several centimeters far [40].

The junction point which allows the information transmission between two neurons and in particular between the axon of a transmitting neuron and a dendritic branch of a receiving cell is called synapse. From here on, we will refer to the first neuron as the presynaptic neuron and to the second one as the postsynaptic neuron [41].

The main variable necessary to describe the dynamics of a neuron is its membrane potential. The membrane potential is defined as the electric potential difference between the interior fluid of the cell and the extracellular surroundings, caused by concentration gradients of the sodium Na^+, potassium K^+, calcium Ca^{2+} and chloride Cl^- ions and maintained by the lipidic impermeable cell membrane [29]. Crossing neurons membrane, these ions can flow into or out the cell through membrane-spanning ion channels, called ion pumps, creating electric currents which alter the membrane potential from its rest negative value to even positive values (depolarization phase). At rest, the membrane potential of a neuron is about -70 mV for most neurons [3, 41, 43]. If due to these ionic currents it reaches a given threshold value, an action potential is actually generated. An action potential, also called (electrical) spike or nervous pulse, is a very short and fast electrical signal, represented by a fluctuation or a wave of depolarization in the membrane potential. It is the most elementary unit of neural information that can be transmitted, with an amplitude of about 100 mV and a duration of 1-2 ms. In details, an action potential consists of an initial phase of depolarization, during which the membrane potential increases up to a value of about +30 mV, followed by a repolarization, or a phase of decrease, which brings it to a lower value than the original one, let's say -80 mV. Therefore, immediately after the emission of a spike, a neuron falls in a resting state, called refractory period, lasting few seconds [40], during which the membrane potential recovers its initial level, passing from -80 mV to -70 mV. In this last phase, called hyperpolarization, no other action potential can be produced and sent [3].

The typical shape of an action potential is reported in Fig. 2.2(a) and Fig. 2.2(b). This signal propagates along the neuron axon with an average velocity from 2 to about 120 m/s. Its shape typically does not change and its amplitude does not undergo any attenuation during its propagation, since each axonal segment is electrically isolated from the outside by a lipidic

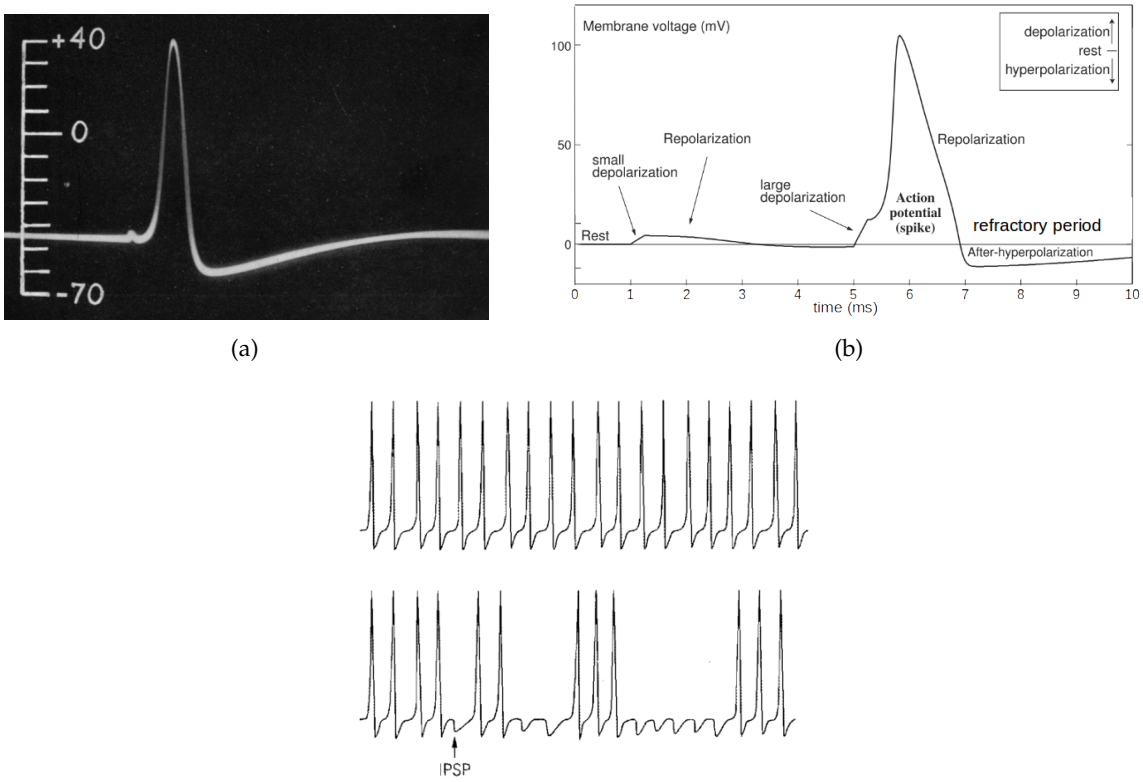

(a) (b)

(c)

FIGURE 2.2: (a) One of the first measures of an action potential and, in particular, this is the action potential recorded between the inside and the outside of the neuron of a squid. The vertical scale indicates the potential in millivolts of the electrode positioned inside the axon, while the outside environment has been set at zero potential. Image adapted from [42]. (b) Outline of a typical action potential. On the left, there is a weak depolarization which is not sufficient to reach the firing threshold and to produce a spike, followed by a large depolarization and a spike. For simplicity, the vertical scale of the potential (in mV) has been shifted upwards so that the rest value of the membrane potential is zero and its peak value is 100 mV. Image adapted from [29]. (c) Above: an example of a typical excitatory spike train of an active neuron. Below: if this neuron receives inhibitory signals (IPSP), then some of its action potentials will be suppressed and the timing and the regularity of its spike train will be altered. Image adapted from [3].

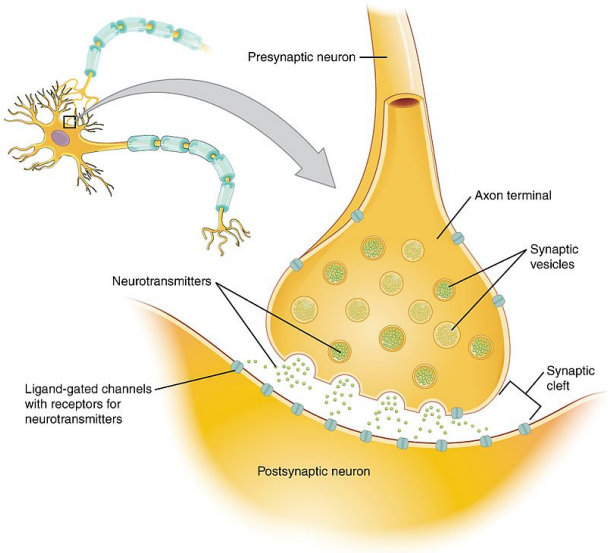

FIGURE 2.3: Representation of a chemical synapse. Image from [44]

covering [43]. Considering that all action potentials share a similar shape, it is evident that this shape cannot carry information. Information is rather encoded in the number, the timing and the regularity of series of consecutive spikes emitted by a single neuron, called spike trains [41].

If a cell emits an action potential, then we will say that it "spikes" or "fires" a pulse, while a spiking or a firing cell is cell that it is generating and sending its action potential. Moreover, we will call the number of action potentials emitted per unit time (usually a second), the frequency of firing or the firing rate of the neuron. A typical average firing rate for nerve cells in the central nervous system is of the order of 10-20 per second [43].

Because of the opening and closing mechanisms of the membrane ion channels, the action potential generated by a neuron is an all-or-none spike: it is emitted only if the membrane potential depolarizes up to exceeding a threshold value, but if this threshold is not reached, no signal arises and the potential comes back to the rest state. Finding the exact value of this threshold is not trivial, as one can read in [29], and in general various types of neurons have different thresholds and respond in a completely different way to the same input or stimulus: this depends on many factors, both on the temporal characteristics of the stimulus and its location and on the intrinsic properties of neurons, such as ion channels dynamics or the morphology of their dendritic trees [3]. Also, it is important to underline that every biological element of the nerve cell, and specially its membrane, behaves as a highly non linear integrator for all the electrical signals, which the neuron continuously receives, and that a neuron never fires on its own, but always as a result of incoming spikes from other cells [29].

Once a neuron generates an action potential, this signal is immediately sent to other cells through its (presynaptic) axon, which is linked thanks to a synapse to the (postsynaptic) dendrite of another neuron. There are two types of synapses: electrical synapses, called gap junction, and chemical synapses. The main properties and differences between these two classes of synapses are reported in Table 2.1, while in Fig. 2.3 we show a chemical synapse. Since the chemical synapses are the most abundant in neural systems and since the model of synaptic coupling considered in this work (see Section 3.3) is mainly inspired by them, from here on we will treat only chemical synapses.

In such a synapse, when an action potential reaches the synaptic site, thanks to the opening mechanism of particular ion channels, specific chemical molecules, localized in the presynaptic branch and called neurotransmitters, are released through the axon membrane in a thin interspace, called synaptic cleft, between the two nervous termination. Here, they flow from the

Synapse	Distance between membranes	Synaptic cleft	Structural components	Elements for signal transmission	Synaptic delay	Transmission direction
Electrical	3.5 nm	no	junction channels	ionic currents	no	bidirectional
Chemical	20-40 nm	yes	presynaptic vesicles, postsynaptic channels with receptors	chemical neurotransmitters	0.3 - 5 ms	unidirectional

TABLE 2.1: Properties and differences between electrical and chemical synapses. Table adapted from [3].

presynaptic axon to the postsynaptic dendritic extension. When neurotransmitters are received by specific receptors on the membrane of the postsynaptic dendrite, its ion channels open and modify the postsynaptic membrane potential, generating an electrical response, called postsynaptic potential (PSP), which is sent to the postsynaptic soma [3].

From this mechanism, it clearly emerges that the action potential transmission through a chemical synapse takes place in only one possible direction and specifically from the cell which releases the neurotransmitters to the cell which holds the required receptors. A transmission in the opposite direction is forbidden.

The signal amplitude of the postsynaptic potential with respect to the presynaptic action potential defines the synapse efficacy and directly depends on the amount of neurotransmitters coming from the presynaptic cell. Intrinsic processes of the presynaptic neuron, such as variations of the membrane potential or of the frequency of spike trains, and extrinsic processes of the postsynaptic neuron, as signals reception from other synapses, can modify the synaptic efficacy. The capacity of a synapse of changing its efficacy is called synaptic plasticity and, in particular, short term plasticity (STP), if the efficacy variations last for short time intervals (few seconds), or long term plasticity (LTP), if the variations last for longer intervals (few minutes or hours). The first plasticity is produced by amount variations in the released neurotransmitters, while the second one by functional and structural alterations of neurons. Both these mechanisms seem to be related with memory and learning processes [45].

Finally, If the synaptic transmission produces an increase (depolarization) of the postsynaptic membrane potential, then we will have an excitatory postsynaptic potential (EPSP) and we will say that the postsynaptic cell is excited. On the contrary, if the postsynaptic membrane potential decreases (hyperpolarization), then we will have an inhibitory postsynaptic potential (IPSP) and the postsynaptic cell will be inhibited [43] (see Fig. 2.2(c)).

Different chemical molecules contained in the presynaptic cell can be considered as neurotransmitters, but the kind of postsynaptic potential which is produced depends only on the specific receptors or ion channels which are opened by the neurotransmitters on the postsynaptic membrane. Some presynaptic neurotransmitters are caught by receptors which can produce both an excitatory and an inhibitory response, other molecules are otherwise addressed only to a class of receptors, either excitatory or inhibitory. For instance, the glutamate neurotransmitter interacts only with receptors which will create a depolarization (excitation), while γ-aminobutyric acid or GABA and glycine interact with receptors which will create an inhibition. In this case we will directly classify these neurotransmitters as excitatory and inhibitory, respectively [3]. Moreover, each postsynaptic neuron receives, at each time, excitatory and inhibitory signals coming from thousands of synapses: before deciding whether it can generate its own action potential or not, it needs to perform a temporal and spatial integration of all these signals. This summation process depends on the localization and on the size of each synapse, on its efficacy and its interference with other close synapses and on the properties of

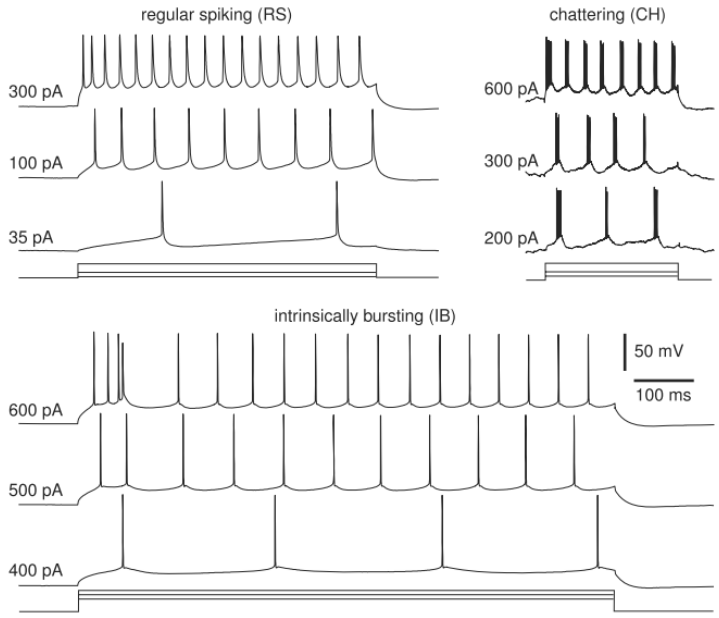

FIGURE 2.4: Some examples of firing patterns of neocortical neurons in response to different depolarizing currents (measured in pA). RS and IB are *in vitro* recordings of pyramidal neurons in the visual cortex of a rat; CH was recorded *in vivo* in cat visual cortex. Image from [29].

the postsynaptic neuron [43].

Trying to sum up this complex procedure, according to which neurotransmitters are released, looking at the physiological effects they produce on a postsynaptic cell, we can distinguish between two main types of neurons: excitatory cells and inhibitory cells. Excitatory neurons globally provoke an excitatory signal on the postsynaptic cells to which they are connected, while inhibitory neurons provoke an inhibitory signal. Thus, although from a purely biological point of view, it clearly emerges that it is the synapses itself to be excitatory or inhibitory, in this thesis we will assign this property to neurons, so that we will deal with excitatory or inhibitory neurons [46].

2.2 Experimental measures of neural activity

One of the underlying ideas which emerges in the previous Section is that the membrane potential of a neuron can be considered as the main dynamical variable one should describe to capture the global behavior of the single cell. The membrane potential of a single neuron can be measured using different intracellular and extracellular methods, as for instance recordings with electrodes during *in vitro* experiments. Signals that can be typically detected in this way are the so-called firing patterns. Examples of firing patterns are reported in Fig. 2.4. Due to the complex dynamics of membrane ion channels and their properties, each neuron can display a wide range of behaviors, each corresponding to a specific firing pattern.

In addition to this measure on single neurons, if one has to manage a large population of nerve cells, a more appropriate variable to describe this activity is the local field potential (LFP), which is a neuronal signal obtained by low-pass filtering extracellular recordings of large groups of cells and it represents the mean potential produced by the slow components of synaptic events near to a recording electrode. In this way we get an insight of the "average" behavior of a large number of interacting neurons [5, 47].

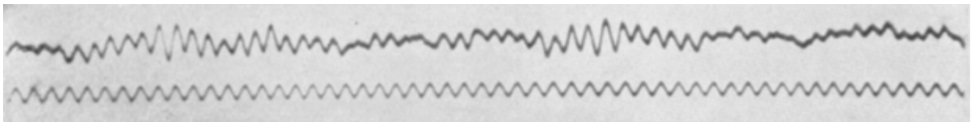

FIGURE 2.5: The first human EEG tracing, recorded in 1925 by Hans Berger with non polarizable electrodes and photographic paper. The lower line is a reference 10 Hz sine wave. Image from [49].

Looking at the largest scale of the brain activity, which is composed by multiple frequencies, one can apply both frequency domain and time domain analysis methods. At this level, many techniques can be used in experimental neurosciences. Each of these methods is always characterized by a compromise between the spatial resolution, needed for instance to investigate signals generated by neural microcircuits of the cerebral cortex, rather than the brain activity at the global scale, and the temporal resolution, considering that the propagation of action potentials among neurons occurs at the millisecond scale.

In order to have a good spatial resolution one can use the functional magnetic resonance images (fMRI) technique, which records the neural activity measuring variations on the magnetic susceptibility of neural tissues [7]. Electroencephalography (EEG), which measures electrical signals through scalp electrodes, has good temporal resolution but low spatial definition, since the EEG signal recorded by a single electrode is a spatially mean of the local field potential referring to a 10 cm^2 area. Inferring information from this signal on the specific firing patterns of the involved neurons is quite difficult.

Since its discovery, the origin and the nature of EEG signals have been intensive investigated. Historically, the first attempts of recording brain activities were carried out in 1875 by Richard Caton, a British physician who worked in Liverpool, and at the same time by some physiologists of Eastern Europe. Almost in the same period G. Fritsch and J. E. Hitzig saw that the human cerebral cortex could be electrically stimulated. Clearly, these discoveries had a huge impact on the neuroscientific world and in the following years many researchers and physiologists began to investigate at various levels the electrical nature of the nervous system and of the brain [48].

Among them, Hans Berger, an officer in the Prussian Army and an neuropsychiatrist at the University of Jena (Germany), is officially considered the discoverer of the human electroencephalogram. In a fundamental paper, published in 1929, he wrote: "*The electroencephalogram represents a continuous curve with continuous oscillations in which... one can distinguish larger first order waves with an average duration of 90 milliseconds and smaller second order waves of an average duration of 35 milliseconds. The larger deflections measure at most 150 to 200 microvolts...*" [1, 49] (see Fig. 2.5). Berger called "alpha" rhythms the large-amplitude waves, because they were the first observed signals, while "beta" rhythms the smaller in amplitude and faster waves.

Similarly to the EEG, the MEG or magnetoencephalography records the perturbations of the extracranial magnetic field produced by the electrical activity of a neuronal ensemble, without using any electrodes. The spatial resolution of a MEG signal is better than an EEG one (~ 1 cm^2), mostly because the magnetic fields do not interfere with the skull and scalp. However, such a spatial resolution is still too coarse to infer the activity of single microcircuits or cells [1]. Using Fourier analysis, the complex EEG or MEG signals can be decomposed in a combination of sine waves and a frequencies or power spectrum can be plotted to see which components are dominant, while short-time segments of EEG signals are usually studied with the so-called "wavelet" analysis or with correlation methods [1].

Finally, the diffusion tensor imaging (DTI) is a method which maps the anatomical connectivity between different brain areas using the water diffusion through the nerve fibers [7], while the positron emission tomography (PET) can be used to analyze the binding of specific chemicals, drugs and neurotransmitters [1].

At present, the best methods to get measures with the highest spatial resolution are optical methods [1, 50], as for instance imaging based on voltage-sensitive dyes (VSDI) and fast photodetecting devices, and two-photon or multiphoton laser scanning microscopy [1], which can measure the neuronal activity inside the cerebral cortex or in general in deeper brain regions.

Since Berger's discoveries, thanks to all these experimental techniques, global neural oscillations at the brain level have been observed in different mammalian species and in different frequency ranges. A clear international classification of all these brain rhythms, as they are usually called, was finally proposed in 1974. According to the order in which they were discovered, the entire observable frequency range was arbitrarily divided into bands, labeled with Greek letters, and the brain waves were distinguished as follows [51, 52] (see also Fig. 2.6(a) and Fig. 2.6(b)):

1. Slow and ultra slow oscillations, $0.02 - 0.5$ Hz
2. Delta oscillations, $0.5 - 4$ Hz
3. Theta oscillations, $4 - 8$ Hz
4. Alpha oscillations, $8 - 12$ Hz
5. Beta oscillations, $12 - 30$ Hz
6. Gamma oscillations, $30 - 80$ Hz
7. Fast oscillations, $80 - 200$ Hz
8. Ultra fast oscillations, $200 - 600$ Hz

Close frequency bands which appear in the same neuronal network are typically associated with different brain states and, on the other hand, several rhythms can temporally coexist in same or different structures. A more appropriate classification should take into account that a specific oscillation could be related to a specific physiological function or that different frequencies could involve different level of connections and computation. Unfortunately, the exact origins of most brain oscillations are still not known and it is not clear which specific cognitive functions are related to a given oscillation. What emerges is that all frequencies, from the slowest to the fastest ones, are continuously present and cover more than four orders of magnitude in the temporal scale, requiring tens of different mechanisms to be generated and a cooperation of many neural structures and circuits [51].

Globally, brain computation and decision capacities are clearly based on information transmission from one region to another [5, 53]. This transmission depends on the effective connectivity among different brain areas and the timing of global brain rhythms could limit the speed with which this communication runs: for instance, fast oscillations as gamma rhythms could favor local integration, while slow oscillations, as beta rhythms, involve many neurons belonging to more distant neuronal structures [54, 55]. In other words, the wavelength of each brain wave can be interpreted as a temporal processing window [1], during which the transmission of a message can take place, as if the brain operated in a discontinuous way with temporal packages.

2.3 Synchronization evidences in experimental neuroscience

How can brain and its basic structural elements, like neurons and synapses, perform highly complex functions, as sensorimotor or cognitive functions? This fundamental question has been investigated for many years and we are still far from a complete answer. Currently, we

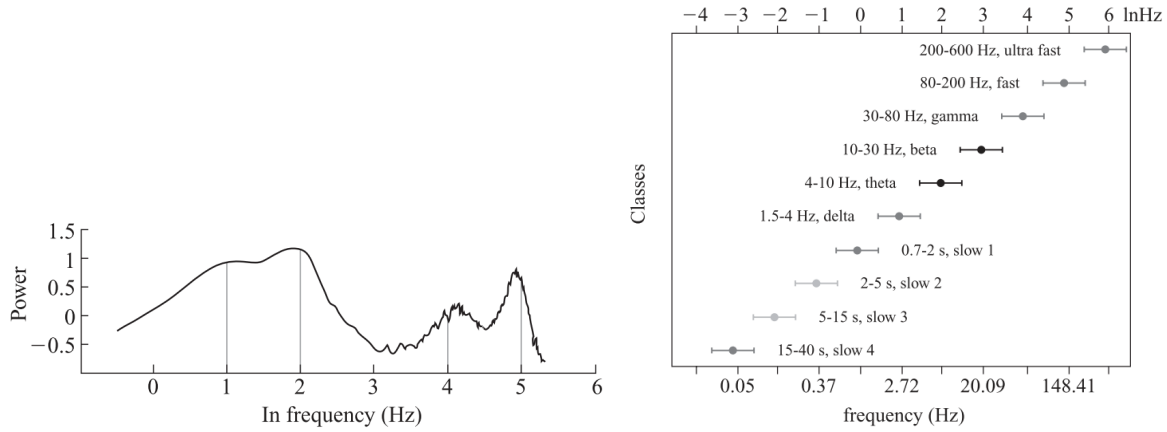

(a) (b)

FIGURE 2.6: (a) Power spectrum of the hippocampal EEG in the mouse, where the four peaks, corresponding to the traditional delta, theta, gamma and fast bands, are almost multiples of natural log integer values. Image adapted from [29]. (b) Frequency bands of cerebral cortex oscillations, showing an arithmetic progression on the logarithmic scale. For each band, the frequency ranges and their commonly used names are reported. Image from [51].

know that a neuron is not only a simple signals integrator, which collects inputs from its neighborhood, decides if the threshold is reached or not, produces and sends a spike. Rather, it is a fundamental dynamical unit with an intrinsic computational power and it continuously cooperates with many other units in extensive circuits and networks. Since the behavior of a single oscillatory and spiking object is easy to predict and carries very little information, the statistical analysis of even complex spike trains from isolated neurons does not seem to be determinant. The key point is represented by the complexity which arises when one considers large ensemble of different neurons. One of the first who proposed the idea of a spatio-temporal orchestration of neurons assemblies to explain the brain computational capability was Donald Hebb, in his book published in 1949 [45], where he also defined his famous learning rule based on the synaptic plasticity. This prospective brought out the need of studying collective behaviors, in particular established through synchrony, of large numbers of connected neurons to treat brain large-scale operations.

In such systems, due to the presence of many coupled oscillatory elements (neurons), we expect to observe activity patterns somehow related to synchronization phenomena, as we have described in Chapter 1. Actually, synchrony in different types of neural tissues and in various brain regions have been really observed. Both *in vivo* and *in vitro* experiments on different animals and human patients, during awakeness or rest states, show synchronous patterns. Since the control role on the firing rate of a neuron at any time is performed by the inputs, which it receives from other cells or from the outside world, and by the brain self-organized activity, this implies that both these mechanisms can drive synchronization states.

Resuming the conclusions of the previous Section, as a mechanism for information transmission and signals integration [5, 53], synchronization by oscillation is considerably advantageous because of its cost-effectiveness, as it can be extended with relatively little effort to very large ensembles, and at the same time because it brings a high level of redundancy. For instance, in isolated cortical networks, which are especially susceptible to neuronal synchronization, many neurons share similar information because they share similar inputs. This redundancy can be considered as an useful security mechanism, since if some neurons fail to respond to the inputs, other cells may surely transfer the message, though it reduces the amount

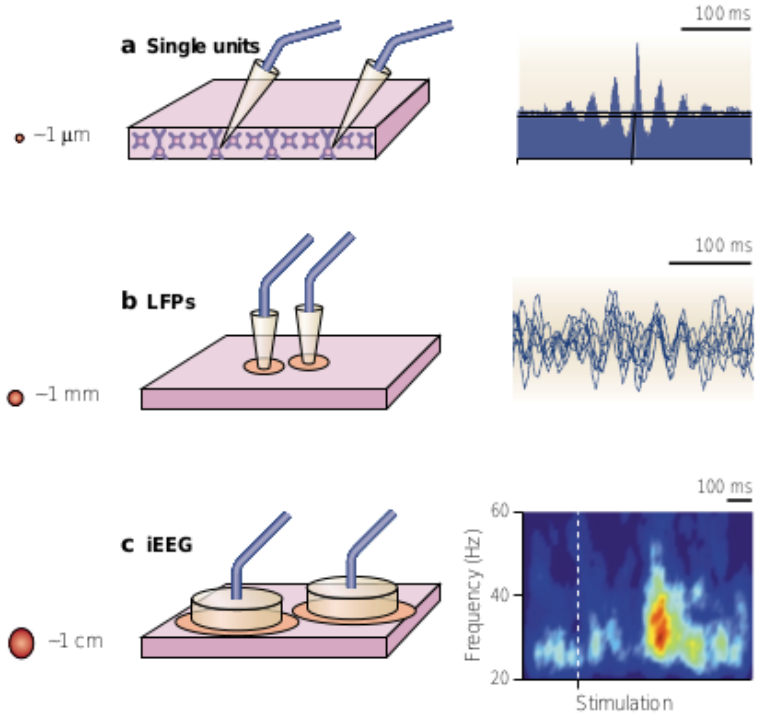

FIGURE 2.7: Schematic representation of synchronization phenomena and measure techniques in neural tissues at different spatial scales: (a) among single neurons with cross-correlations analysis, (b) among local small circuits with LFPs recordings, (c) among larger neural population with EEG measures. Image adapted from [57].

of information that can be processed by a given network [1].

Dynamics of neuronal coherence as a communication tool in nervous systems is furthermore necessary if one thinks that neurons can transfer information only through local anatomical connections, which are rather limited, while cognitive functions require a cooperation of many distant regions of the brain. Thus, the existence of an effective communication structure behind the anatomical connectivity has been supposed, being represented by patterns of phase-locking or coherence among neural groups, whose typical time scales fit to those of cognitive functions. Synchronization states, detected from fMRI images, as for example in [56], prove that neural coherence may actually be the natural way in which groups of activated neurons can communicate and interact (CTC or "communication-through-coherence" hypothesis).

In the following, we report some experimental results in which the role of synchronization in driving some functions performed by the neural network clearly emerges. This brief list does not pretend to be complete or exhaustive, presenting only some recent examples. Considering both *in vivo* and *in vitro* experiments on neural tissues, synchronization seems to determine not only positive effects and basic brain functions, since it is related for example to specific motor tasks or to memory [4] and learning processes, but also negative effects, such as pathological and harmful states in the cerebral tissues [5, 6, 58, 59]. Examples of such diseases are epileptic seizures, which are caused by slow and uniform oscillations that could last minutes and enhance neuronal excitability and synchronization, Parkinson's disease and schizophrenia.

It clearly emerges from many observations that synchronization phenomena in the nervous system can appear at many spatial and temporal scales. At each scale, specific signals can be detected and analyzed using appropriate tools as shown in Fig. 2.7. For instance, if we want to study the integration and synchronization activity of many single units, we need to focus on the temporal scale in the millisecond range and therefore to use recording methods with high

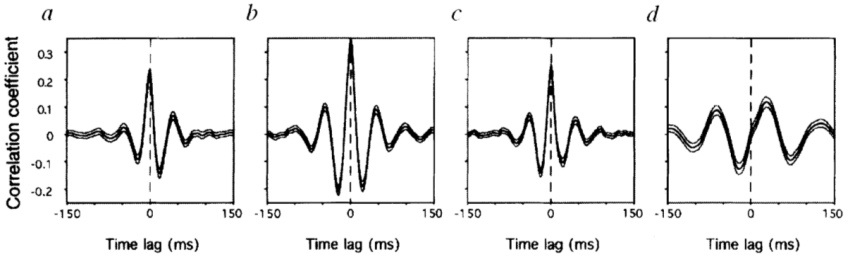

FIGURE 2.8: Synchronization patterns in cortical areas of awake cats, during task performance, detected through correlation functions among field potentials. The pronounced peaks in the correlation functions correspond to a high synchronization between the field potentials of two recorded sites. The strength of synchrony reflects the functional relations among cortical areas. Image adapted from [60].

temporal resolution [57]. From the point of view of global signals, a firing activity of many synchronous neurons gives rise to measurable fluctuations of the EEG traces, whose spectral analysis shows that neurons can oscillate synchronously in different frequency bands from less than 2 to greater than 60 Hz [53].

Evidences of phase synchrony at a local (millimeters) spatial scale as a basic mechanism for brain integration have recently been provided by extensive studies of visual-binding problem [57], which concerns how brain can link together different attributes of an object in a unified representation, since its various features, as color, texture, depth, are mapped separately in specific visual cortical areas. In those regions, excitatory and inhibitory neurons are packed in separated columns, called cortical columns, which easily synchronize each other thanks to the anatomical structure and the local connectivity. For larger (centimeters) scale, such as in neural ensembles between occipital and frontal lobes or across hemispheres, synchronization is achieved through distant connections, as cortico-cortical fibers [57].

About temporal scales, it is well known that many cognitive events take place in hundreds of milliseconds. At this time scale, a single action potential emitted by a cell is not sufficient to significantly activate a target neuron, unless this spike is synchronized with many others. This kind of spike synchrony has been really observed in neurons in cortical motor and visual areas, between the two brain hemispheres and in the hippocampus. Also coherence among LFP signals has been recorded in somatosensory and primary motor cortex and between primary and premotor areas [57, 61]. Roelfsema et al. [60] have measured synchronization states in visual, parietal and motor cortex of awake cats, using fields potential and cross-correlation analysis of these signals (see Fig. 2.8). Here, synchrony phenomena without time lags seem to be necessary to integrate pre-movement activity into a coherent representation of a final movement, while cats perform a simple task in response to visual stimuli.

Also in human patients, intracortical oscillations during the performing of a visual discrimination task show large-scale synchrony between temporal and frontal lobes [57]. Other simple visuotactile tasks are associated to gamma coherence in EEG tracings between visual and somatosensory cortices [62] or to theta oscillation in frontal and posterior cortical areas in the case of memory tasks [63]. Thanks to these and other similar results, the emergence of synchronous patterns in hippocampal, cortical and medial temporal areas has been proposed to be related to the acquisition and retrieval of memory. For instance, in [64] it is stated that neural communication facilitates both working memory and long-term memory processes, while spike timing-dependent plasticity leads to an increasing phase synchronization. Moreover, complementary mechanisms of $m : n$ phase coupling are crucial for a non-interfering representation of multiple objects in working memory.

In [65], a long-distance pattern of synchronization has been obtained in human subjects who were looking at ambiguous visual stimuli. Starting with an increase in synchrony during

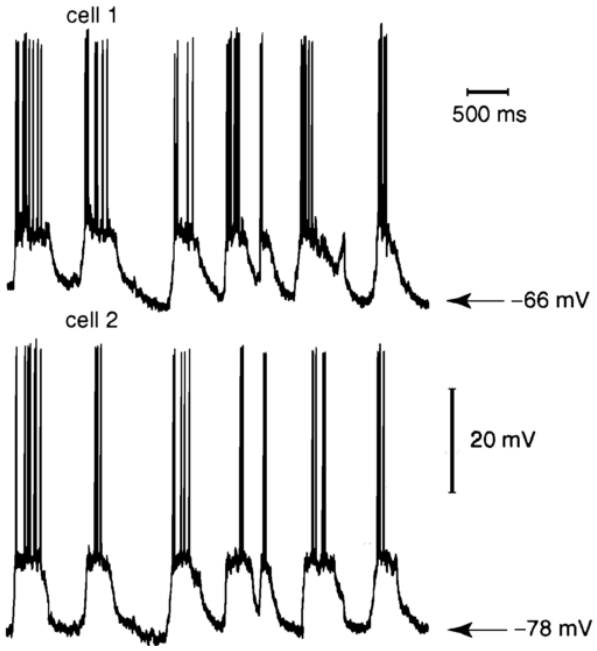

FIGURE 2.9: Synchronized 'up' and 'down' states of the membrane potential of striatal spiny neurons. 'Up' states are characterized by a fast spiking activity of neurons, while 'down' states by a subthreshold activity. Slow "up-down" fluctuations in cortical cells are correlated with a slow ($\approx$ 1 Hz) rhythm of the EEG during sleep and with the level of anesthesia. Image adapted from [67].

the perception task after stimulus presentation, this state is followed by a period of strong desynchronization, marking the transition between the moment of perception and the motor response. This represents one of the first experimental evidences to support the theory that phase synchrony and, in particular, gamma-phase synchrony is directly involved in human cognitive functions. The role of synchronization in building perceptions is also widely treated in [66].

Also during rest and slow-wave sleep, in specific neural populations in the hippocampus, strongly synchronized patterns appear as very fast transient oscillations, when in time windows of hundreds of millisecond a macroscopic fraction of the pyramidal cells fire a spike or a complex spikes burst [68]. In anesthetized animals, *in vivo* synchronization was recorded in striatal spiny neurons, which are particular inhibitory neurons located in the basal ganglia structure (subcortical group of nuclei of the vertebrates brain, responsible primarily for motor control), as reported in Fig. 2.9.

Concerning pathological states [5], very fast oscillations, observed in the hippocampus and neocortex, could be used as an indication of local epileptic seizures (see [69] and references), though the issue is even more complex if one considers that both decreases and increases in synchrony are formally related to epilepsy and seizures [70]. The symptoms of Parkinson's disease have been proved to be associated with abnormal synchronization patterns in the basal ganglia, which can be modified with high-frequency electrical stimulations [5]. Naturally, future improvements in methodological approaches, which allow a more and more non-invasive investigation of long-range synchronization in human patients with brain disorders, will provide a better understanding of such pathologies.

As a conclusion, all these experimental results concerning the role of synchronization in nervous systems show that long-range coherence in neural activity really constitutes a fundamental mechanism for implementing communication between spatially distant circuits in the

brain and for performing perceptual tasks. We can list three main consequences of these communication patterns. First, a population of neurons can evolve according to temporal scales not present in the single cell dynamics. Second, spontaneous population synchrony can emerge without any modulation of the firing rates of individual neurons. Third, mean field activities can be used as reference signals, to which the single cells activity can be related [1].

2.4 Synchronization on computational neuroscience

One of the first works which reports numerical results concerning the onset of synchronous states in oscillatory systems and in particular in systems of pulse-coupled biological oscillators was published in 1990 by R. Mirollo and S. Strogatz [71]. This paper opened a rich and productive research field, concerning numerical simulations of networks, whose dynamics try to reproduce the behavior of real neural systems in a more or less detailed way. Because of the complexity degree in describing any biological neural ensemble, from both the structural and the dynamical point of view, such an approach has immediately been shown to be highly promising.

In the following years, a wide range of numerical studies have been performed on different neural systems, investigating for instance how the network can produce coherent oscillations states during retrievals of a pattern [72], or how the presence of an inhibitory component [73] or temporal delays [74, 75] can enhance the system synchronization, while the excitatory component has a general desynchronizing effect [76, 77].

Just looking at this brief list of numerical examples, it turns out that many techniques have been used to detect synchronous or asynchronous states in networks from the computational point of view. Mirollo and Strogatz [71] simply plotted, for instance, a histogram of the number of firing units, i.e. oscillators which are emitting output signals similar to action potentials or spikes, in different time bins or the state of the system after some iterations of the return map which describes its dynamics. In [72] periodic spike bursts in coherent oscillations were observed plotting all firing events of each unit as a function of time (spike raster or raster plot), while Van Vreeswijk et al. in [73] plotted the inter-spike interval of a unit, that is the time interval between two consecutive spike events of the same unit (see Section 3.2), as a function of the previous one: points which lie on the same closed curve are synchronous. He also introduced an order parameter to measure in a more quantitative way the synchronization level of the network, finding a transition phase from a synchronous to an asynchronous regime when coupling time constants increase. In [74], synchronization states are represented by stable fixed points in the return map of the network dynamics and synchronous clusters emerge plotting the phase of each oscillator as a function of time. Finally, in [75] the main measure concerns the average value of the fluctuations of the global population voltage with respect to its mean.

More recently, in pulse-coupled networks of leaky integrate-and-fire neurons (see Section 3.2) synchronous states have been characterized by measuring the minimal and maximal values of the mean synaptic field of the network: the larger the difference between these two values, the more synchronous the system is. A similar approach appears also in [78], where networks of leaky integrate-and-fire neurons with short-term synaptic plasticity are investigated and synchronization emerges also from measures of the average inter-spike interval (as in [79]): here, synchronous neurons show constant values of their average inter-spike interval and they are therefore called locked. Computing the fraction of these locked neurons, with respect to the whole network, a diagram of a synchronization transition can be plotted, as in [79, 80].

However, despite all these approaches to synchronization in simulations of neural networks, if we think that any neuron can be globally thought as an oscillating unit, one of the most immediate measures of the synchronization level of a systems of coupled neurons which we can apply is the Kuramoto parameter (Section 1.6), as reported in [79]. To compute this

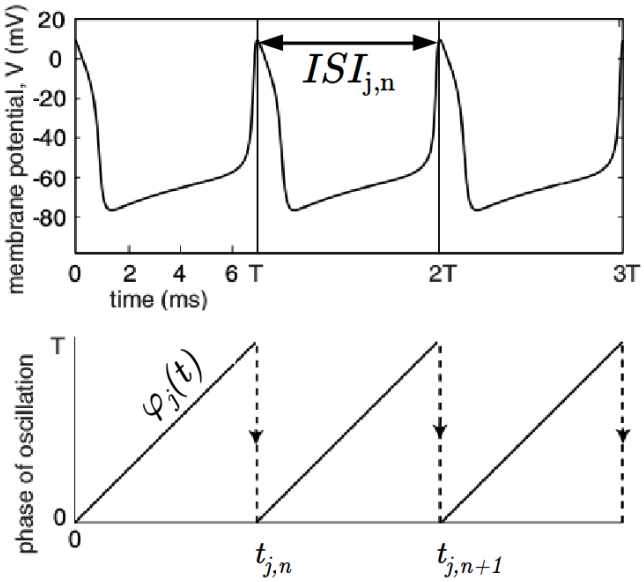

FIGURE 2.10: Schematic representation of the membrane potential of a neuron j with some action potentials or spikes (top panel). The temporal distance between two consecutive spikes at time $t_{j,n}$ and $t_{j,n+1}$ is the inter-spike interval $ISI_{j,n}$. The corresponding phase $\phi_j(t)$ (Eq. (2.1)) is plotted in the bottom panel. Image adapted from [29].

parameter we first need to assign a phase to each neural unit. Since the membrane potential periodically produces action potentials, or spikes, we can define the phase $\phi_j(t)$ of neuron j at time t as the temporal distance between t and the last spike event $t_{j,n}$ of the considered neuron, normalized with the current inter-spike interval $ISI_{j,n}$, that is the interval between the last spike at time $t_{j,n}$ and the next spike event at time $t_{j,n+1}$:

$$\phi_j(t) = 2\pi \, \frac{t - t_{j,n}}{t_{j,n+1} - t_{j,n}}, \text{ for } j = 1, ..., N \tag{2.1}$$

where the factor 2π translates this value into an angular quantity, N is the number of neurons in the system and t necessarily belongs to the interval $[t_{j,n}; t_{j,n+1})$. In Fig. 2.10, we schematically represent this phase. Computed the phase of all neurons in the network, the time-dependent Kuramoto parameter will then be defined by Eq. (1.18). In particular, considering its absolute value

$$R(t) = \left| \frac{1}{N} \sum_{j=1}^{N} e^{i\phi_j(t)} \right|, \tag{2.2}$$

we get a real parameter $R(t)$ in the interval $[0, 1]$. In this work, we refer to this definition every time we will deal with the Kuramoto parameter; while its time average, denoted as $\langle R \rangle$ or simply R, is computed as an average of $R(t)$ over a given temporal interval.

Note that, in order to compute $R(t)$ at time t during the system dynamical evolution, we should know the future spike events $t_{j,n+1}$ of each neuron with respect to t. From the numerical point of view, this is a fairly heavy computation, especially if the system evolution is slow and one needs temporal averages of $R(t)$ over large intervals. Although within certain constraints, and in particular if the dynamics is stable and uniform enough, $ISI_{j,n}$ can be simply replaced by the past inter-spike interval $ISI_{j,n-1} = t_{j,n} - t_{j,n-1}$, we have everywhere tried to apply the original definition of the Kuramoto parameter with $ISI_{j,n}$.

In the next Chapter we define our neuronal networks from the models we have chosen for the single excitatory and inhibitory neuron dynamics and the short term synaptic plasticity to the heterogeneous mean field formulation of the finite connectivity network.

Chapter 3

Dynamics of neural networks with synaptic plasticity

Once we have introduced what is synchronization in the first Chapter and we have presented some guidelines about synchronization in neurosciences from both an experimental and a computational point of view, in this Chapter we describe our neural networks model, whose elements have been characterized in Section 2.1.

Starting from some general assumptions, we introduce the leaky integrate-and-fire (LIF) equation for the membrane potential of the single cell and a phenomenological model for the short term synaptic plasticity (Tsodyks-Uziel-Markram or TUM model), which takes into account both the excitation and the inhibition synaptic mechanism. Then, we define the dynamical evolution laws of the system through an algorithm called event-driven map, which lets us easily simulate large networks. Finally, we introduce a mean field formulation, called heterogeneous mean field, which correctly reproduces the dynamics of our system in the limit of large connectivities with a very convenient approach.

3.1 Defining our neural network

In computational and theoretical neuroscience, many abstraction levels can be considered for modeling a neural population, each characterized by a given spatial and temporal resolution and endowed with a dynamical description of biophysical interactions, based on the details richness one wants to manage.

We can distinguish different description levels [81]. At the microscopic scale, one can formulate very detailed biophysical models for the single cell behavior, which for instance refers to the opening/closing mechanisms of the membrane ionic channels in generating action potentials or to the synaptic vesicles dynamics in spikes transmission. Because of the highly complex biological processes which have to be taken into account at this level, this class of models need large amounts of dynamical variables and equations, whose mathematical integration becomes too complicated to be applied to extensive neural ensembles. The following abstraction level is the morphological one, which concerns the transmission of signals along axons and dendrites, defining models such as cable equations, Rall model, multi-compartment models, still highly detailed from the biological point of view. The spatial resolution which can be reached in this class of models is of the order of micrometers, lower than the previous one (~ 10 nm), while the temporal scale of the biological processes they describe is of the order of milliseconds. Climbing again, we reach the cellular level. Here, neurons can be considered as single dynamical units, point particles, whose state is described by a simple global variable, such as the membrane potential, and they are connected to each other by schematic links representing the synapses. Since we are no more interested in the specific dynamics of each ion channel or neurotransmitter, but rather in the global behavior of the cell or the synapse, we can now

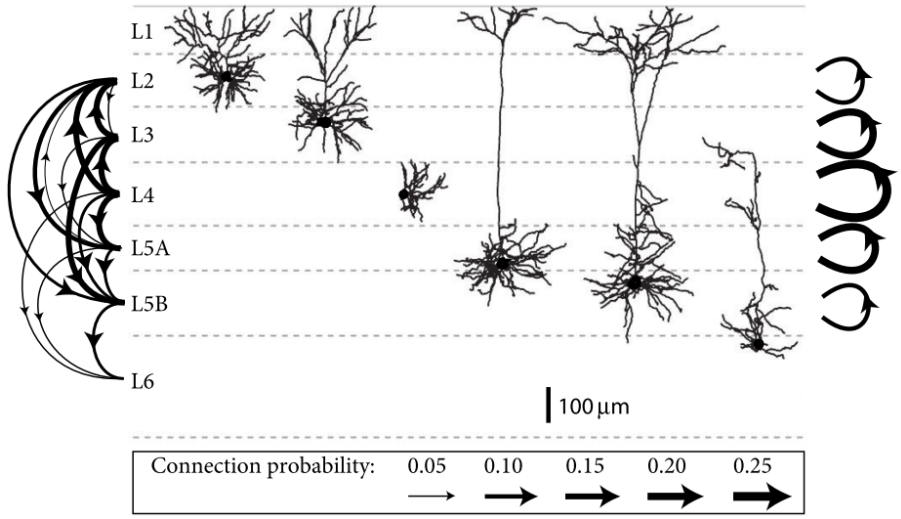

FIGURE 3.1: Typical connectivity patterns and shapes of excitatory neurons of cortical columns in the somatosensory cortex of the mouse. Arrows on the left indicate connection probabilities among neurons across layers, while arrows on the right show connection probabilities among neurons within the same layer. Image from [81].

quite cheaply simulate a large number of neurons, creating a self-consistent subpopulation and reaching a spatial resolution of tens of micrometers.

Increasing the size of this subsystem, we enter the mesoscopic description scale, where we are able to simulate an entire neural population with hundreds or thousands of neurons, characterized by a local connectivity. Linking together different nervous populations with long-range connections, we get interacting populations and, with a further abstraction, multiple layers networks. Again, at the macroscopic scale of hundreds of micrometers, using quite sophisticated field models, multiple columns dynamics can be simulated, performing simple learning, retrieval and memory tasks. Finally, whole brain regions may be taken into account, reaching a spatial resolution of the order of the centimeters.

Neural networks discussed in this work refer to the cellular description level. In literature, models at the cellular level are mainly employed to study neural ensembles of the neocortex, where neurons are organized in highly coupled cylindrical columns, divided in six vertical layers. These structures are basic functional units of the cerebral cortex, endowed with the so-called feed-forward and top-down connections (among columns or towards other brain regions) and dense recurrent connections (among neurons or layers within the same column), as shown in Fig. 3.1 [40].

At this cellular level, we will describe neurons dynamics through one of the main classes of models for neurons [82], that is a spiking model, which allows us to analyze the spike trains of individuals neurons [81] and to represent the whole neural activity of our network reporting the spike train of each neuron as a function of time [81], as for example it is shown in Fig. 3.2. Such a plot is typically called raster plot: each spike corresponds to a dot and neurons are ordered on y axis according to their index. Examples of raster plots snapped out during the simulations of our neural networks can be found in the next Chapter.

Once defined the single neuron dynamics, which describes how the cell generates its action potential, we need to add a coupling dynamics among neurons, which controls the transmission mechanism of spikes from a presynaptic to a postsynaptic unit, assuming that the postsynaptic response to a presynaptic action potential is instantaneous. Neuron dynamics and synaptic coupling will be presented, respectively, in Section 3.2 and Section 3.3.

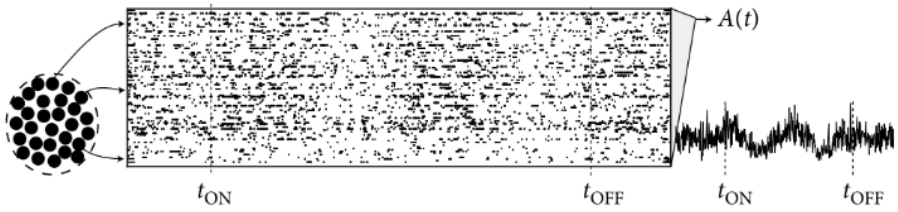

FIGURE 3.2: Raster plot of a population of spiking neurons. Each dot in this plot represents as a function of time the spike event of a neuron. $A(t)$ is the population activity and can be computed counting the spikes which are present in given time bins, averaged over all neurons. Image adapted from [81].

Before going on, let us clearly specify some general assumptions we have done about our neural networks:

- We investigate networks which represent single populations of coupled neurons, treated as point particles. We will consider both excitatory (Chapter 4) and inhibitory (Chapter 5) integrate-and-fire neurons (Section 3.2), randomly connected to each other only through chemical synapses, characterized by short term synaptic plasticity (Section 3.3).

- Our neural networks are represented as graphs, whose nodes correspond to neurons and links or edges to synapses. Its adjacency matrix $\mathcal{A} = \{\epsilon_{ij}\}$ describes all the links of the network, setting for each unit i the neurons from which i receives inputs and the neurons to which i sends outputs. More precisely, in a purely excitatory network, that is in a network with only excitatory neurons, $\epsilon_{ij} = 0$ if there are not synapses between i and j, $\epsilon_{ij} = 1$ if there is a link between i and j and in particular if j (presynaptic neuron) can send its action potentials to i (postsynaptic neuron). From here on, any variable with these two indices will follow this notation, that is $\square_{ij}$ will mean $\square_{i \leftarrow j}$.

- The neural connectivity we consider is the anatomical connectivity. Indeed, large-scale brain networks can be described with three different levels of connectivity, which are mutually interrelated [83]. First, anatomical or structural connectivity is the set of physical or structural connections (synapses) among single neurons (local circuits) or neural populations in different brain regions. These connections are relatively static at shorter time scales (from seconds to minutes), but synapses can be created or deleted, becoming dynamic, at longer time scales (from hours to days), as for example during learning or reinforcement processes. Second, functional connectivity represents the statistical dependencies between spatially distant neuronal units and measures with different methods their correlation, spectral coherence or phase-locking. Typical time scales for the dynamics of functional connectivity are of the order of hundreds of milliseconds. Third, effective connectivity represents causal interactions among large-scale regions. Experimentally, this connectivity can be obtained through observations of the temporal ordering of neural events. As the functional structure, it is not static, but it reflects the interaction of various subregions of brain in performing different cognitive tasks or behavioral states.

- All neurons have an equal time-independent threshold value for spikes emission and modulation mechanism of synaptic strength, accommodation of the threshold, non-additive interactions among multiple synaptic inputs or the refractory period after spiking are not included. All these restrictions are largely compensated by the extreme simplicity of their dynamics, which allows us to integrate and simulate at the same time a large amount of neurons.

- Neural activity in our networks is endogenous, that is the population activity is self-produced. This is a reasonable assumption, since we mainly refers to cortical neural

ensembles. In such regions, continuous spontaneous firing activity of neurons, once isolated from the rest of the brain and without any external sensory stimulus, has been experimentally proved both *in vivo* and *in vitro* (see for example [3, 58, 84]) and theoretically investigated on random networks since the 1960s [46].

- Any real neural network is realistically represented by as a spatial weighted evolving network (see Appendix A). A cortical system is an intrinsically spatial network, as each neuron is in a specific position, more or less distant from other neurons. These distances directly influence the transmission of electrical signals, which can be delayed, due to possible dispersions phenomena along axons and dendrites. However, since we consider local networks, where transmission delays are negligible and spikes run instantaneously from the presynaptic to the postsynaptic unit, we do not need to consider spatial networks. A cortical system should be represented by a weighted network, where the weight associated to each link would correspond to the efficacy of the relative synapse (see Section 2.1): the stronger a synapse is, thanks to its plasticity and reinforcement processes, the higher its weight parameter becomes. However, in the mean field formulation that we introduce in our model in Section 3.5, these synaptic weights are absorbed in the number of connections of each node, so that for simplicity we can assume unweighted networks, where the elements ϵ_{ij} of the adjacency matrix can only be 0 or 1. Finally, a real cortical network is an evolving system from the anatomical connectivity point of view, since new synapses can be continuously created or the old ones can die, modifying the anatomical structure [3]. In our networks, the topology is always fixed and no link is added or removed during the dynamic evolution. As stated above, if we suppose that these formation or deletion processes take place on much longer time scales than spikes generation and transmission and than the typical time scales of the short term synaptic plasticity, we can easily justify this approximation of fixed anatomical connectivity.

3.2 Single neuron dynamics (LIF model)

As argued in the previous Section, our work deals with spiking neural networks models. The first necessary element for such networks is a spiking neuron, that is a neuron able to emits an action potential through a discontinuous membrane dynamics. Typical single neuron models characterized by this property are the so-called integrate-and-fire models, which are single-compartment models [40], since they describe the membrane potential of a neuron with a single variable.

Integrate-and-fire neurons are relatively recent and are considered the simplest models able to define the dynamics of the membrane potential and, with a simple artificial rule, the mechanism for generating spikes. If one wants to describe the onset of action potentials from a more detailed biophysical point of view, in terms of non trivial interaction among nonlinear ionic currents, mediated by voltage-gated ion channels, more realistic and highly dimensional models should be taken into account. Among them, we find the first historically proposed model for the neuron membrane, published in 1952 [85], one of the breakthroughs of computational neuroscience for which A. Hodgkin and A. Huxley won the Nobel prize in 1963. After a series of experiments on the squid giant axon, they worked out a complex but relatively complete mathematical model which describes how membrane potential, conductances and ionic currents interact and determine spikes emission. It assumes that cell membranes behave as parallel electrical circuits, as reported in Fig. 3.3(a), with time-dependent resistors R_{Na}, R_K, R_L, which correspond to the ionic permeabilities of the membrane (in particular for potassium and sodium ions), a capacitor C_M, which represents its phospholipid bilayer accumulating ionic charges, and voltage batteries E_{Na}, E_K, E_L, which simulate the electrochemical driving forces [29, 86].

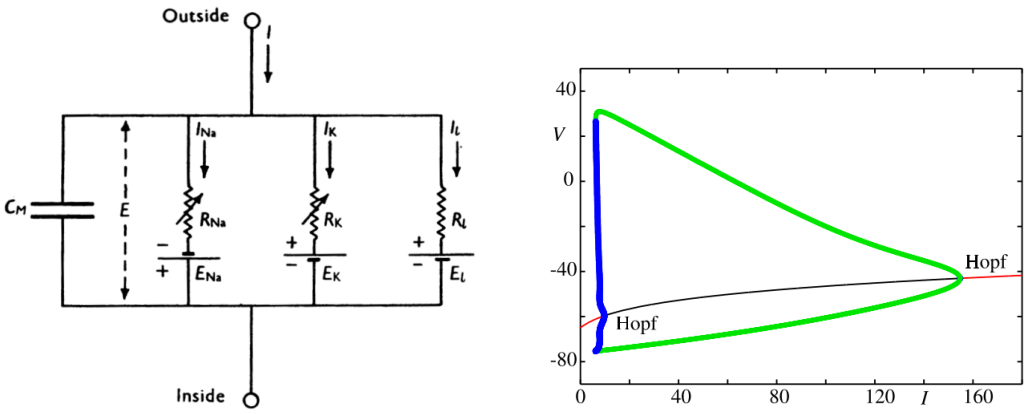

(a) (b)

FIGURE 3.3: (a) Equivalent electrical circuit, representing membrane dynamics of a neuron. Image from [85]. (b) Bifurcation diagram of the Hodgkin–Huxley model as a function of the external current I. V is the membrane potential. The green lines show the amplitude of a stable limit cycle, while the blue lines unstable limit-cycle behaviour, both born from Hopf bifurcations. The solid red (black) line shows the stable (unstable) fixed point. Image from [86].

Since the complete description of a Hodgkin-Huxley neuron requires 4 dynamical variables and a set of 4 coupled ordinary differential equations, computational analyses are quite heavy. Easier later models were proposed in 1961-1962 by R. FitzHugh [87] and J. Nagumo [88] in 1981 and in 1981 by C. Morris and H. Lecar [41, 89], to describe voltage oscillations in the barnacle giant muscle fiber. Both models are based on only 2 dynamical variables and on the interpretation of the cell membrane as an electronic circuits.

Integrate-and-fire models represent a further simplification, since their only variable is the membrane potential $V(t)$. As phenomenological model of neuronal dynamics, first of all they are able to sum, let's say they "integrate", all the inputs received by the cell at each time, and then to trigger an action potential, let's say they "fire" [81]. For integrating signals and evolving $V(t)$ we need one equation; for firing we need to define a threshold potential V_{th} so that if $V(t)$ exceeds the threshold, the neuron emits its action potential. As we can capture the global neural dynamics with one simple ordinary differential equation, an integrate-and-fire model is what we need for simulating networks with thousands of neurons, where all action potentials have the same negligible shape and are considered as discrete spike "events".

In particular, in this work we consider one of the most common integrate-and-fire models, called leaky integrate-and-fire or LIF neuron [40, 41, 43, 81]. This model was first proposed by L. Lapicque in 1907, before the main findings about the mechanisms responsible for the generation of action potentials [90, 91]. As for the previous mentioned models, also a LIF neuron can be represented by a simple parallel circuit with a capacitor C and a resistor R (RC parallel circuit, see in Fig. 3.4(a)). Using Kirchhoff's and Ohm's laws and other basic formulas of electronics, the total current $I(t)$, which enters the circuit, splits into two component $I(t) = I_R + I_C$. The first (second) current is the resistive (capacitive) term which passes through the resistor (capacitor). From their definitions, we get

$$I(t) = \frac{V(t) - V_R}{R} + C\frac{dV(t)}{dt}, \tag{3.1}$$

where $V(t)$ is the membrane potential, V_R is its rest or reset value and the current $I(t)$ can either be an external current (given by a stimulus) or a synaptic input from presynaptic neurons. The resistive current is the dissipative term of this equation; it is also called ohmic leakage current:

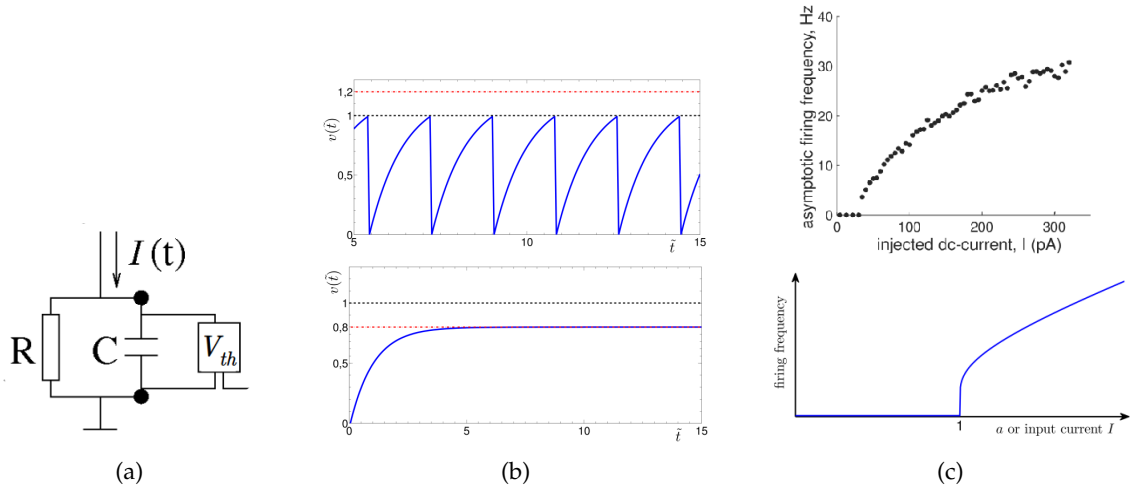

(a) (b) (c)

FIGURE 3.4: (a) Equivalent electrical circuit for the dynamics of the single neuron membrane potential. The external element V_{th} represents the firing threshold. Image adapted from [41]. (b) Membrane potential dynamics in the LIF model for $a = 1.2$ (top panel, spiking regime) and for $a = 0.8$ (bottom panel, not spiking regime). The dashed black line represents the threshold value $v_{th} = 1$. Every time the potential reaches the threshold value, a spike is emitted (not shown). Time and potential are adimensional variables, according to Eq. (3.6). (c) Frequency-current (F-I) curve, namely firing frequency F of a neuron as a function of the injecting current I. We show in the top panel experimental data, recorded for pyramidal neurons from rat primary visual cortex (image adapted from [29]) and in the bottom panel the theoretical curve computed from the LIF model in Eq. (3.10).

this is why we call this model leaky integrate-and-fire neuron.

Then, we introduce the characteristic time constant of this RC circuit $\tau_m = RC$ ('m' stands for membrane) and we suppose to have a constant external current $I(t) = I$:

$$\tau_m \frac{dV(t)}{dt} = RI - (V(t) - V_R). \tag{3.2}$$

Adding a reset rule to model the spike generation, we obtain a final spiking neuron: when the membrane potential $V(t)$ exceeds the threshold value V_{th}, equal for all neurons and time-independent, the neuron is said to fire an action potential, and its potential is reset to the rest value V_R, that is

$$\text{if } V(t) \geq V_{th} \ \rightarrow V(t) = V_R \ + \ \text{spike emission}. \tag{3.3}$$

All parameters can be set to their physiological values, according to the type of neuron which one considers. For instance, for a typical cortical neuron we get $V_R \sim -65$mV, $\tau_m = 10$ms, $V_{th} \sim -50$mV, $R \sim 10^7\Omega$ [40, 43, 86]. In order to get rid of the dependence of the model on the specific values associated to each parameter, it is now convenient to appropriately rescale time and voltage variables, so that Eq. (3.3) assumes a simpler adimensional formulation:

$$t \ \rightarrow \ t/\tau_m \tag{3.4}$$

$$v \ = \ \frac{V - V_R}{V_{th} - V_R}; \ a = \frac{RI}{V_{th} - V_R} \tag{3.5}$$

$$\dot{v} \ = \ a - v, \tag{3.6}$$

where $\dot{v} = \frac{dv}{dt}$ and a is the correctly rescaled leakage current. In this framework, the threshold value is $v_{th} = 1$, while the reset value $v_R = 0$ and, looking at the above biological values,

one adimensional time unit corresponds to a time interval of about 10 ms. Solving Eq. (3.6), the continuous subthreshold behavior of the neuron yields

$$v = a(1 - e^{-t}), \text{ with the resetting rule } v(t) = 0 \text{ if } v(t) \geq 1. \tag{3.7}$$

The resting state of such a neuron is $v = a$: this implies that is for $a > 1$, the neuron is not spiking, since it will never be able to reach the firing threshold. For $a \geq 1$, namely for the leakage current greater than the threshold value, the neuron is in the so-called spiking regime, since its potential can exceed the threshold and generates an action potential, as shown in Fig. 3.4(b). This produces periodic oscillation between the threshold and the reset values, whose period can be computed solving Eq. (3.6) for $v_1 = 0$ and $v_2 = 1$:

$$v_1 = 0 \to 0 = a(1 - e^{-t_1}) \to t_1 = 0 \tag{3.8}$$

$$v_2 = 0 \to 1 = a(1 - e^{-t_2}) \to t_2 = ln\left(\frac{a}{1-a}\right) \tag{3.9}$$

$$T = t_2 - t_1 = ln\left(\frac{a}{1-a}\right). \tag{3.10}$$

The time interval between two consecutive spikes by the same neuron will be called from now on inter-spike interval or ISI. The $ISI(t)$ of a neuron is generally time-dependent. Together with raster plots (Section 2.4), plots of the average value of $ISI(t)$ of a neuron, or $\langle ISI \rangle$, as a function of the number of nodes from which it receives input spikes, that is its in-degree (Section 3.1), have been largely used in this work to define the dynamical properties of the network (see Chapter 4 and Chapter 5).

From the analytical result in Eq. (3.10), we can compute the firing frequency (inverse of period T) as a function of the parameter a or the external input current I, getting the F-I curve. We report the typical functional form of this curve for the LIF neuron in Fig. 3.4(c) (bottom panel) and we compare it with experimental measures on pyramidal cortical neurons (top panel). Such a F-I curve implies that the neuron actually translates the strength of an input into the frequency of spiking: the higher the input signal, the higher the neuron firing rate is. Even very weak inputs get the neuron fire though with low frequencies [29]. Referring to the classification proposed by Hodgkin in 1948, these features place the LIF neuron in the class I of neural excitability, which is characterized by a wide range (two order or magnitude) of possible frequency rates [29].

Although this is a quite elementary model, a LIF neuron encodes specific properties of real cells, necessary in our model. In particular, it can distinguish between an excitation and an inhibition process, since positive inputs $I > 0$ increase the membrane potential towards the threshold, while negative inputs decrease it, as we will see in Section 3.4.

Many extensions to the LIF model have been proposed, as the nonlinear or quadratic integrate-and-fire neuron or the resonate-and-fire (generalized integrate-and-fire) models. They can represent more realistically than a LIF equation the membrane potential dynamics of neurons but require higher computational costs and therefore we have rejected them. On the contrary, though it is not so realistic, its extreme simplicity makes LIF neuron an ideal candidate for the single cell dynamics, with clear dynamical properties, easy to be analytically treated and numerically computed in our work.

In the next Section, we will define the coupling dynamics among LIF neurons.

3.3 Short term synaptic plasticity (TUM model)

In Section 2.1, it is shown how neurons interact with each other through synapses, exchanging action potentials. Now, we need to model the dynamical behavior of such synapses and in

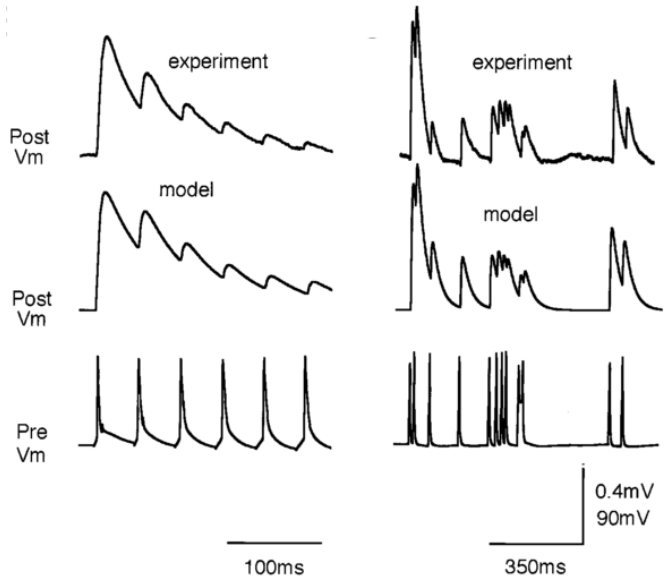

FIGURE 3.5: PSP generated by two different spike trains (bottom, regular on the left and irregular on the right) measured experimentally (top) and computed with the model (middle). Image adapted from [92].

particular chemical synapses. The transmission of an action potential through such a synapse is driven by the neurotransmitters, which bind to the postsynaptic ion channels or to receptors of ion channels. The following opening of those channels changes the conductance of postsynaptic neuron and produces a postsynaptic potential (PSP). Conductance models for synapses describe this transmission with a simple dynamical equation of the probability that a channel opens after a given number of neurotransmitters has reached it [40].

Since we are interested in modeling short term synaptic plasticity of chemical synapses, namely the capacity of this synapse to modify its conductance due to its activity history for short time scales (from milliseconds to tens of seconds), instead of considering dynamical equations for the opening probability, we can directly describe the modification in the neurotransmitters release from the presynaptic neurons. There exist two types of short term plasticity: short term synaptic depression and short term synaptic facilitation. The first mechanism takes place when a presynaptic spike train produces a series of PSP decreasing in amplitude, as if the synapse was depressed, and this typically occurs among excitatory pyramidal cells of the somatosensory cortex. The second mechanism yields an increasing PSP series, as it the synapse facilitated the signal transmission, and this is typical between a presynaptic pyramidal cell and a cortical inhibitory interneuron. In general, facilitation and depression are characterized by different time scales [3, 40].

As a model of short term synaptic plasticity, including both depression and facilitation mechanisms, we have chosen the theory proposed in 1997 by M. Tsodyks and H. Markram [92]. It is a phenomenological model of cortical synapses, which is able to correctly reproduce with a good approximation the synaptic responses between pyramidal neurons [93], as shown in figure Fig. 3.5, and some biophysical mechanisms of synaptic depression, such as receptor desensitization or depletion of synaptic vesicles. According to this model, each synapses is characterized by a given amount of resources, partitioned into three states: available, active and inactive.

Let's consider the generic synapse between the presynaptic neuron j and the postsynaptic neuron i. Dividing the number of resources by the total amount of resources, we get available, active and inactive resources fractions that will be denoted as x_{ij}, y_{ij} and z_{ij}, respectively, with $0 \leq x_{ij} \leq 1, 0 \leq y_{ij} \leq 1$ and $0 \leq z_{ij} \leq 1$. These fractions continuously change in time, due to

action potentials transmission through the synapse, but the total amount of resources, that is $x_{ji} + y_{ji} + z_{ji}$, is conserved and normalized to 1. The kinetic equation of each fraction reads

$$\dot{y}_{ij} = -\frac{y_{ij}}{\tau_{in}} + u_{ij}x_{ij}(t)S_j(t) \tag{3.11}$$

$$\dot{x}_{ij} = \frac{z_{ij}}{\tau_r} - u_{ij}x_{ij}(t)S_j(t) \tag{3.12}$$

$$\dot{z}_{ij} = \frac{y_{ij}}{\tau_{in}} - \frac{z_{ij}}{\tau_r} \tag{3.13}$$

$$x_{ij} + y_{ij} + z_{ij} = 1, \tag{3.14}$$

where the constant u_{ij} is the utilization of synaptic efficacy parameter and the last row is the conservation law. $S_j(t)$ represents the spike train of the presynaptic neuron j. Since we are not interested in the specific shape of action potentials emitted by a neuron, we assume identical and instantaneous action potentials for all neurons. For these reasons, each spike can be approximated as a Dirac δ function and the complete spike train $S_j(t)$ can be written as a linear sum of Dirac δ functions:

$$S_j(t) = \sum_n \delta(t - t_{j,n}), \tag{3.15}$$

where $t_{j,n}$ is the time in which neuron j emits its $n-$th action potential.

In these equations, the dynamics is characterized by two main time constants: the inactivation time constant τ_{in} and the recovery time constant τ_r^i. For cortical synapses the recovery time is much larger (typically of the order of 1 second) than the inactivation one (few milliseconds).

If in a generic time interval $[t_1, t_2]$ neuron j does not spike any action potential, that is $S_j(t) = 0,\ \forall t \in [t_1, t_2]$, the active resources y_{ij} exponentially decay in the inactive state z_{ij} with a time constant τ_{in}, while the inactive resources are exponentially recovered and fall in the available state x_{ij} with a time constant τ_r. This not spiking dynamics continues until all the active resources run out and the synapse dies. Otherwise, when neuron j emits a spike at time time t, that is $S_j(t) = 1$, a fraction of available resources x_{ij}, proportional to the parameter u_{ij}, becomes active with a discontinuous jump, as if the synapse recharged. The final current produced in the postsynaptic neurons is proportional to the fraction of active resources.

To include the short term facilitation mechanism, we need to introduce the facilitation factor, proposed in 1998 by M. Tsodyks, K. Pawelzik and H. Markram [94], which increases at each spike arrival and decays between spikes. To do that, it is sufficient assuming that u_{ij} is no longer a time-independent parameter, but rather it is described by a further equation as follows:

$$\dot{u}_{ij} = -\frac{u_{ij}}{\tau_f} + U_f\,(1 - u_{ij})S_j(t), \tag{3.16}$$

where τ_f is a new time constant, called facilitation time, and U_f is a time-independent parameter. According to this equation, u_{ij} grows fast if the spiking rate on a neuron is high. In a not spiking regime, u_{ij} exponentially decays with a time constant τ_f, which is typically larger than the inactivation time and shorter than the recovery one, while during a spike it instantaneously increases of a fixed amount U_f.

As mentioned above, since among excitatory cells the synaptic transmission is mainly characterized by short term depression, in a purely excitatory network we expect that $\tau_f \to 0$ and $u_{ij} = constant = U_f$, while u_{ij} evolves according to Eq. (3.16) if we have both excitatory and inhibitory neurons, so that both depression and facilitation mechanisms are taken into account. In this last case τ_r is supposed to depend on the nature of the postsynaptic neuron, so that we will have one recovery time constant for excitatory postsynaptic neurons τ_r^E and one for inhibitory postsynaptic neurons τ_r^I [10].

The full set of ordinary differential equations of this model now reads

$$\dot{y}_{ij} = -\frac{y_{ij}}{\tau_{in}} + u_{ij}x_{ij}(t)S_j(t) \tag{3.17}$$

$$\dot{x}_{ij} = \frac{z_{ij}}{\tau_r^{E,I}} - u_{ij}x_{ij}(t)S_j(t) \tag{3.18}$$

$$\dot{z}_{ij} = \frac{y_{ij}}{\tau_{in}} - \frac{z_{ij}}{\tau_r^{E,I}} \tag{3.19}$$

$$x_{ij} + y_{ij} + z_{ij} = 1 \tag{3.20}$$

$$u_{ij} = U_f, \text{ if } i \text{ is excitatory} \tag{3.21}$$

$$\dot{u}_{ij} = -\frac{u_{ij}}{\tau_f} + U_f\,(1-u_{ij})S_j(t), \text{ if } i \text{ is inhibitory.} \tag{3.22}$$

In this final configuration, this model is often referred as the TUM model for the short term synaptic plasticity, from the initial letters of Tsodyks, Uziel and Markram. Numerical values assigned to all the synaptic parameters are extracted from their paper [10] or from [95] and they have to be properly rescaled to get more general adimensional equations, as shown for Eq. (3.6).

In the next Section, we will see how to embed this synaptic dynamics in the single LIF neuron presented in Section 3.2, in order to finally build our coupled neural network.

3.4 Neural dynamics with finite connectivity

The single cell dynamics described by the final formulation of the adimensional LIF neuron (Eq. (3.6)) is an isolated dynamical units, since no external current which can play the role of synaptic inputs received from other neurons is included.

Since each signal transmission among neurons is set by the coupling dynamics proposed by TUM model, following [10] we have supposed that the synaptic current $I_{syn,i}(t)$, entering the postsynaptic neuron i, is a sum of presynaptic currents from all the j neurons connected to i:

$$\dot{v}_i = a - v_i + I_{syn,i}(t) = a - v_i + \sum_{j=1}^{N} A_{ij}y_{ij}(t), \tag{3.23}$$

where the sum includes all neurons of the network (assuming an all-to-all connectivity pattern), $y_{ij}(t)$ is the active resources fraction for the synapse between i and j and A_{ij} is the synaptic efficacy parameter: the higher this efficacy parameter, the higher the postsynaptic current and the stronger the synaptic transmission are. For simplicity, we adopt a constant and equal value $A_{ij} = g$ for each synapse and we take it out from the sum. Therefore, the efficacy of the synapse depends only on how many neurons j are connected to i. From a dynamical systems point of view, g represents the coupling constant among single units. Accordingly, we can rewrite the previous expression of the synaptic current as:

$$I_{syn,i}(t) = \frac{g}{\langle k_{in}\rangle}\sum_{j=1}^{N}\epsilon_{ij}y_{ij}(t), \tag{3.24}$$

where ϵ_{ij} is the generic element of the adjacency matrix (Appendix A), with $\epsilon_{ij} = 0$ or $\epsilon_{ij} = 1$.

A sum along the $j-$th column or a sum along the $i-$th row of the adjacency matrix will respectively yield the output degree of node j, that is the number of neurons to which j directs its spike, and the input degree of node i, that is the number of neurons from which i receives

spikes (Appendix A):

$$k_{in} = \sum_{i=1}^{N} \epsilon_{ij}; \quad k_{out} = \sum_{j=1}^{N} \epsilon_{ij}. \tag{3.25}$$

Then, the total degree of node i will be the sum of its input and output degree. that is $k_i = k_{in,i} + k_{out,i}$.

Since we consider graphs where the degree k_i of each node typically scales with the size N of the system, the sum in Eq. (3.24) could diverge in the thermodynamic limit of $N \to \infty$. Therefore, to keep this model well-defined also in that case, the coupling constant g has to be properly normalized: this is why we divide it by the average input degree of the network $\langle k_{in} \rangle$.

The synaptic current $I_{syn,i}(t)$ can be also referred as the local field $Y_i(t)$ perceived by neuron i as a result of all its presynaptic units, from which it receives a spike, or more precisely:

$$I_{syn,i}(t) = gY_i(t). \tag{3.26}$$

As emerges in [10], for a purely excitatory network the state of synapse $i \leftarrow j$ depends only on the past state of the presynaptic neuron, so that we are allowed to rewrite Eqs. (3.17-3.21) with the only presynaptic j index, as if the synapse variables x_{ij}, y_{ij}, z_{ij} and u_{ij} were actually node variables x_j, y_j, z_j and $u_j = U_f$.

Joining the Equations set (3.17-3.21) to Eq. (3.23) and Eq. (3.24), we finally get:

$$\begin{cases} \dot{v}_i &= a - v_i + \frac{g}{\langle k_{in} \rangle} \sum_{j=1}^{N} \epsilon_{ij} y_j(t) \\ \dot{y}_i &= -\frac{y_i}{\tau_{in}} + U_f(1 - y_i - z_i) S_i(t) \\ \dot{z}_i &= \frac{y_i}{\tau_{in}} - \frac{z_i}{\tau_r^E} \quad \text{for } i = 1, ..., N, \end{cases} \tag{3.27}$$

where the conservation law of synaptic resources has been used to define $x_i = 1 - y_i - z_i$ and $\langle k_{in} \rangle$ is the average input degree. A system with N neurons will correspond to a set of $3N$ coupled ordinary differential equations.

For an excitatory and inhibitory network, we need to specify if the $i-$th node is excitatory (E) or inhibitory (I) and if its resources are sent to an excitatory or to an inhibitory neuron. Therefore, the Equations set of the model in this case becomes

$$\begin{cases} \dot{v_i}^{(\dagger,*)} &= a - v_i^{(\dagger,*)} + \frac{g}{\langle k_{in} \rangle} \sum_{j=1}^{N} \epsilon_{ij}\, y_j^{(\dagger,*)}(t) \\ \dot{y}_i^{(\dagger,*)} &= -\frac{y_i^{(\dagger,*)}}{\tau_{in}} + u_i^{(\dagger,*)}(1 - y_i^{(\dagger,*)} - z_i^{(\dagger,*)}) S_i^*(t) \\ \dot{z}_i^{(\dagger,*)} &= \frac{y_i^{(\dagger,*)}}{\tau_{in}} - \frac{z_i^{(\dagger,*)}}{\tau_r^\dagger} \\ u_i^{(E,*)} &= U_f \\ \dot{u}_i^{(I,*)} &= -\frac{u_i^{(I,*)}}{\tau_f} + U_f\,(1 - u_i^{(I,*)}) S_i^*(t), \quad \text{for } i = 1, ..., N, \end{cases} \tag{3.28}$$

where the superscript symbol $* = E, I$ denotes what type is the $i-$th site, while $\dagger = E, I$ denotes what type is the postsynaptic node. Here, the adjacency matrix element ϵ_{ij} is zero if i and j are not connected one to each other, $\epsilon_{ij} = 1$ if i and j are linked and the presynaptic neuron j is excitatory and $\epsilon_{ij} = -1$ if the presynaptic neuron j is inhibitory. Such a choice comes from the fact that now each neuron i typically receives some inputs coming from presynaptic excitatory units and some others from inhibitory units. The latter will move its potential away from the threshold value, as if they added a negative contribution to the synaptic current $I_{syn,i}(t)$, while the former will bring it closer to the threshold, as a positive term was added to $I_{syn,i}(t)$. Note that in this case the input and output degree of the $i-$th node is still a sum along the $i-$th row and the $i-$th column of this matrix, but taking the absolute value of ϵ_{ij}.

As reported in the previous Section, numerical values of all parameters in Eqs. (3.27) and Eqs. (3.28) are typically assigned according to some accepted biophysical reference values for cortical neural networks [96, 97] and in particular we follow what is reported in [10]: $\tau_m = 15 - 30$ ms, $\tau_{in} = 3$ ms, $\tau_r^E = 800$ ms, $\tau_r^I = 100$ ms, $\tau_f = 1000$ ms, $V_{th} = 15$ mV, $V_R = 13.5$ mV, $A_{mean} \sim 5$ mV. After a proper rescaling, our final adimensional values are:

$$\begin{cases} \tau_{in} = 0.2 \\ \tau_r^E = 133 \cdot \tau_{in} \\ \tau_r^I = 17 \cdot \tau_{in} \\ \tau_f = 33.25 \\ g = 30 \\ U_f = 0.5 \\ a = 1.3 \end{cases} \tag{3.29}$$

Unless otherwise specified, all the numerical simulations we have performed refer to the above values. In particular we will never vary the inactivation time τ_{in}. Interesting results concerning how the behavior of the purely excitatory network described in Eqs. (3.27) changes as function of τ_{in} can be found in [79, 98].

Let's now consider the purely excitatory network. Its dynamics can be decomposed in a continuous behavior in between two consecutive action potentials, which can be emitted by any neurons, and in discrete events or spikes. In the continuous phase, namely in the time interval $\tau(n) = t_{n+1} - t_n$, where t_{n+1} and t_n are respectively the time instant immediately after the $(n+1)-$th and $n-$th spike of the network ($S_j(t) = 0,\ \forall t \in [t_n, t_{n+1})$), Eqs. (3.27) can be exactly integrated. We will refer to $\tau(n)$ also as the ISI of the network at the $n-$th time step. Then, when a spike is emitted, we need to update in a discontinuous way all the variables.

Since our main goal is to numerically simulate such a dynamics, it is particularly convenient to write a map, which yields the values of v_i, y_i and z_i at the $(n+1)-$th time step as a function of the previous step (for convenience, we denote the time step as n instead of t_n). After some mathematical derivations, this map reads:

$$y_i(n+1) = y_i(n)e^{-\frac{\tau(n)}{\tau_{in}}} + u\left[1 - \frac{\tau_r^E}{\tau_r^E - \tau_{in}} y_i(n)\left(e^{-\frac{\tau(n)}{\tau_r^E}} - \frac{\tau_{in}}{\tau_r^E} e^{-\frac{\tau(n)}{\tau_{in}}}\right) - z_i(n)e^{-\frac{\tau(n)}{\tau_r^E}}\right]\delta_{i,s} \tag{3.30}$$

$$z_i(n+1) = z_i(n)e^{-\frac{\tau(n)}{\tau_r^E}} + \frac{\tau_r^E}{\tau_r^E - \tau_{in}} y_i(n)\left[e^{-\frac{\tau(n)}{\tau_r^E}} - e^{-\frac{\tau(n)}{\tau_{in}}}\right] \tag{3.31}$$

$$v_i(n+1) = v_i(n)e^{-\tau(n)} + a(1 - e^{-\tau(n)}) + \frac{g}{\langle k \rangle} F_i(n), \text{ if } i \neq s \tag{3.32}$$

$$v_i(n+1) = 0, \text{ if } i = s \tag{3.33}$$

$$with\ F_i(n) = \frac{\tau_{in}\left(e^{-\frac{\tau(n)}{\tau_{in}}} - e^{-\tau(n)}\right)}{\tau_{in} - 1} \cdot \sum_{j=1}^{N} \epsilon_{ij} y_j(n), \tag{3.34}$$

where s is the index of the neuron which at time t_n has emitted a spike and $\delta_{i,s}$ is the Kronecker δ function, that is $\delta_{i,s} = 1$ if $i = s$ and $\delta_{i,s} = 0$ if $i \neq j$. An analogous map can be written also in the case of an excitatory and inhibitory network (see Appendix D).

Now, to compute $\tau(n)$ or, more simply, the time t_{n+1} of the next spiking event of the network we take advantage of the so-called event-driven approach [99–103]. According to this algorithm, we first compute the spiking time of each neuron i, with $i = 1, ..., N$: we let its potential evolve in a continuous way, until it exceeds the threshold. The time step immediately

after this crossing will be its firing time $t_{i,n+1}$. From the potential equation in Eq. (3.27), this implies numerically solving the equation $v_i(n+1) = 1$, through for instance bisection methods, or computing

$$t_{i,n+1} = t_{i,n} + ln\left(\frac{a - v_i(n)}{a + (g/\langle k\rangle)\, F_i(n) - 1}\right), \quad \text{for } i = 1, ..., N. \tag{3.35}$$

Thanks to the analytical solution of the differential equations expressed in Eqs. (3.30)-3.34, the dynamics of these system can be exactly simulated and the eventual errors coming from the bisection method are negligible.

The minimum of the final array of all the firing times $\{t_{1,n+1}, t_{2,n+1}, ..., t_{N,n+1}\}$ will be the time t_{n+1} of the next event of the system. Then, we update the state of the corresponding firing neuron, resetting its potential to zero as in Eq. (3.33), we propagate the spike, properly updating every variable of all the other neurons according to Eqs. (3.30 - 3.32) and we repeat this procedure throughout the simulation time. The typical output of such a simulation consists of a vector with the times of all the firing events and a vector with the indices of the corresponding spiking neurons. With these two arrays the final raster plot, which represents the dynamical state of the network (see for example Fig. 3.2, can be built.

Note that in the map that we have introduced above, the discrete time steps are exactly all the firing events computed during the simulation and, accordingly, they are not equal, but they depends on which neuron fires first.

Now, after having defined the map and the event-driven algorithm to compute the time of the next event, two further ingredients are necessary to perform a simulation of this system: initial conditions of the system and the connectivity pattern. Connectivity pattern is fully encoded by the adjacency matrix, while initial conditions are defined by assigning to the variables u, v, y and z of each neuron random values uniformly chosen in the interval $[0, 1]$. These variables will be used as the $0-$th step values of the map, to compute the next ones.

One of the main goals presented in the Introduction is to investigate how heterogeneity can influence the synchronization properties or phase transitions in our neural networks. Since we simulate identical LIF neurons with short term synaptic plasticity, heterogeneity can appear only in the number of connections attached to each node, that is in the nodes degree: a network will be said heterogeneous if there is a large inequality among its neurons with very high and very low degree. From this point of view, it seems extremely convenient to introduce a mean field approximation of this model, which instead of requiring an adjacency matrix only needs to define a probability distribution function (p.d.f. or degree distribution) $P(k)$ for the nodes degree and in particular a distribution $P(k_{in})$ for the input degree and a distribution $P(k_{out})$ for the output degree. Such a formulation is treated in the next Section.

Finally, we underline that, since each node is characterized by its own in- and out-degree, the phrase "finite connectivity" which appears in this Section title is explained.

3.5 Heterogeneous mean field formulation with single-site degree correlation

Recent results [12, 80] obtained from numerical simulations of a purely excitatory random network of LIF neurons, coupled through the short term synaptic plasticity described by the TUM model, have shown that the neural population essentially splits into two subgroups: the locked and the unlocked neurons (see Section 1.6), as shown in Fig. 3.6. The first group follows a periodic dynamics, with constant average inter-spike interval or $\langle ISI\rangle$, equal for all neurons, while the second one is aperiodic and each neuron has its own $\langle ISI\rangle$. Referring to Fig. 3.6(a), spikes events of locked (unlocked) neurons are in the inferior (superior) part of the raster plot, while

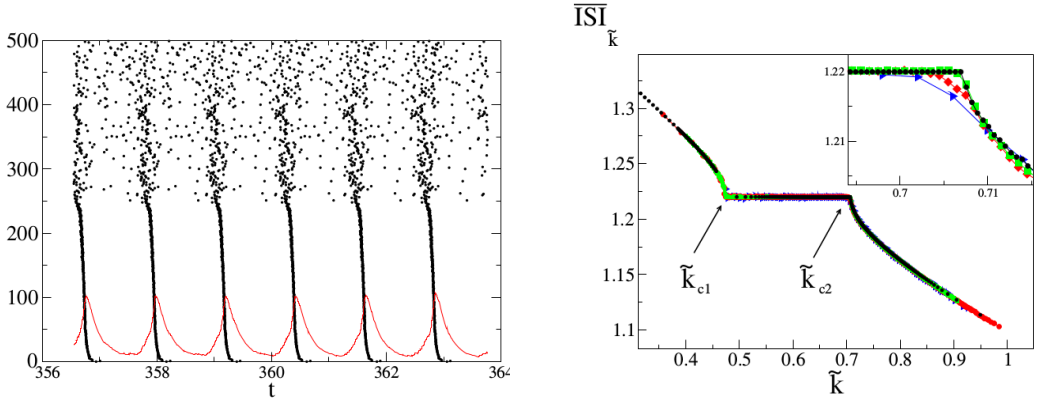

FIGURE 3.6: (a) Raster plot (black dots) and global field $Y(t)$ (red line, average value of synaptic fields defined in Eq. (3.24)) as a function of time for a network with $N = 500$ neurons and a Gaussian in-degree distribution $P(k_{in})$ ($\langle \tilde{k} \rangle = 0.7$. Neurons are ordered along the vertical axis according to their in-degree. Image from [80]. (b) Time average of the inter-spike interval $\langle ISI_{\tilde{k}} \rangle$ as a function of the degree $\tilde{k}$ of neurons for the same network simulated with different sizes N: $N = 500$ (blue triangles), $N = 5000$(red diamonds), $N = 20000$ (green squares). Neurons whit a degree $\tilde{k} \in (\notin) \left[\tilde{k}_{c1}; \tilde{k}_{c2}\right]$ are locked (unlocked). Image from [80].

their $\langle ISI_{\tilde{k}} \rangle$ correspond to the horizontal plateau in Fig. 3.6(b) and it is independent on their degree $\tilde{k}$, unlike the unlocked neurons, whose $\langle ISI \rangle$ strongly depends on the degree. This is the typical scenario of partial synchronization presented in Section 1.6 and from Fig. 3.6(b) it clearly emerges the separation between these two subpopulations is essentially driven by the neurons degree: only neurons with $\tilde{k} \in \left[\tilde{k}_{c1}; \tilde{k}_{c2}\right]$ get locked.

As a result, what most characterizes the dynamical properties of a node is not its connections pattern, but rather its degree k. In other words, only looking at its degree, we can decide to which group (locked or unlocked) a neuron belongs.

This advances the necessity of defining a particular mean field approach which could take into account such a fundamental issue, as the so-called heterogeneous mean-field or HMF theory, recently proposed in [11, 104–106], where "heterogeneous" means that it is able to somehow preserve the heterogeneity in the connectivity pattern of the original model.

Since the HMF approach was initially introduced for epidemic dynamics in social networks, here we follow the formulation presented in [80] and [12] for neural networks with short term synaptic plasticity, adding a fundamental new ingredient about the connectivity pattern chosen in our networks, which turns out to be very useful to better investigate the heterogeneity role in driving the dynamical properties.

Indeed, at the end of the previous Section we see how the degree distributions $P(k_{in})$ and $P(k_{out})$ characterize the heterogeneity in our network. However, precise measures of the connectivity patterns in brain networks of animals or humans are in many cases far from been completely known [7, 107]. Nevertheless, some general properties seems to emerge, such as small-world [108] or scale-free [109] properties (Appendix A) or the presence of functional hub [110, 111]. Among them, degree correlations among neurons, such as assortativity patterns in the synaptic connections, that is the propensity of neurons to mostly connect to cells with a similar degrees, has been shown to improve the signals transmission within the network and at the same time to prevent synchronization [30, 112]. However, a more individual kind of degrees correlation can be also taken into account, such as correlation between the input degree and the

output degree on single node. For instance, an anti-correlation, characterized by nodes with low in-degree and high out-degree and vice versa, seems to drive the stability of the network firing rate with respect to stochastic fluctuations that could be detected as a false stimulus and it turns out to be a fundamental property to detect single-cell stimulation in barrel cortex, as experimentally observed in rodents [113].

For our purposes, to maximize the effect of heterogeneity on dynamical properties of the neural network, we can take advantage of this single-site degree correlation, imposing in all our networks the in-degree $k_{in,i}$ equal to the out-degree $k_{out,i}$ for each node i. For this reason, we will refer to the input and output connectivity of node i as simply k_i, being $k_{in,i} = k_{out,i} = k_i$, and the input and output degree distributions $P(k_{in})$ and $P(k_{out})$ will be the same $P(k)$. Recently, such a strong degree correlations has been experimentally measured for instance in [114].

For now, in order to introduce the heterogeneous mean field formulation in a more general framework, let's consider $k_{in,i} \neq k_{out,i}$ and $P(k_{in}) \neq P(k_{out})$. In a purely excitatory network, the local field $Y_i(t)$ received by neuron i at time t, defined in Eq. (3.24) and Eq. (3.26), can be rewritten as

$$Y_i(t) = \frac{1}{\langle k_{in} \rangle} \sum_{j=1}^{N} \epsilon_{ij} y_j(t) = \frac{k_{in,i}}{\langle k_{in} \rangle} \frac{1}{k_{in,i}} \sum_{j=1}^{N} \epsilon_{ij} y_j(t), \tag{3.36}$$

where we write y_j instead of y_{ij} and on the right we put in evidence the input degree k_i on node i. Due to the adjacency matrix elements ϵ_{ij} in the sum, we expect to have $k_{out,i}$ non-null addends (and $N - k_{out,i}$ zero elements), so that the sum from 1 to N can be replaced by the sum from 1 to $k_{out,i}$ terms, as if instead of considering the whole network, we took only those nodes and their resources actually connected to i, such that $\epsilon_{ij} = 1$:

$$Y_i(t) = \frac{k_{in,i}}{\langle k_{in} \rangle} \frac{1}{k_{in,i}} \sum_{\substack{j=1 \\ (i,j)}}^{k_{out,i}} y_j(t), \tag{3.37}$$

where the notation (i, j) means that only the pairs where i and j are nearest neighbors are taken into account. Now, $1/k_{in,i} \sum y_j$ can be seen as an average of the resources $y_j(t)$ over all the output links of node i. In a mean field formulation, one would expect to write it as an average over all the links, that is

$$Y_i(t) \approx \frac{k_{in,i}}{\langle k_{in} \rangle} \frac{1}{2N_L} \sum_{(i,j)}^{N_L} y_{ij}(t), \tag{3.38}$$

where the sum now includes all the N_L links (i, j) of the network, with $N_L = N\langle k_{out} \rangle$, and $\langle k_{in} \rangle = \langle k \rangle / 2$ (see Appendix A). The factor 2 in front of N_L takes into account that each link is counted twice. However, since the resources y_{ij} depend only on the presynaptic neuron j, whose output degree is $k_{out,j}$, we get

$$Y_i(t) \approx \frac{k_{in,i}}{\frac{\langle k \rangle}{2}} \frac{1}{2N\langle k_{out} \rangle} \sum_{j=1}^{N} k_{out,j}\, y_j(t) = \frac{k_{in,i}}{\langle k \rangle} Y(t), \tag{3.39}$$

where in the right hand side we put into evidence the mean field $Y(t)$, which does no longer depend on the single node i, but it is a global quantity.

We clearly expect that this approximation is good for an uncorrelated random network at large k and it is exact for massive graphs in the limit of infinite connectivity, where "infinite" means that we consider the limit of large networks, $N \to \infty$, and the degrees scale with the

network size N.

Replacing Eq. (3.39) in the potential equation (first row if Eqs. (3.27)), we find

$$\dot{v_i} = a - v_i + g \, \frac{k_{in,i}}{\langle k \rangle} \, Y(t). \tag{3.40}$$

In its original form, node i is coupled to the rest of the network through the local field $Y_i(t)$ and in particular to the adjacency matrix elements ϵ_{ij}. Now, its potential equation turns out to be a single node equation coupled to the rest of the network through the mean field $Y(t)$, with a coupling term which is proportional to g and to its input degree $k_{in,i}$. As requested at the beginning of this Section, we have actually succeeded in writing a mean-field model where the single node dynamics is only driven by the degree. Accordingly, from the point of view of an effective theory, we could also read the distribution $P(k_{in})$ for the input degree k_{in} as a distribution in the coupling constants $P(gk_{in})$ (coupling distribution).

The immediate consequence of this formulation is an advantageous change of perspective in describing the network dynamics: we are now allowed to create groups of nodes with the same input degree k_{in}, called connectivity classes, and to replace the dynamics of a single node with the dynamics of a single class of nodes with in-degree k_{in}. The node resources $v_i(t), y_i(t)$ and $z_i(t)$ will be then replaced by the resources of $v_{k_{in}}(t), y_{k_{in}}(t)$ and $z_{k_{in}}(t)$ of the connectivity class with in-degree k_{in}.

In particular, in the limit of large connectivity, all the degrees can be considered as continuous variables and the discrete distributions as continuous functions, so that in Eq. (3.39) the sum can be rewritten as an integral and the mean field $Y(t)$ can be in general defined as follows:

$$Y(t) = \int \frac{P(k_{out}) \; k_{out} \; P(k_{out}|k_{in}) \; y_{k_{in}}(t)}{\langle k_{out} \rangle} \, dk_{out} \, dk_{in}, \tag{3.41}$$

where $P(k_{out}|k_{in})$ is the probability of finding an output degree k_{out}, given an input degree k_{in}.

As a consequence, the only distribution which has to be taken into account is

$$\bar{P}(k_{in}) = \int \frac{P(k_{out}) \; k_{out} \; P(k_{out}|k_{in})}{\langle k_{out} \rangle} \, dk_{out}. \tag{3.42}$$

Coming back to our specific case, since we introduce a single-site degree correlation, that is $k_{in} = k_{out} = k$ for all nodes and $P(k_{in}) = P(k_{out}) = P(k)$, $P(k_{out}|k_{in})$ is a *delta* function and Eq. (3.41) yields

$$Y(t) = \int \frac{P(k) \; k \; y_k(t)}{\langle k \rangle} \, dk, \tag{3.43}$$

where $\langle k \rangle = \int k P(k) dk$ and k now represents both the input and the output degree for the connectivity class k.

In this setup, in order to create discrete connectivity classes from a continuous distribution, we apply an importance sampling procedure on $P(k)$: on the domain $[k_{min}; k_{max}]$ of $P(k)$, we sample M discrete values k_c with $c = 1, ..., M$ ($\{k_1, k_2, ..., k_M\}$), imposing that

$$\int_{k_c}^{k_{c+1}} P(k) \, dk = \mathcal{C}, \tag{3.44}$$

where $\mathcal{C}$ is a constant, equal to $1/M$ because of the normalization condition on $P(k)$. Then, each class will be denoted by its degree k_c, which will refer to the continuous connectivity interval $[k_c; k_{c+1})$. Note that the degree k_c, left endpoint of the class interval, also called representative degree of the $c-$th class, will actually enter the potential equation in Eqs. (3.40) (factor k_i in front of the synaptic field $Y(t)$) to drive the class dynamics. The numerical results would not

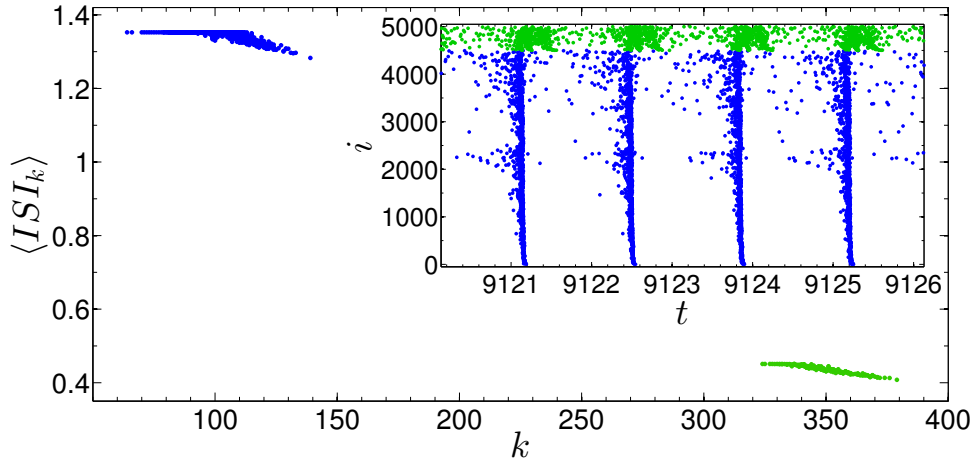

FIGURE 3.7: $\langle ISI \rangle_k$ as a function of the degree k for a network of $N = 5000$ neurons, which evolves according Eqs. (3.28). The first 4000 neurons are excitatory (blue dots), while the other 1000 are inhibitory (green dots). The degree distribution $P_E(k)$ and $P_I(k)$ of both populations is Gaussian. The excitatory average degree $\langle k_E \rangle$ is 100, the inhibitory one $\langle k_I \rangle$ is 350 and the standard deviation is the same, $\sigma_E = \sigma_I = 10$. In the inset we report a raster plot of the corresponding dynamics, where nodes are ordered along the vertical axis according to their degree k. A dot means that neuron i has fired at time t. Here and in all other plots time is dimensionless: based on the rescaling with τ_m shown in Eq. (3.4) and the values proposed in Eq. (3.29), a time unit in the abscissa axis corresponds to about 10 ms. [115]

change if one chose a different prescription, as for instance a representative degree equal to the average degree (integral mean) on the interval $k \in [k_c, k_{c+1})$, as we have briefly verified.

It is also important to emphasize that a totally equivalent formulation of this HMF approach could be obtained, if one sampled a different distribution, namely $\tilde{P}(k) = k \cdot P(k)/\langle k \rangle$, and defined the mean-field in Eq. (3.43) without the k factor in the denominator:

$$\int_{k_c}^{k_{c+1}} \tilde{P}(k)\, dk = \mathcal{C}, \tag{3.45}$$

$$Y(t) = \int \tilde{P}(k) y_k\, dk, \tag{3.46}$$

where the second row corresponds to the original formulation proposed in [80]. In that case, an exhaustive study of the validity of HMF approach in correctly reproducing the neural networks dynamics with finite connectivity can be found in [12], where this model has been tested with respect to its stability properties, its robustness to noise, its applicability also to sparse topologies and its effectiveness in solving the so-called inverse problem, that is in recovering the degree distribution $P(k)$ from the global field $Y(t)$.

Let's now consider the more general case of an excitatory and inhibitory network. Since, as for the purely excitatory case, its dynamics typically displays partially synchronous states, with locked and unlocked neurons (see Fig. 3.7, we can derive the HMF formulation of the corresponding finite connectivity equations, expressed in 3.28. Now, we have two populations of neurons, the excitatory (E) and inhibitory (I) one, whose synaptic resources evolve with a different time scale: indeed, as shown in Section 3.3, due to the facilitation mechanism the recovery time constant of an excitatory neuron is different ($\tau_r^E = 133 \cdot \tau_{in}$) from the inhibitory neuron ($\tau_r^I = 17 \cdot \tau_{in}$). The synaptic field $Y_I(t)$ reaching an inhibitory neuron is different from the field $Y_E(t)$ of an excitatory neuron and this gives rise to a different evolution of the membrane

potential. Accordingly, we need to introduce for each connectivity class two potential variables v_k^E and v_k^I for the excitatory and the inhibitory neuron class respectively and, instead of a single distribution $P(k)$, the excitatory and inhibitory degree distributions $P_E(k)$ and $P_I(k)$, which have to be correctly normalized, so that $\int (P_E(k) + P_I(k))dk = 1$. Moreover, both the mean fields $Y_E(t)$ and $Y_I(t)$ should take into account contributions of both the presynaptic excitatory and inhibitory inputs received by a class, which will be positive and negative respectively, due to the definition of the adjacency matrix given in Eqs. (3.28). Then, we get

$$\begin{aligned} Y_E(t) &= +Y_{EE}(t) - Y_{EI}(t) \\ Y_I(t) &= +Y_{IE}(t) - Y_{II}(t). \end{aligned} \tag{3.47}$$

The generic field $Y_{\dagger *}(t)$ is the contribute received by a class of type $\dagger$ from a class of type $*$, where the symbols $\dagger, *$ stand for E (excitatory) or I inhibitory, and is defined as follows:

$$Y_{\dagger,*}(t) \;=\; \int \frac{P_*(k)\, k\, y_k^{(\dagger,*)}}{\langle k \rangle}\, dk, \tag{3.48}$$

where $y_k^{(\dagger,*)}$ represents the active resources of the class with degree k and of type $*$ outgoing towards a class of type $\dagger$ and similarly it will be for the available, inactive and efficacy resources $x_k * (\dagger, *)$, $z_k * (\dagger, *)$ and $u_k * (\dagger, *)$.

Finally, the full set of Eqs. (3.28) for the evolution of an excitatory and inhibitory network can be rewritten as follows:

$$\begin{aligned} \dot{v}_k^{\dagger}(t) &= a - v_k^{\dagger}(t) + \frac{g}{\langle k \rangle} k Y_{\dagger}(t), \\ \dot{y}_k^{(\dagger,*)}(t) &= -\frac{y_k^{(\dagger,*)}(t)}{\tau_{in}} + u_k^{(\dagger,*)}(t)(1 - y_k^{(\dagger,*)}(t) - z_k^{(\dagger,*)}(t))S_k^*(t), \\ \dot{z}_k^{(\dagger,*)}(t) &= \frac{y_k^{(\dagger,*)}(t)}{\tau_{in}} - \frac{z_k^{(\dagger,*)}(t)}{\tau_r^{\dagger}}, \\ u_k^{(E,*)}(t) &= U_f, \\ \dot{u}_k^{(I,*)}(t) &= -\frac{u_k^{(I,*)}(t)}{\tau_f} + U_f(1 - u_k^{(I,*)}(t))S_k^*(t). \end{aligned} \tag{3.49}$$

where the index k now refers to the connectivity class with degree k. The values of all parameters are set as in 3.29.

As in the purely excitatory case, we can now sample the degree distribution $P_E(k)$ and $P_I(k)$ through an appropriate importance sampling and get the M discrete connectivity classes. Once defined the global field $Y_E(t)$ and $Y_I(t)$, are formally identical to the original model expressed in Eqs. (3.28), though now k is a degree index and not a single site index. We can therefore easily simulate a system of M classes, using solutions similar to those reported in Eqs. 3.30–3.34, with few slight differences when considering inhibitory contributions, and building an analogous event-driven map algorithm to find the next spiking event.

The event-driven map associated to Eqs. (3.49) is reported in Appendix D, where we also show a comparison between the results obtained with the HMF approach and the finite connectivity dynamics. As for the purely excitatory case, also in networks with excitation and inhibition it has been proved that the HMF approach reproduces better and better the neural networks behavior with finite connectivity by increasing the connectivity, as expected, and for sufficiently large degrees the two dynamics become equal. However, in excitatory and inhibitory network such a convergence is not trivial, specially if we consider the states with a dynamical balance between excitation and inhibition, as explained in Appendix D.

As a conclusion, we point out the three main advantages derived from the introduction of the HMF formulation for our neural networks dynamics:

1. The HMF approach allows us to emphasize the role of the connectivity, and in particular of the degree k, in defining the dynamical properties of the network and to preserve the heterogeneity expressed by the system topology.

2. In our network, neurons degree have to be distributed according a given function $P(k)$. In order to build a specific realization of such a random networks and write its adjacency matrix we need to consider a configuration model (see Appendix A). However, this procedure is remarkably complicated by the constraint imposed on our networks concerning the single-site degree correlation $k_{i,in} = k_{i,out} = k_i$. Indeed, during the network building algorithm we have to check that each new link from the $i-$th to the $j-$th unit is coherent with their assigned degree and in particular with $k_{i,out}$ and $k_{j,in}$. This is a rather complex and numerically heavy problem, mostly if we choose large or heavy-tailed distributions. However, in the HMF formulation we no longer need to define the adjacency matrix of the system and this issue is overcome. We will thus be able to choose any degree distribution $P(k)$ and investigate the synchronization pattern of the network as a function of its heterogeneity, that will be encoded by the distribution width, as we will see in Chapter 4.

3. From the computational point of view, numerical simulations of the HMF model come out to be very efficient and the fluctuations due to discretization of the continuous distribution $P(k)$ are very small: indeed, it has been proved (see Appendix D or [12]) that it is sufficient to sample $M \sim \mathcal{O}(10^2)$ connectivity classes to effectively reproduce the finite connectivity dynamics, which otherwise could require to manage networks with thousands of nodes (with all their variables and the corresponding adjacency matrices).

In the next Chapter we will apply the HMF model to purely excitatory ensembles, to study how the heterogeneity of the network, represented by its degree distribution $P(k)$, influence its synchronization properties. Results about excitatory and inhibitory networks with the HMF formulation are instead reported in Chapter 5.

Chapter 4

The role of heterogeneity in driving synchronization

In the previous Chapter we have described in detail our model of neural network, which is composed of leaky integrate-and-fine excitatory and inhibitory neurons with short term synaptic plasticity, introduced through the Tsodyks-Uziel-Markram equations. Then, we have adopted a mean field formulation of this model, called the heterogeneous mean field, which is rather useful since it preserves the heterogeneity of the system and puts in evidence the role of the connectivity in driving the neurons dynamics. Finally, we have shortly presented the numerical algorithm, which we use to simulate our networks.

Now, in this Chapter we discuss the synchronization dynamics of purely excitatory networks with different degree distributions, in order to investigate which parameters are the most relevant in driving the phase transitions from partially synchronous to asynchronous regimes, starting from some known results in literature, as the "paradox of heterogeneity". First, we consider the simple case of a Gaussian distribution, then we introduce a scale-free topology and we discuss about the role of its initial cutoff. Finally, we analyze a distribution which is somehow able to interpolate these two cases.

4.1 The paradox of heterogeneity on neural networks

The role of heterogeneity in driving synchronization properties of a system of N coupled oscillators has been intensively investigated (see for instance [11, 112, 116]), particularly since when A. Motter and co-workers stated the so-called "paradox of heterogeneity" [13]. Considering an unweighted network of linearly coupled identical oscillators, through a master stability function approach (see Appendix B) they found that the system synchronizability, that is the propensity if a system to become synchronous, decreases when the heterogeneity of the degree distribution of their elements increases.

In general, starting from a regular ring of N nodes, each connected to $2m$ nearest neighbors, heterogeneity is tuned by the number M of random links which are added to go from a regular graph to a small-world topology (see Appendix A). For small values of M, most of the nodes preserve the regular connectivity pattern of the starting graph, so that the degree distribution is almost uniform, while for large M many random links are added and more heterogeneous topologies arise. In these small-world topologies, random links act as efficient shortcuts, directly linking nodes that otherwise would be away from each other and reducing the diameter of the network (Appendix A). This should enhances communication among single elements, promoting the onset of complete synchronization states, as shown in [117], where small-world networks have been proved to synchronize more efficiently than random graphs.

However, this is not always true, since enhancing the degree heterogeneity and consequently decreasing the diameter of the network corresponds to create hub nodes, i.e. nodes

whose degree is much larger than the average connectivity of the whole system. The overload of these hubs does not help the system to get synchronous. Here is the "paradox of heterogeneity": although they have smaller diameters, heterogeneous networks are less easily synchronized than homogeneous ones, because the large amounts of incoherent inputs that a hub typically receives from other oscillators tend to balance each other, hindering its synchronization. Therefore, also the onset of synchronization of the whole network is more difficult, as reported for instance in [118], where heterogeneity is controlled by the number of hubs or "centers" present in the system.

Concerning synchronization in neural networks, a simple way to introduce heterogeneity is considering an all-to-all network of N coupled excitatory and inhibitory neurons, with a fixed probability distribution for their natural firing frequency [119]. In this case, when the heterogeneity increases, it has been analytically proved that phase-locked states lose stability and disappear. Otherwise, the heterogeneity in systems of firing pulse-coupled neurons can be also defined by the network topology, as in [120], where the synchronizability seems to be mainly driven by the degree and in particular by the input degree k of neurons, showing that neurons with similar k can more easily synchronize than others.

The role of connectivity has been particularly investigated in excitatory random networks of pulse-coupled neurons [121, 122], where neurons are described by the same LIF equation that we have chosen in our work (see Section 3.2), in presence of sparse connectivity [123] or in presence of quenched or annealed disorder in the connections pattern. More precisely, the system displays a transition from an asynchronous phase to a partially synchronous regime as a function of the average degree $\langle k \rangle$ [122]. Similar results can be found in a different model of uniform (random) and small-world neural networks, but not in scale-free topologies, as shown in [124].

In excitatory diluted random networks, with LIF oscillators as single neurons, coupled through the same dynamics of short term synaptic plasticity introduced in our work, synchronization transitions have been analyzed as a function of the synaptic time constant τ_{in}, again in presence of quenched disorder [79]. Finally, in [80] the synchronization level in similar random networks is computed through the fraction of locked neurons (see Section 2.4) as a function of the standard deviation of the input degree distribution $P(k_{in})$ for different distributions. In that paper, as a conclusion, it is simply said that "*the fraction of locked neurons increases as $P(k)$ becomes sharper and sharper, while synchronization is eventually lost for broader distributions*" [80].

Broad degree distributions are also taken into account in [125] for purely inhibitory and excitatory/inhibitory networks of integrate-and-fire neurons, though without synaptic plasticity, and seem to produce the same global effect: an increase of the width in the distribution and, in particular, in the input degree distribution reduces the coherent oscillations of the system.

Now, how to better characterize such a relation between synchronization and broad distributions or heterogeneity? Can we state for our specific neural network models a general synchronization criterion, which somehow deals with the above mentioned "paradox of heterogeneity", whose validity has been discussed in generic systems of coupled oscillators? In this framework, we can now present our results, concerning a systematic study of synchronization properties of purely excitatory networks with LIF neurons and short term synaptic plasticity as a function of the degree heterogeneity and the synaptic coupling strength.

4.2 Simple case: synchronization transitions with Gaussian degree distribution

Let's consider the neuronal network in the heterogeneous mean field formulation, described in the previous Chapter and in particular by Eqs. (3.49), where we consider the only excitatory population: this implies that $P_I(k) = 0,\ \forall k$, so that the only degree distribution is excitatory

$P(k) = P_E(k)$, as the synaptic field $Y(t) = Y_E(t)$, computed according to Eqs. (3.43). Since the network does not require any facilitation mechanism, $u_k^{(I,*)}(t)$ are now null and the last row in Eqs. (3.49) can be neglected. For all the other variables, only the excitatory contribution is taken into account. In this setup, the effectiveness of the HMF approach in correctly capturing the dynamics of a finite connectivity network, described in Eqs. (3.27), has been largely proved in [12]. Moreover, since in Section 3.5 we have properly defined a mean field $Y(t)$ which takes into account the correlation between the input and the output degree for each node, or $k_{i,in} = k_{i,out} = k_i$, we are allowed to safely apply the HMF approximation to simulate our networks.

What we now need is simply choosing an appropriate probability distribution function $P(k)$ for the nodes (input and output) degree. As emerged in Section 3.4, the connectivity properties of our random networks are described by their degree distribution, especially when we switch to the HMF formulation of the model. Then, the network heterogeneity will be naturally defined by the width of this distribution: broad distributions will correspond to more heterogeneous topologies, where neurons with very low degrees are mixed with neurons with very high degrees, or hubs, while narrow distributions will be related to more homogeneous networks.

From known results in literature (see Section 4.1), we expect to observe synchronization phase transitions as a function of this heterogeneity in the connectivity pattern, or more precisely transitions from a synchronous to an asynchronous dynamical state, displayed by the network in the steady regime, when we enhance the width of the degree distribution $P(k)$ or equivalently of the coupling distribution, if we consider the point of view of the effective theory, introduced in Section 3.5.

As a starting point, we first consider a Gaussian p.d.f. $P(k)$, with

$$P(k) = \frac{1}{\sqrt{2\pi}\sigma} e^{-\frac{(k-\langle k\rangle)^2}{2\sigma^2}}, \tag{4.1}$$

where $\langle k\rangle$ is the average degree and σ is the standard deviation. This is one of the easiest distribution to manage, as it is convergent for $k \to 0$ and $k \to \infty$, its moments are always well-defined and its width is directly tuned by the standard deviation. Accordingly, keeping in this case fixed the average degree $\langle k\rangle$ and varying the standard deviation, the ratio $\sigma/\langle k\rangle$ will be the heterogeneity parameter of our networks.

As shown in Section 3.5, through the importance sampling procedure, we sample this Gaussian distribution to create M discrete connectivity classes $\{k_1, k_2, ..., k_M\}$. Here, the typical number of degree classes that we simulate is $M = 500$, unless otherwise specified, since it appears to be a good compromise between an appropriate discretization of the $P(k)$ and a set of equations, which is not too heavy to be numerically integrated. Moreover, in [12] it has been shown that the simulation of a HMF dynamics with discrete classes converge fast enough, that is as $1/\sqrt{M}$, to the HMF model with $M \to \infty$ and a number of classes equal to $M \sim \mathcal{O}(10^2)$ is already able to correctly reproduce the finite connectivity dynamics.

Now, if we consider an average degree $\langle k\rangle = 10$ (fixed) and a standard deviation $\sigma = 1$, so that the ratio $\sigma/\langle k\rangle$ is equal to 0.1, and we vary the coupling constant g of the LIF equation in Eqs. (3.49), we can observe a phase transition from partially synchronous states for small values of g to asynchronous dynamics as g increases.

Raster plots corresponding to the first regime display the typical pattern of partial synchronization: classes with low degrees, as for instance those with an index $i \lesssim 350$ in in Fig. 4.1(a), are locked, while classes with high degree ($i \gtrsim 350$) are unlocked. The periodic dynamics of the first group corresponds to a constant value of the average inter-spike interval $\langle ISI_k\rangle$, equal for all locked neurons, which does not depend on their degree. This gives rise to the typical horizontal plateau, which referring to Fig. 4.1(a) emerges for $k_{min} \leq k \leq 10.5$, being k_{min} the lowest

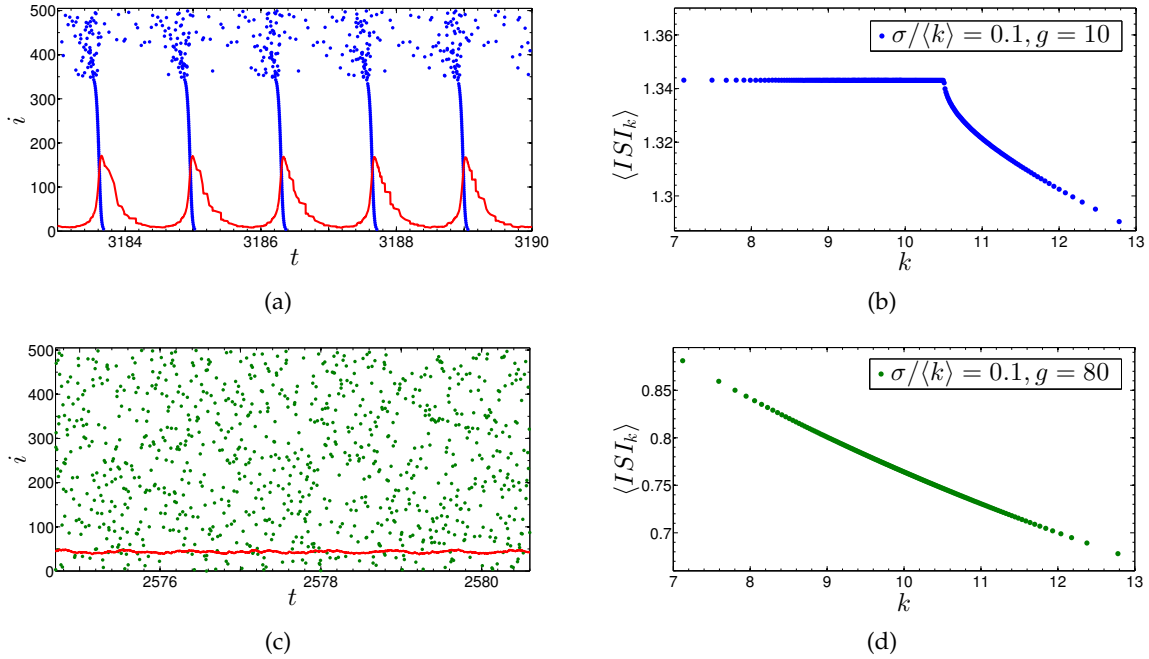

FIGURE 4.1: (a) Raster plot of an excitatory network (blue dots) and excitatory synaptic field $Y_E(t)$ (red line) as a function of time t. We have set $M = 500$ connectivity classes and coupling constant $g = 10$. The degree distribution $P(k)$ is a Gaussian with $\langle k\rangle = 10$ and $\sigma = 1$. In this setup, the dynamics is partially synchronous, with locked and unlocked neurons. Nodes are ordered along the vertical axis according to their degree k and i is the class index. Here and in the next raster plot, in order to make it visible on the raster plot, we have rescaled the field $Y_E(t)$ of a factor equal to 6000. (b) $\langle ISI_k\rangle$ as a function of the degree k for the same network. The left horizontal plateau represents to the locked neurons. (c) Raster plot (green dots) and excitatory synaptic field $Y_E(t)$ (red line) as a function of time t, for a network with the same parameters of the previous one, but with $g = 80$. Now, the dynamics is completely asynchronous and all neurons are unlocked. (d) Corresponding plot of $\langle ISI_k\rangle$ as a function of the degree k.

degree in the network, representative of the first class. Otherwise, in the unlocked group each classes evolves in an incoherent way with respect all the others and its $\langle ISI_k\rangle$ depends on k.

In the asynchronous regime, we can no longer point out any locked class from the raster plot (see for instance Fig. 4.1(c)) or any plateau in the $\langle ISI_k\rangle$ vs k plot (see Fig. 4.1(d)) and the dynamics is everywhere aperiodic or unlocked.

For a further characterization of the dynamical state, we have superposed to the raster plots also the mean field $Y_E(t)$, computed according to Eq. (3.43), after a rescaling with an appropriate factor to make it well visible on the raster plot scale. In the partially or totally synchronous regime, this field is periodic with the same periodicity of the locked group and its peaks correspond to the series of firing events of the synchronous classes.

Note that, strictly speaking, the periodic behavior of these neurons is not a real synchronization (see Section 1.3 and [15] for instance): although they are characterized by the same period (or frequency), they have different phases because, within a single locked series, spikes do not occur exactly at the same same, but with constant phase shifts, each class with respect to the others. Accordingly, we should more correctly call such a dynamics a 1:1 phase locking (see Fig. 1.3). Moreover, in a recent work [126] it has been shown that this partial synchronization corresponds to a quasisynchronous regime, where, in addition to a locked cluster of nodes, the unlocked neurons display a quasiperiodicity, that is a not trivial periodicity on longer or

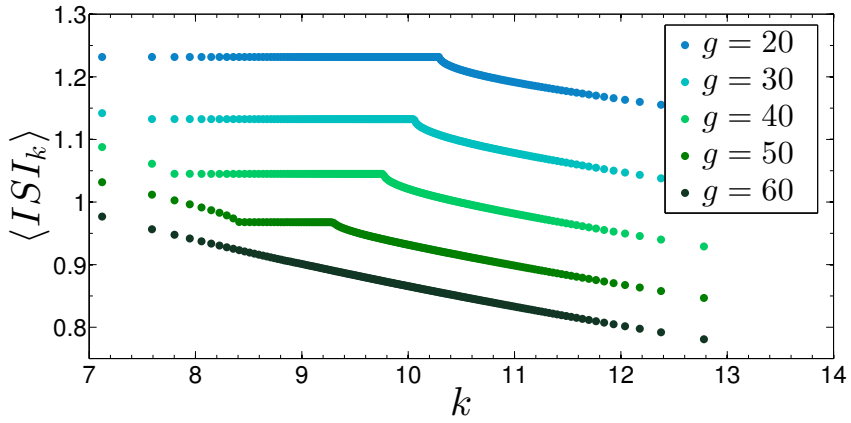

FIGURE 4.2: $\langle ISI_k \rangle$ as a function of the degree k for a network with a Gaussian degree distribution $P(k)$, where $\langle k \rangle = 10$ and $\sigma = 1$, and different coupling constants, as indicated in the legend.

shorter time scales than the locked dynamics. Every time that in this work we consider partial synchronization, we actually refer to this quasisynchronous regime.

In Fig. 4.2 we analyze the dynamics as a function of the increasing coupling g: for larger g the network gets less synchronous and the locked plateau shrinks, until neurons with too low degree exit from the locked cluster (for $g = 50$) and become asynchronous and only a small group of classes remain still periodic. As a result, a further increase of g ($g \sim 60$) make the system totally asynchronous.

To better characterize such a synchronous-asynchronous phase transition we take advantage as order parameter the Kuramoto parameter R, defined in Eq. (2.2), as a function of the coupling g. More precisely, all the R are temporal average values of the Kuramoto parameter, or $R = \langle R(t) \rangle$, computed over a sufficiently large time interval, let's say over a sufficiently large number of integration steps of the event-driven map, after discarding the transient period, that is the first iterations of the map at the beginning of the simulation.

This initial transient dynamics is necessary for the network to thermalize towards the stationary dynamical regime, starting from the initial conditions (randomly chosen with uniform probability on the interval $[0, 1]$) imposed to the system. The transient clearly depends on the coupling constant, since in a weakly coupled system (small g) single neurons take longer to interact and influence each other than in a strongly coupled system. Consequently, also the average value R should be properly defined, considering that with slower and slower dynamics (smaller and smaller coupling g) $R(t)$ has to be measured over larger and larger intervals. For this reason, every time we compute the Kuramoto parameter R we average over about N^3/g iterations of the map.

In Fig. 4.3(a), we plot R as a function of g for different values of the ratio $\sigma/\langle k \rangle$. As expected, what first emerges is that an increase in the coupling among neurons makes the system more heterogeneous and therefore synchronization lowers. Similarly, a decrease of g enhances the synchronous level. Indeed, in less coupled networks each neuron tends more to evolve as a single unit, according to its own natural frequency, equal for each unit to $f_{locked} = 1/\langle ISI_{locked} \rangle$, since all our LIF neurons are identical (Section 3.2).

However, in the limit of small couplings the transient time diverges and we do not observe a total synchronization, since R does not tend to 1, as it clearly emerges in Fig. 4.3(a). In particular, $g \to 0$ is a singular limit. Indeed, setting $g = 0$, we expect an asynchronous system: all the oscillators are uncoupled and their phases remain uncorrelated, since they do not interact with each other. Otherwise, computing the average Kuramoto parameter R, waiting for longer and longer transient times as g decreases, and considering $g \to 0$ we would obtain maximum

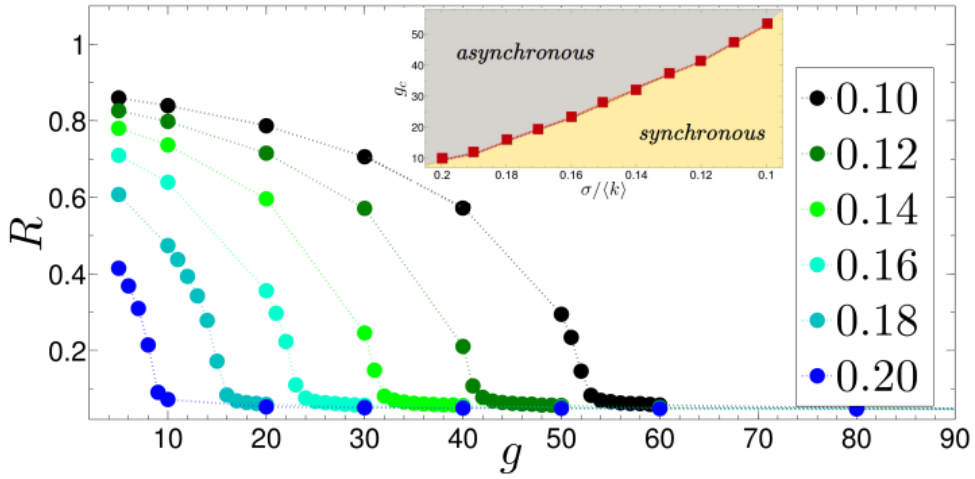

(a)

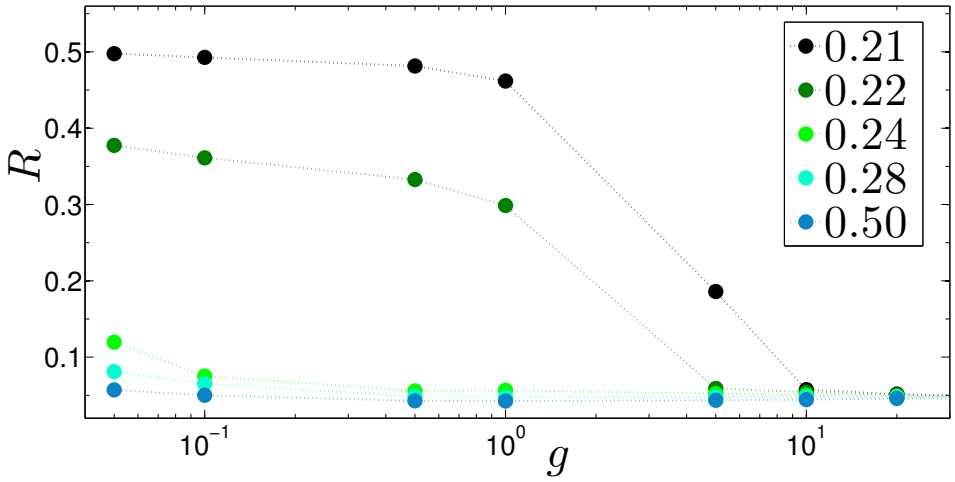

(b)

FIGURE 4.3: Synchronization phase transition for a Gaussian degree distribution $P(k)$ as a function of the heterogeneity parameter $\sigma/\langle k\rangle$, shown in the legend. For each $\sigma/\langle k\rangle$, we plot the Kuramoto parameter R a function of the coupling g. For simplicity, due to the different scales used for the coupling g, we split the transitions into two panels, based on the value of $\sigma/\langle k\rangle$: $0.1 \leq \sigma/\langle k\rangle \leq 0.2$ in panel (a) and $\sigma/\langle k\rangle > 0.2$ in panel (b). Lines have been drawn to guide the eyes. In the inset of the top panel we schematically show the final phase diagram of the critical value g_c of the coupling as a function of $\sigma/\langle k\rangle$.

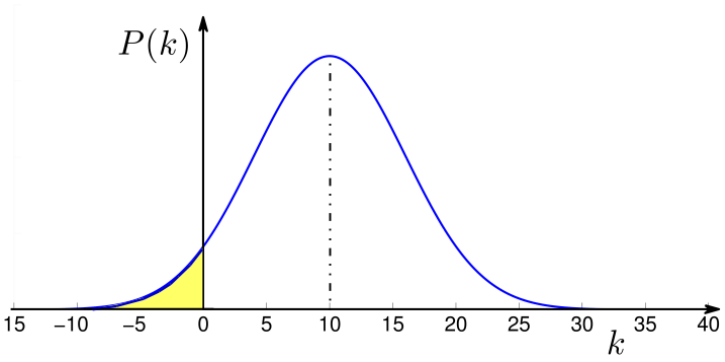

FIGURE 4.4: Example of a broad Gaussian distribution with negative degrees. Here in particular the ratio $\sigma/\langle k\rangle$ is equal to 0.6. When we need to simulate such distributions, the yellow area is cut off in order to consider only the positive degrees and the function is correctly renormalized.

synchronization.

As for each level of heterogeneity, that is for each value of $\sigma/\langle k\rangle$, an increase of g reduces the synchronization of the network, we can compute, for every transition, the critical value g_c of the coupling for which the system goes from a partially synchronous to an asynchronous regime. In the inset of Fig. 4.3(a), the plot we have obtained of g_c as a function of $\sigma/\langle k\rangle$ shows that an increase of the heterogeneity makes the network less synchronizable, since $g_c \to 0$ as $\sigma/\langle k\rangle$ grows. Thus, from these first insights it turns out that the "paradox of heterogeneity" seems to be confirmed in a totally different context from what is presented in [13].

This situation is directly more evident if we further enlarge the Gaussian distribution for $\sigma/\langle k\rangle > 0.2$. As shown in Fig. 4.3(b), beyond a certain width the critical coupling g_c goes to 0 and we do not observe any synchronous-asynchronous phase transitions, even for very small values of the coupling.

However, in this last case of broad Gaussian distributions a new issue arises: indeed, for large values of σ, due to their width, the left tail of the Gaussians broaden towards negative degrees, as schematically shown in Fig. 4.4. Adding negative degrees to the network and consequently negative couplings in the potential dynamics in Eqs. (3.49) would be equivalent to consider negative synaptic fields and to include an inhibitory mechanism in the network. As systems with an inhibitory component correspond to a totally new scenario and are discussed in the next Chapter, here we need to keep only the positive degrees and therefore Gaussian distributions with an initial cutoff if their width requires it. Synchronization measures reported in Fig. 4.3(b) actually refer to networks with these kind of modified distributions.

Now, looking at this figure, we are no longer allowed to state that the heterogeneity parameter $\sigma/\langle k\rangle$ is the only factor to drive the synchronization properties of the network. Indeed, increasing the Gaussian width makes the system more uncoupled, since the number of neurons with low degree enhances and new classes with $k \sim 0$ are included, as if the Gaussian peak shifted towards 0. Both these two features may control the onset of synchronous regimes: from one side the degree heterogeneity, which grows with the distribution width and puts together nodes with very high and very low degrees, and on the other side the presence of a larger and larger population with null connectivity, or with $k \to 0$. In particular, these new nodes with very low connectivity tend to accumulate at 0.

In the next Section we choose a different degree distribution in order to try to separate these two factors.

4.3 Synchronization transitions with power law degree distributions

In the previous Section we have discussed the synchronization transitions in network with Gaussian degree distributions, showing a not so trivial relation between heterogeneity and excitatory system synchronizability, due to the fact that we can not continue to increase the peak width, i.e. its standard deviation, without weakening the coupling pattern of the neurons and adding classes with $k \to 0$. This component with null connectivity can influence the onset of synchronization as much as the heterogeneity parameter. Rather, we need a degree distribution which can be enlarged how much we want towards high connectivities, letting us control the presence hubs, but at the same time does not accumulate in $k = 0$.

One of the simplest candidates with these features is the power law distribution $P(k) = \mathbb{N}k^{-\alpha}$, with normalization constant $\mathbb{N}$ and $\alpha > 0$ and an initial cutoff, such that $k \in [k_{min}, \infty)$ with $k_{min} > 0$ and the divergence in $k = 0$ is removed. In all the following results we set $k_{min} = 10$. The main features (mean value and variance) of this power law distribution can be easily computed from simple analytical integrals. Note that, in order to not diverge and to remain well-defined, the variance requires that $\alpha > 3$ and the average degree, which is a necessary parameter for the dynamics since it appears in the potential equation in Eqs. (3.49), $\alpha > 2$.

In networks with such distributions, typically called scale-free (SF) networks (see Appendix A), the width σ or the heterogeneity parameter $\sigma/\langle k \rangle$ is encoded only by the exponent α and it is independent on the cutoff k_{min}. First, decreasing α makes the network more heterogeneous; then, classes with very low connectivity ($k \to k_{min}$) are anyway included and are safely fixed: when the degree distribution gets larger and the hubs grow, the "peak" does no longer shift towards $k \to 0$, as for the Gaussian case.

Synchronization properties of scale-free networks has been intensively investigated, also due to the fact that power law distributions are highly widespread in different fields: networks with scale-free topology emerge in biology as well as in technology, in engineering and in social contexts, as shown in Appendix A, where the most measured or computed exponents α are less than 3. Topologies characterized by power law degree distributions also appear in brain networks, as for instance at the level of functional connectivity (Section 3.1), where they have been detected through fMRI observations (Section 2.2) [83, 109] and the computed exponent is close to 2 with an average number of connections per neuron equal to 4.

A wide range of results are known in literature about synchronization in networks with power law degree distributions. Among them, a recent work by D. S. Lee [127] show a complete phase diagram for a SF network of oscillators, as a function of their coupling and the exponent of the distribution: in the thermodynamic limit, for $2 < \alpha < 3$ the system is always synchronized ($R > 0$) for any value of the coupling, while for $\alpha > 3$ a transition from an asynchronous to a synchronous state appears as the coupling increases, due to the formation of the giant cluster of synchronized oscillators. An analogous result comes from [128]. What clearly emerges is that a radical change in the system behavior occurs at $\alpha > 3$, that is when the degree fluctuations, measured by the distribution variance, begin to be convergent.

In particular, for $\alpha = 3$ in finite size system there exists a small critical value for the coupling for which a small fraction of elements becomes locked and typical partially synchronous states, as those we have observed in our networks, appear, until a total synchronization is reached [129]. Similar to this, many other works (as for instance [130, 131]) discuss the synchronization properties with $\alpha = 3$, since this is the typical value of the exponent obtained from the Barabási-Albert (BA) model of SF networks (see Appendix A), or with $\alpha \approx 2$, when some extensions of the Barabási-Albert (BA) model are taken into account, as for [132].

Again, in finite size networks of oscillators an improvement in the synchronizability of the system, which produces synchronization transitions also for $2 < \alpha < 3$, can be in general

obtained if a positive correlation is set between the oscillators natural frequency and the corresponding node degree, as shown in [133–135]. A further synchronization transition has been for the first time observed also in specific neural network based on the McCulloch-Pits model of synaptic interaction and power law degree distribution with $1.5 < \alpha \leq 2$ where the average connectivity diverges [136].

What emerges from this brief list of know results it that, regardless of the specific model which is take into account, synchronization and other dynamics properties of a network are strongly influenced by the exponent of the connectivity distribution and a net change in the behavior of the system occurs when the exponent α shifts towards values for which the first or the second moment of the distribution diverge or are not well-defined. In this framework, especially for what concerns synchronization, we now investigate the synchronization transitions performed by our neural networks with power law distributions $P(k)$ from the point of view of the topology heterogeneity, tuned by α, and we see that α is no longer the only relevant parameter.

Let's first consider a given value of α, for instance $\alpha = 4.3$, and $M = 500$ connectivity classes and directly analyze the transition, plotting in Fig. 4.5(a) the average Kuramoto parameter R as a function of the coupling g (blue dots). As for the Gaussian case, small values of g correspond to a partially synchronous regime, with locked neurons at low connectivity and unlocked neurons at high connectivity, while as g increases the network becomes less and less synchronous, until it falls in a totally asynchronous regime for a given $g > g_c$. Computing the critical value g_c of the coupling is not so trivial, but we now need to apply a finite-size scaling: indeed, finite-size effects coming from simulating an HMF model with discrete classes strongly influence the fluctuations in the aperiodic regimes. This is why in the asynchronous states the Kuramoto parameter is not perfectly null and it is more difficult to identify the exact transition point than in the Gaussian case, where the finite-size fluctuations seem to be not so crucial. However, if we simulate the same HMF network with a better discretization or with sampling on the degree distribution with more connectivity classes, R decreases towards zero. Only considering the full HMF model, which would correspond to an infinite discretization $M \to \infty$, we would expect to obtain a null Kuramoto parameter for the asynchronous phase.

Hence, taking advantage of a finite-size scaling analysis [137], we consider 4 different discretizations of the same model, namely $M = 250, 500, 1000,$ and 2000, and for each one we plot its synchronization transition as a function of g (see Fig. 4.5(a)).

As we expected, the comparison of data concerning different M shows that in the periodic regime the level of synchronization of the network does not depend on M and the relative values of R well overlap, while in the aperiodic regime R gets closer to zero as M increases. In that case, the scaling of R goes as $1/\sqrt{M}$ [12, 129, 137], as shown in Fig. 4.5(b), where for each M we plot the rescaled Kuramoto parameter $R_{res,M} = R_M/\sqrt{M}$ (R_M denotes the Kuramoto parameter R of the network with M connectivity classes). Since they now show the correct scaling, all data of the asynchronous regime perfectly overlap.

Accordingly, we can define the critical coupling value g_c as the point where this scaling law begins to fail and the transition curves split. In Fig. 4.5(b) this corresponds to $g_c = 150$.

We can now repeat the same analysis for different values of the exponent and in particular for $3.8 < \alpha < 4.3$, observing that the synchronization scenario, with partial synchronization at small g and asynchronous states at large g, does not substantially change. However, for $3.5 < \alpha \leq 3.8$ a double transition emerges. In the small coupling region the network is asynchronous. Then, as g increases, we find a first critical point g_c^{inf} and a partial synchronization regime appears, until a second phase transition at $g_c^{sup} > g_c^{inf}$ is reached and the network becomes definitively asynchronous. Considering for example $\alpha = 3.6$, whose plots are reported in Fig. 4.5(c) and Fig. 4.5(d), especially from the rescaled plot we see that $g_c^{inf} \simeq 30$ and $g_c^{sup} \simeq 170$ and for $30 < g < 170$ we get an intermediate partially synchronized region, which tends to

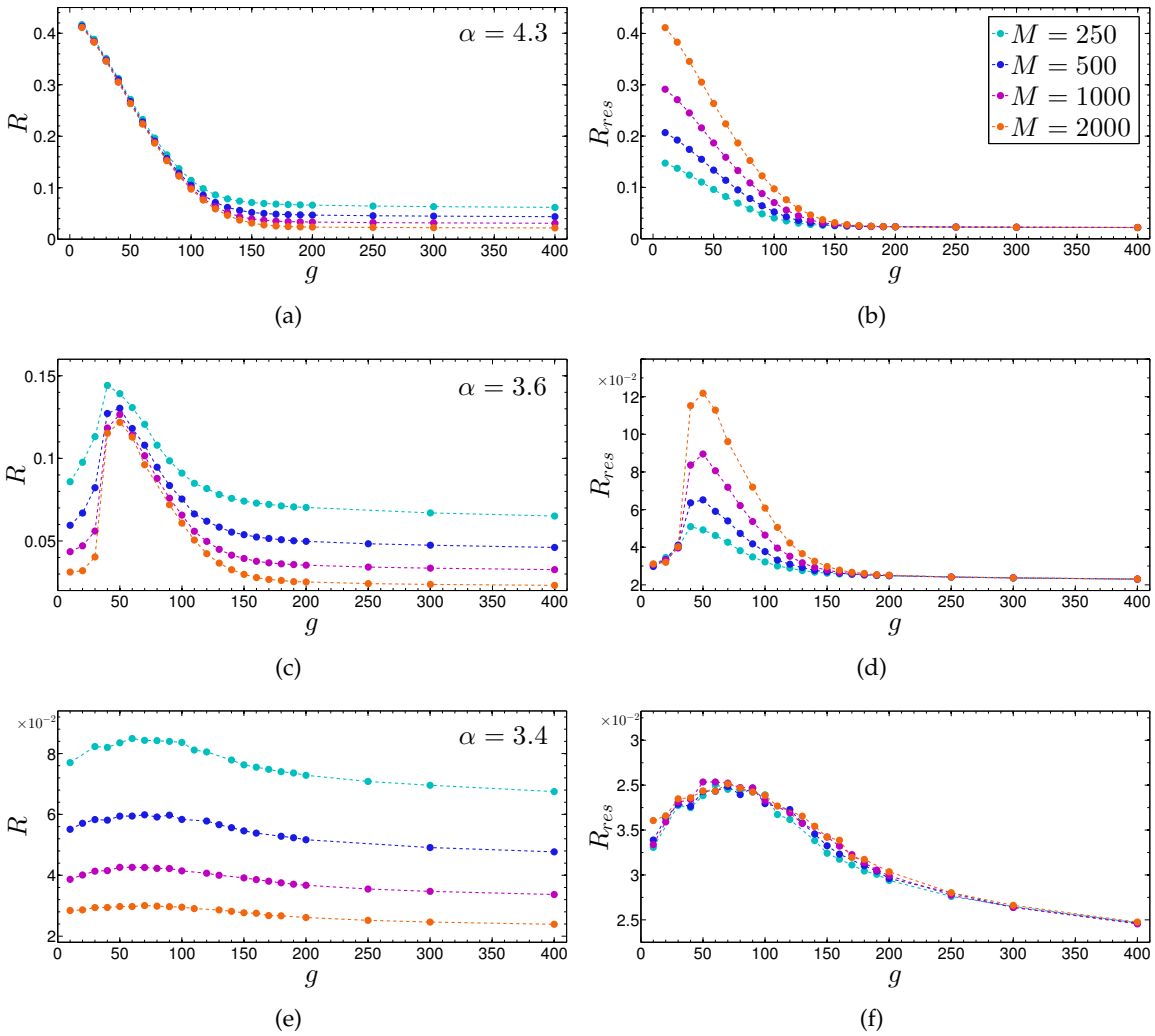

FIGURE 4.5: Synchronization phase transitions for power law distributions with different exponent α: in the left column, $\alpha = 4.3$ in panel (a), $\alpha = 3.6$ in panel (c) and $\alpha = 3.4$ in panel (e). For each exponent, we plot the Kuramoto parameter R as a function of the coupling g, considering (in different colors) 4 discretizations of the distribution $P(k)$, namely $M = 250, 500, 1000$ and 2000 connectivity classes, as shown in the legend of panel (b), which applies to every plot of this figure. In the right panels we simply rescale R to take into account the finite-size effects coming from simulating an HMF model with discrete classes. In particular, keeping data related to $M = 2000$ (the finest implemented discretization) as a reference, $R_{res,1000} = R_{1000}/\sqrt{2}$, $R_{res,500} = R_{500}/2$ and $R_{res,250} = R_{250}/2\sqrt{2}$. Note that the computing time for integrating and evolving the map considerably increases when we simulate a larger numbers of classes.

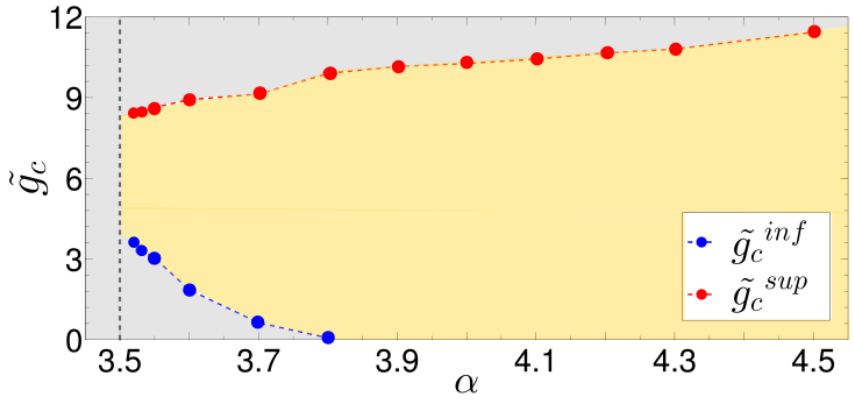

FIGURE 4.6: Synchronization phase diagram for power law distributions: we plot the critical couplings $\tilde{g_c}^{sup}$ (red dots) and $\tilde{g_c}^{inf}$ (blue dots) as a function of the exponent α. Each critical value $\tilde{g_c}$ has been computed looking at the rescaled plots of the single transitions, as those reported in the previous figures. The yellow area corresponds to the synchronous regime, while the grey-shaded area to the asynchronous regime. Note that, when we are very close to $\alpha = 3.5$, fluctuations diverge and recognizing the synchronization transition becomes rather difficult, even with very large number of classes.

shrink as α decreases, as it will be shown in the final phase diagram. We can also state that in these intermediate values of α the limit of $g \to 0$ is no longer a singular limit.

Finally, when for $\alpha < 3.5$ no synchronization transition has been detected, for neither small nor intermediate values of the coupling.

In order to compare the results of the critical coupling values g_c for all the different exponents α we have considered, we need to properly rescale also the coupling parameter, since in the potential equation in Eq. (3.49) the coupling of the $k-$th class to the synaptic field $Y(t)$ is proportional to $g/\langle k \rangle$. Therefore, we define the rescaled coupling constant $\tilde{g_c} = g_c/\langle k \rangle$.

The final phase diagram of the rescaled critical couplings $\tilde{g_c}^{sup}$ and $\tilde{g_c}^{inf}$ as a function of the heterogeneity of the network, or of the exponent α itself, is reported in Fig. 4.6 (for coherence, for $\alpha > 3.8$ the only critical point which is present is denoted as $\tilde{g_c}^{sup}$). Looking at that plot, it turns out that also with scale-free topologies the "paradox of heterogeneity" seems to remain valid: as α decreases, the hubs increase their degree, the network becomes more and more heterogeneous and therefore less and less synchronized. Indeed, the critical coupling $\tilde{g_c}^{sup}$ for which the network becomes asynchronous lowers and at the same time for $3.5 < \alpha \leq 3.8$ a second transition appears at increasing values of $\tilde{g_c}^{inf}$, so that the central synchronized region shrinks.

Since the qualitative behaviour of the system seems to be mainly driven by the exponent α, in the next Section we discuss the robustness of these results with respect to the initial cutoff imposed to the distribution, considering some possible variations of these power law functions and showing the fundamental role played by the cutoff in driving the system synchronization.

4.4 Modified power law degree distributions

One of the open questions of the previous Section is how the initial cutoff of the power law degree distribution, necessary to remove the connectivity divergence in $k = 0$, can influence synchronization transitions on the network. In the first case we have chosen a sharp cutoff, setting a minimum degree $k_{min} = 10$ and a $P(k) \sim k^{-\alpha}$ with $k \in [k_{min}, \infty)$. Some preliminary tests show that the final phase diagram reported in Fig. 4.6 does not substantially depend on

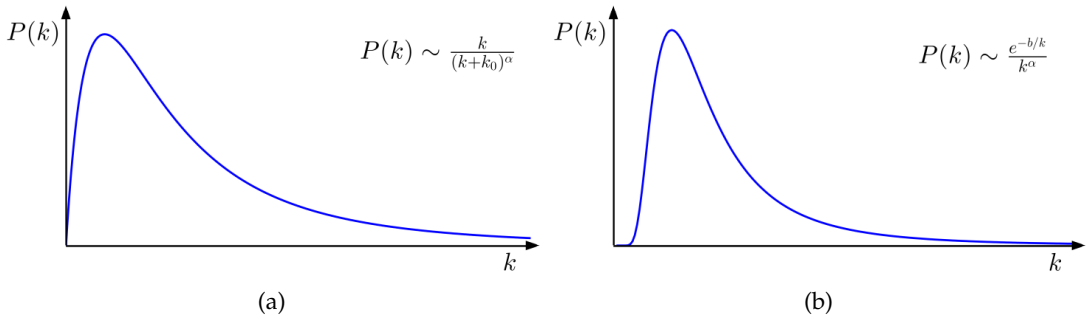

FIGURE 4.7: Two examples of power law distributions with a different initial cutoff: linear in panel (a) and exponential in panel (b). The analytical expressions of these functions are reported in the corresponding panel.

the value of $k_{min} > 0$ and comparable results could be obtained if we used $k_{min} = 5$ or other values. Indeed, in this case changing k_{min} simply corresponds to a rescaling of the coupling g.

Another standard cutoff, which is usually applied to power law distributions, is a shift for the whole distribution of a quantity $k_0 > 0$, which yields

$$P(k) \sim (k + k_0)^{-\alpha}, \text{ with } k \in [0, \infty). \tag{4.2}$$

As we have numerically verified, with such distributions any synchronization transition disappears and networks are always asynchronous, for any value of the coupling g. For what has emerged in the Gaussian case, this could be a consequence of the presence of a peak at $k = 0$, as all these distributions display.

In order to remove this peak from $k = 0$, smoother prescriptions can be considered as initial cutoff of the power law $P(k) \sim k^{-\alpha}$. Therefore, we have considered different distributions, such as $P(k) \sim k/(k + k_0)^{\alpha}$ with $k \in [0, \infty)$, shown in Fig. 4.7(a). Surprisingly, also in this case we have observed that networks never synchronize, even for arbitrarily "narrow" distributions (very large α).

To understand these results, we have tried to compare the peak of these modified power laws with a Gaussian peak, through a Taylor expansion about their maximum. For this purpose, we rewrite the new distribution $P(k)$ in an equivalent way, as follows:

$$P(k) = \mathbb{N}\frac{k}{(k + k_0)^{\alpha}} = \mathbb{N}e^{\ln \frac{k}{(k+k_0)^{\alpha}}} = \mathbb{N}e^{\ln k - \alpha \ln(k+k_0)} = \mathbb{N}e^{f(k)}, \tag{4.3}$$

where $\mathbb{N}$ is the normalization constant.

Writing the generic Taylor series for $f(k)$ about its maximum $k = k_{max}$, namely

$$f(k) = f(k_{max}) + f'(k_{max})(k - k_{max}) + \frac{1}{2}f''(k_{max})(k - k_{max})^2 + \wr(k^3), \tag{4.4}$$

with $f^{(n)}(k) = d^n f(k)/dk^n$, the peak of the distribution $P(k)$ can be approximated as

$$P(k) \approx \mathbb{N}e^{f(k_{max}) + \frac{1}{2}f''(k_{max})(k-k_{max})^2} = \mathbb{N}Fe^{-\frac{(k-k_{max})^2}{-2/f''(k_{max})}}, \tag{4.5}$$

where $F = e^{f(k_{max})}$ is only a multiplicative factor, which can be put in front of the distribution, as a rescaling of the normalization $\mathbb{N}$. In particular, computing the first and the second

derivative,

$$f'(k) = \frac{1}{k} - \frac{\alpha}{k+k_0} \tag{4.6}$$

$$f''(k) = -\frac{1}{k^2} + \frac{\alpha}{(k+k_0)^2}, \tag{4.7}$$

the maximum k_{max} can be obtained from

$$f'(k_{max}) = 0 \;\Rightarrow\; k_{max} = \frac{k_0}{\alpha - 1}, \tag{4.8}$$

while for the second derivative we get

$$f''(k_{max}) = -\frac{(\alpha-1)^3}{\alpha k_0^2} \tag{4.9}$$

which as expected is negative for $\alpha > 1$.

Therefore, this power law peak assumes around its maximum a Gaussian shape with an average value $\langle k \rangle = k_{max}$ and a variance $\sigma^2 = -(1/f''(k_{max}))$, which turns out to be correctly positive if we replace $f''(k_{max})$ with the result in Eq. (4.9). In Section 4.2, we have shown how sufficiently narrow Gaussian distributions, that is with $\sigma/\langle k \rangle \lesssim 0.22$, are able to produce synchronous states, at least for small couplings. Applying this constraint in this case let us write a sort of "Gaussian synchronization condition", which defines a possible range of values for the distribution parameters α and k_0, where we can expect to find synchronous states, since the peak is well approximated by a sufficiently narrow Gaussian. This condition reads

$$\sqrt{-\frac{1}{f''(k_{max})}} \cdot \frac{1}{k_{max}} < \epsilon \tag{4.10}$$

where $0 < \epsilon \ll 1$ and in particular $\epsilon \approx 0.22$. Replacing k_{max} and $f''(k_{max})$ with Eq. (4.8) and Eq. (4.9), the final condition is independent on k_0 and it is given by

$$\sqrt{\frac{\alpha}{\alpha - 1}} < \epsilon. \tag{4.11}$$

Since such a relation is never satisfied for any value of $\alpha > 0$, these modified power law distributions $P(k) \sim k/(k+k_0)^\alpha$ cannot be approximated with a sufficiently narrow Gaussian and, as a consequence, they should never produce synchronous states in the network.

Actually, as we have observed from our numerical simulations, no synchronization transition emerges, neither for very large values of α, which in the previous Section correspond to a higher synchronizability of the network, nor for small couplings, which in general promote synchronization, at least for neurons with low connectivities, as it has been shown for the Gaussian case.

If we consider the case of an exponential initial cutoff, shown in Fig. 4.7(b), we get

$$P(k) = \mathbb{N}\frac{e^{-b/k}}{k^{\alpha}} = \mathbb{N}e^{f(k)} \tag{4.12}$$

$$f(k) = -\frac{b}{k} - \alpha \ln k \tag{4.13}$$

$$f'(k) = \frac{b}{k^2} - \frac{\alpha}{k} \tag{4.14}$$

$$k_{max} = \frac{b}{\alpha} \tag{4.15}$$

$$f''(k) = -\frac{2b}{k^3} + \frac{\alpha}{k^2} \tag{4.16}$$

$$f''(k_{max}) = -\frac{\alpha^3}{b^2}. \tag{4.17}$$

Here, the "Gaussian synchronization condition" reads

$$\frac{1}{\sqrt{\alpha}} < \epsilon, \tag{4.18}$$

which for instance for $\epsilon \approx 0.2$ is satisfied only for $\alpha > 25$, as it is confirmed from numerical results. However, this corresponds to highly unrealistic values for the power law exponent, as currently no biological, technological or social network with scale-free topology has shown such an exponent.

What clearly emerges from these modified power law distributions is that, in scale-free topologies, synchronization properties of the network are strongly influenced by the initial cutoff applied on the function. This is not surprising, since neurons with low connectivity, namely classes with small degrees, typically tend to synchronize better than the others and modifying the initial cutoff directly affects them. From one side, we need power law distributions, as shown in the previous Section, to better describe the heterogeneity of the network, taking advantage of very broad functions with large hubs without the width constraint imposed by the Gaussian case. On the other side, it has been proved that we have to accurately define a proper initial cutoff for the scale-free distribution and it is fundamental to keep its peak separate from 0.

Moreover, the emergence of a "Gaussian synchronization condition", derived from the comparison of these modified power laws with a standard synchronous Gaussian peak, underlines the importance of the Gaussian case as a reference case, if one wants to investigate the synchronization transitions in specific scale-free topologies, at least for small connectivities.

These two final issues give us a clear hint for considering synchronization transitions with a last kind of distributions, which are discussed in the next Section.

4.5 An homogeneity constraint

The discussion about the initial cutoff to set on power law degree distributions presented in the previous Section suggests the idea that the scale-free tail, and especially its exponent, is not the only important parameter to drive the synchronization properties of the network, but we need to add to this heterogeneous tail a sufficiently narrow peak, which corresponds to a homogeneous bulk of locked classes. This yields the necessity of considering distributions, whose features could somehow interpolate between a power law and a Gaussian distribution. The first distribution allows us to enhance the heterogeneity of the network connectivity in a safe way, while the second one ensures a good peak and initial cutoff, correctly weighing the classes with small degrees and setting the best conditions of synchronizability for the network.

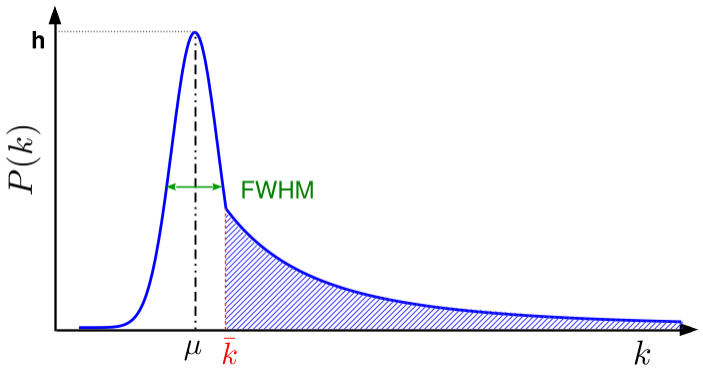

FIGURE 4.8: An example of a Gaussian distribution with a power law tail with exponent α: μ is the central degree of the Gaussian peak with height h, $FWHM$ is the full width at half maximum of the whole distribution and $\bar{k}$ is the degree at which the Gaussian peak joins with the power law tail. The dotted area represent the fraction f, that is the weight of the power law tail with the respect to the distribution.

Thus, as a final step, in order to better investigate the role of heterogeneity in driving the synchronization transitions, we choose a Gaussian degree distribution at low connectivity (small degrees) with a power law tail at high connectivity (large degrees), as follows:

$$P(k) = \begin{cases} (1-f)\, N_g\, \frac{1}{\sqrt{2\pi}\sigma} e^{-(k-\mu)^2/2\sigma^2}, & \text{if } k \leq \bar{k} \\ f\, N_p\, k^{-\alpha}, & \text{if } k > \bar{k} \end{cases} \tag{4.19}$$

where we have introduced a fraction f which weighs the power law tail with respect to the Gaussian peak, whose central value is now called μ, instead of $\langle k \rangle$, since in this case μ is no longer the average degree of the whole distribution. A typical shape of this distribution is reported in Fig. 4.8, where we put in evidence the "barrier" value $\bar{k}$ of the degree, that is the value at which the Gaussian peak joins with the power law tail, the height of the Gaussian peak and the full width at half maximum ($FWHM$) of the whole distribution.

For simplicity, we denote as $\mathcal{P} = \{\mu, \sigma, \alpha, f\}$ the set of independent parameters of this distribution. We fix the average degree and the standard deviation of the Gaussian peak, such that $\mu = 10$, $\sigma = 1$ and therefore $\sigma/\mu = 0.1$. As shown in Section 4.2, a network with such a degree distribution displays a full and well-defined synchronization scenario, with partially synchronous and asynchronous states, as g increases. Otherwise, the other parameters α and f are left free: as for scale-free topologies, the exponent α lets us control the level of heterogeneity of the network and the presence of hubs, while f tunes how many neurons will fall into the power law tail, becoming hub, and how many will lie in the Gaussian, contributing to maintain a known synchronization pattern. Fixing $\langle k \rangle$ and σ and choosing given values for α and f, the normalization constants N_G and N_p and the "barrier" degree $\bar{k}$ are strictly determined by the normalization conditions and the continuity condition, namely

$$\begin{cases} \int_0^{\bar{k}} N_G\, \frac{1}{\sqrt{2\pi}\sigma} e^{-(k-\mu)^2/2\sigma^2} dk = 1 \\ \int_{\bar{k}}^{+\infty} N_p k^{-\alpha} dk = 1 \\ (1-f)\, N_g\, \frac{1}{\sqrt{2\pi}\sigma} e^{-(\bar{k}-\mu)^2/2\sigma^2} = f\, N_p\, \bar{k}^{-\alpha} \end{cases} \tag{4.20}$$

which yields

$$\begin{cases} N_G = 1/\left[\text{erf}(\frac{\bar{k}-\mu}{\sqrt{2}\sigma}) - \text{erf}(\frac{-\mu}{\sqrt{2}\sigma})\right] \\ N_p = \frac{\alpha-1}{\bar{k}^{1-\alpha}} \\ \frac{(1-f)e^{-(\bar{k}-\mu)^2/2\sigma^2}}{\sqrt{2\pi}\sigma\left[\text{erf}(\frac{\bar{k}-\mu}{\sqrt{2}\sigma})-\text{erf}(\frac{-\mu}{\sqrt{2}\sigma})\right]} = \frac{f(\alpha-1)}{\bar{k}}. \end{cases} \tag{4.21}$$

For each parameters set $\mathcal{P}$, we first need to numerically compute $\bar{k}$ from the last row of the previous equations; then, we get N_G and N_p from the first two rows and the distribution is fully characterized. In particular, the height h of the Gaussian peak and the $FWHM$ of the distribution will depend on α and f. Since we need to consider values for the exponent α which make the variance of the power law tail diverge, we adopt that parameter as a measure of the distribution width and therefore of the connectivity heterogeneity.

Now, for each distribution identified by the parameters set $\mathcal{P}$, we analyze the synchronization transition as a function of the coupling g, as for the previous distributions. Note that this is a rather heavy computation, since on the $2D$ plane of all possible values for α and f, with in particular $2 < \alpha < 5$ and $0.1 < f < 0.8$, we have to sample some distributions and with such distributions we have to simulate the dynamics of our networks for different value of the coupling g until a transition from a partially synchronous to an asynchronous regime emerges.

The final phase diagram is reported in Fig. 4.9(a), where we plot the $2D$ space of the parameters α and f. Looking at the global synchronization properties as a function of (α, f), we can mainly divide all the considered networks into two subset: the synchronous set, marked with the symbol $\bullet$, and the asynchronous set, marked with the symbol $\times$. The first group includes all those networks, which are characterized by a critical coupling, namely which display a synchronous-asynchronous phase transition for a given value of g; the second group contains those networks which can never get synchronized, even for very small values of g.

Through this essential representation, a sharp separation between the two subsets, stressed by the thick blue line, clearly appears: the first set of more synchronizable networks lies mainly in the top-right region of this plot, while the second less synchronizable set in the bottom-left region. Neither the exponent α nor the fraction f can fully capture the behavior of this separation surface. Indeed, there exist values of α, which correspond to both synchronous and asynchronous networks, and values of f, which include both the groups.

If we now look at the color map on the background of this phase diagram (in Fig. 4.9(a)), representing the values of the $FWHM$ for each pair (α, f), we find that neither the width or the heterogeneity level of the distribution is able to explain this synchronization pattern. Otherwise, what appears to be the most important factor is the height of the Gaussian peak, as shown in Fig. 4.9(b), where the $FWHM$ values have been replace by a different color map for the height. Although it does not perfectly describe the separation between the synchronous and the asynchronous group, since the blue line does not completely fit one of the colored bands, the height of the Gaussian peak seems to be a good parameter, better than the connectivity heterogeneity, to drive the synchronization properties of the network.

Let's first consider a peak height $h = 0.327$ and the corresponding series of distributions with appropriate exponents α and fractions f, which keep this height (represented by a dashed line in Fig. 4.9(b)). In Fig. 4.10(a), we plot the synchronization transitions through the measure of the Kuramoto parameter R, computed as a function of the rescaled coupling $\tilde{g} = g/\langle k \rangle$, considering that we are comparing distributions with different average degrees. What emerges is that the network displays a partial synchronization for small coupling values and it becomes more and more asynchronous as g increases, yielding the typical transition also observed in the Gaussian case (Section 4.2). Moreover, such a framework is preserved also if we consider $2 < \alpha < 3$ and in particular $\alpha \to 2$, that is close to the point where the second moment of the power law distribution diverges.

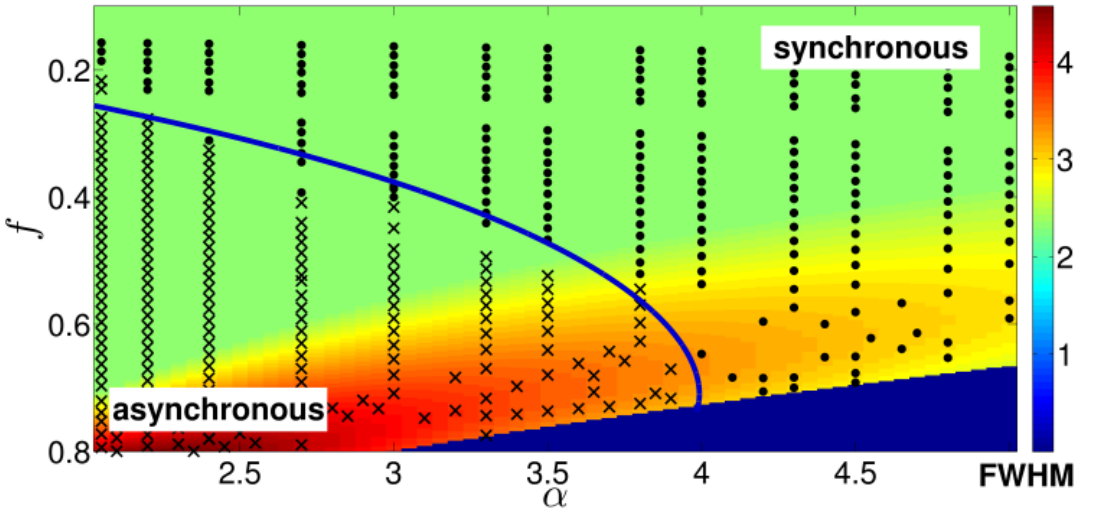

(a)

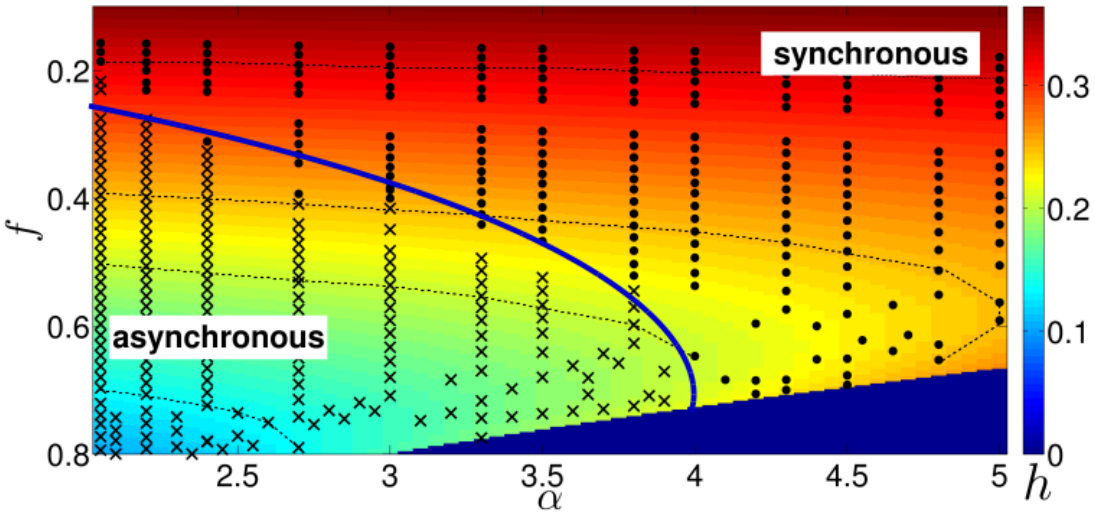

(b)

FIGURE 4.9: Synchronization phase diagram for networks characterized by Gaussian distributions with a power law tail as a function of the exponent α of the power law tail and its weight f: networks which display a synchronous-asynchronous transition for a given value of the coupling g are denoted with $\bullet$, networks which are everywhere asynchronous are represented with $\times$. The thick blue line, drawn to guide the eyes, mark the separation between these two groups. Panels (a) and (b) plot the same data with a different color map on the background: in (a) we represent the values of $FWHM$ of the whole distribution, while in (b) the value of the Gaussian peak height. The respective legends of these color maps are reported in the right. The dashed lines link points which correspond to the same height h and in particular from the top to the bottom: $h = 0.327$, $h = 0.242$, $h = 0.207$ and $h = 0.136$. Synchronization transitions as a function of g for those points are reported in Fig. 4.10. The blue triangle in the right bottom represents a region of not acceptable values for (α, f), since they correspond to a discontinuous distribution. Note that for all the points close to the separation line the fluctuations around the critical point of the transition typically diverge and it becomes rather difficult to identify the synchronous-asynchronous transition. For all these points, we should perform finite-size scaling analyses, as explain in Section 4.3, which are numerically heavy but necessary in order to better describe the separation between the two groups.

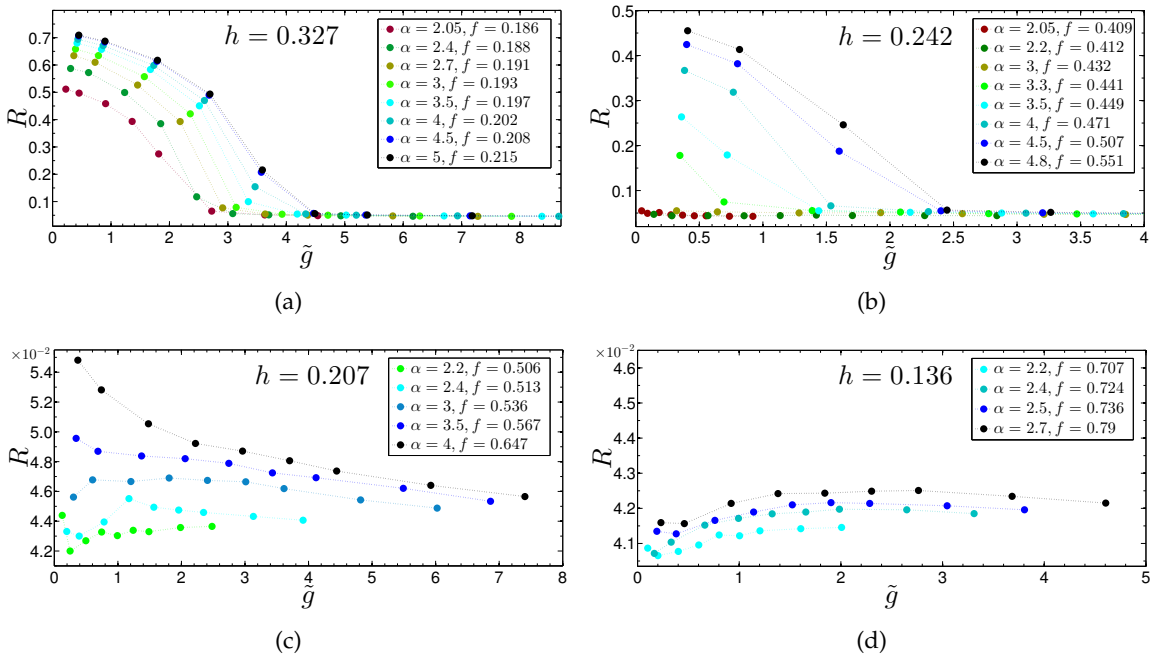

FIGURE 4.10: Synchronization phase transitions for networks characterized by Gaussian distributions with a power law tail. We fix the height of the Gaussian peak and we consider pairs of values (α, f) which respect that constraint. In each panel we report the height h and values of (α, f) considered. For each (α, f), we plot the Kuramoto parameter R as a function of the rescaled coupling $\tilde{g} = g/\langle k \rangle$. For all these networks, we have simulated $M = 500$ connectivity classes and we have set $\mu = 10$ and $\sigma = 1$.

If we lower the Gaussian height, for instance to $h = 0.242$, and we repeat the same analysis, reported in Fig. 4.10(b), we note that the network is less synchronizable and that for exponents smaller a given critical value, let's say $\alpha < 3$ referring to Fig. 4.10(b), no transition emerges, even for small values of the coupling g.

For other heights, as $h = 0.207$ shown in Fig. 4.10(c), a more disordered framework arises and we observe some ambiguous curves, where it is rather difficult to distinguish which values of (α, f) actually yields a synchronous regime at least for small couplings or not. In that case, we need to perform the same scaling analysis presented for the simple power law distributions, choosing different discretizations M of the degree distribution, repeating the measure shown in figname4.10 for $M = 250, 500, 1000$ and 2000 and comparing the values of the rescaled Kuramoto parameter R_{res}, as defined in Section 4.3. As it has been explained in that Section, where the scaling of R_{res} fails and the transition curves, which in the asynchronous regime overlap, begin to split, there we find the onset of synchronization and we can decide if the transition actually occurs.

Finally, for very small value of h, as for $h = 0.136$ in Fig. 4.10(d), no synchronous regime can be detected.

As a conclusion, this implies that in our excitatory networks, characterized by Gaussian degree distributions with a power law tail, the initial "paradox of heterogeneity" can be reworded rather as a homogeneity constraint, which now has a precise formulation in terms of features of the distribution: if we want more synchronizable networks, we should ensure that the eventual Gaussian peak, present in the connectivity distribution, contains enough nodes, namely it is necessary to have enough nodes with similar degrees. Indeed, higher peaks lead to more synchronous systems, independently on the other parameters of the model.

In the next Chapter we discuss how the synchronization properties of our neural networks

change when we add a new ingredient, that is the inhibitory mechanism for synaptic transmission, in addition to the connectivity heterogeneity, encoded by the presence of hubs.

Chapter 5

The role of inhibitory hubs in driving synchronization

Once we have discussed the synchronization properties in a purely excitatory network, as a functions of its connectivity heterogeneity or in terms of an homogeneity constraint, as emerged in the previous Section, in this last Chapter we add to the network a new ingredient, that is the synaptic inhibitory mechanism, and see how the synchronization scenario changes.

In particular, starting from some experimental observations, we investigate the role of inhibitory hubs and the interplay between the fraction of inhibitory neurons present in the network and their hub character in driving synchronization transitions of our neural network. In these transition we observe states of dynamical balance between excitation and inhibition, which correspond to the total synchronization, and an interesting metastable regime which is characterized by a long memory of external inputs applied to the network. An extension of this Chapter can be found in Appendix D, where we more precisely compare the results obtained simulating the dynamics of the HMF formulation and of the finite connectivity network, showing that the convergence between these two approaches is not so trivial.

5.1 Inhibitory component and hubs in neural networks

Considering what has emerged from the previous Chapter about the connectivity pattern of a neural network, one of the features which seems to particularly influence the onset or the loss of synchronization is the presence of hubs, i.e. neurons with a degree much larger than the average connectivity of the whole network. More precisely, such neurons are introduced in a system when typically we consider scale-free topology, as those we have discussed in Sections 4.3, 4.4, 4.5.

Since each hub typically receives a large amount of synaptic inputs and it is also connected to a large amount of other units, it is natural to suppose that its firing activity orchestrates the dynamics of a macroscopic fraction of neural population, as a clock which gives a common rhythm to all units. Thanks to graph theory methods, as motif structures and centrality indices measures, the presence of hub regions has been recently detected in the mammalian cerebral cortex, as shown in [111]. Hubs observed in the anatomical and functional connectivity (see Section 3.1) give a fundamental support in information transmission among different areas of the brain and in performing cognitive functions, although they appears to be highly vulnerable to disconnections and brain disorders [8, 138]. The mapping procedure of multiplex hubs in human functional brain networks could also be applied to distinguish between healthy and schizophrenic patients, as shown in [139].

In addition to connectivity patterns and presence of hubs, also synaptic inhibition turns out to highly influence the neural population activity and synchronization. The presence of an inhibitory component in brain neural networks has been currently prove in almost all mammals neural systems, as shown for instance in [9, 140]. In particular in cortical regions, it has

been observed that, although the neural population is mainly composed by excitatory pyramid neurons, a consistent amount of cells are inhibitory and especially inhibitory interneurons. Interneurons are one of the three types of neurons present in the cerebral cortex and include all those cells which are not specifically classified as sensory or motor neurons [3]. Most interneurons are inhibitory, since the GABA or γ-aminobutyric acid neurotransmitters typically released by their synapses produce an inhibitory response in the postsynaptic neuron, which reduces its membrane potential and therefore inhibits the emergence of a new postsynaptic action potential (see Section 2.1). More precisely, many experimental observations suggest that the fraction of inhibitory neurons of cortical system is about 10-30%, as for instance reported in [9, 81, 141] and in particular in [142] in mouse somatosensory cortex.

One of the first experimental evidences of the crucial role of inhibition in driving the dynamics of neural populations, in particular in the visual cortex, was performed in 1998 by Borg-Graham and colleagues [143]. With a new experimental technique, they found that visual stimuli are typically followed by an overall inhibitory response of the network, as if inhibition served as a general neural segregation. A further confirmation of this segregation function was obtained by Cohen and Miles in 2000 [144], who tried to suppress the excitation and inhibition receptors in hippocampal areas of guinea-pigs, showing that an excitation of inhibitory cells strongly reduce the overall population activity. Since isolated neurons display a much higher firing rate than coupled neurons in an ensemble, inhibition can be seen as a fundamental ingredient, able to change and especially depress the default activity of single cells and to stabilize the network dynamics, which otherwise, in presence of continuously high spiking rates, would be highly noisy.

In the last few years, the role of inhibition has been investigate also in computational neuroscience, especially in order to try to provide a theoretical justification of the previously mentioned inhibitory fractions, which have been experimentally observed in nervous systems of many different species. In [145], it turns out that multi-task learning of Boolean rules in neural networks it optimized if a fraction of 30% inhibitory synapses is included in the system, since this percentage maximizes the learning performances, ensuring at the same time the right level of excitability necessary for the system response.

For what concerns synchronization, inhibition seems to promote firing activity in an excitatory and inhibitory neural networks better than excitation synchronous, as for instance shown in [73]. Interplay between the excitatory and the inhibitory population can produce perfectly synchronous states in fully coupled networks or partial synchronization in sparse random networks, which can be improved when the decay time constant of inhibitory dynamics is increased [146]. In [147], synchronization transition from synchronous to asynchronous regimes in excitatory and inhibitory integrate-and-fire neurons as a function of the balance between these two synaptic mechanisms and of the frequency of an external input. Moreover, in the asynchronous regime, two types of incoherent activity with different computational properties can be detected in sparse networks, as shown in [148], as a function of the coupling: irregular firing activity at constant rates, which promotes fast information transmission, for weak synaptic coupling and irregular firing activity with large fluctuations, which allows a more complex information processing. Finally, it has been recently observed [149] that in pulse-coupled heterogeneous inhibitory networks with sparse random connectivity, inhibition dynamics from one site suppresses the population activity but from the other site it also produces a neural reactivation.

Now, in order to achieve a unifying view, one might wonder how connectivity structure and inhibition cooperate in driving synchronization activity of neural populations. Actually, in 2009, Bonifazi and colleagues put into evidence hub neurons are typically inhibitory, confirming the hypothesis of an interplay between these two ingredients [150]. Through fluorescence imaging techniques, they have found scale-free topologies in the functional connectivity of hippocampal regions of rats and mice, with distribution exponents equal to $1.1 - 1.3$ and therefore

we have proved the existence of hubs, which at the same time turn out to belong to the subpopulation of inhibitory interneurons. The primary role played by these inhibitory hub neurons in driving the synchronous dynamics of neural ensembles also emerge in other recent works, as for instance [151, 152].

Within this framework, in this Chapter we investigate theoretically and numerically the interplay between the presence of hub nodes in the connectivity pattern and the inhibitory component in the synaptic transmission in defining the synchronization properties of our neural networks. To do that, we now consider excitatory inhibitory neurons, whose dynamics is fully described by the equations introduced in Section 3.4 and in particular in Eqs. (3.28). As shown in Section 3.5, we are allowed to apply to the finite connectivity network the heterogeneous mean field formulation and therefore we simulate the dynamics expressed in Eqs. (3.49). A comparison between the results obtained from simulations of the HMF approach and finite connectivity networks can be found in Appendix D, where we show that the dynamics converge one to each other as the network connectivity increases. Although the effectiveness of the HMF in correctly describe the system dynamics in thermodynamic limit has been proved in [12, 78, 80], in our networks this limit is not trivial, mainly due to the effects of finite connectivity noise, as shown in Appendix D.

5.2 Synchronization effect of inhibitory hubs

In order to investigate how the synchronization properties of a network change in the presence of hub inhibitory neurons we need to find two parameters on our networks, which let us directly tune how many inhibitory neurons are present and how large the hubs are with respect of the other nodes, let's say how strong their hub character is. To do that we can properly define two distributions $P_E(k)$ and $P_I(k)$ for these two populations, so that the inhibitory neurons related to the second distribution are also hubs, shifting for instance $P_I(k)$ towards larger degrees.

For what has emerged in the previous Chapter and since we cannot consider the power law distributions detected by Bonifazi and colleagues [150], here we choose two Gaussian distributions with the same standard deviation σ and different average degrees $\langle k_E \rangle$ and $\langle k_I \rangle$, such that $\Delta = \langle k_I \rangle - \langle k_E \rangle$.

Keeping fixed the excitatory average degree and varying the inhibitory average connectivity $\langle k_I \rangle$, this distance Δ between the two Gaussian will tune the hub character of inhibitory nodes, while the fraction f_I of inhibitory neurons, defined as

$$f_I = \int P_I(k) dk, \tag{5.1}$$

will control their weight with respect to the excitatory population, whose fraction is defined as $f_E = \int P_E(k) dk$.

Note that for the normalization condition $f_E + f_I = 1$ the connectivity distribution for a generic neuron is $P_E(k) + P_I(k)$. A schematic representation of this double Gaussian distribution is reported in Fig. 5.1. In particular we set $\sigma = 10$ and $\langle k_E \rangle = 100$, so that the parameter $\sigma / \langle k_E \rangle$, equal to 0.1, ensures a quasisynchronous regime at least at small couplings, i.e. $g \lesssim 50$, as shown in Section 4.2. For this reason,in all results reported in this Chapter the synaptic coupling g is fixed, equal to 30.

First, let us fix $\Delta = 250$ in order and observe the dynamical configurations of the network as a function of the inhibitory fraction f_I. As it is shown by the raster plots in Fig. 5.2(b), when f_I is close to 0, as $f_I = 0.1$ for instance, the network display the typical pattern of partial synchronization, which has emerged in the previous Chapter: excitatory neurons with low degree are locked, while all the others (excitatory nodes with higher degree and inhibitory

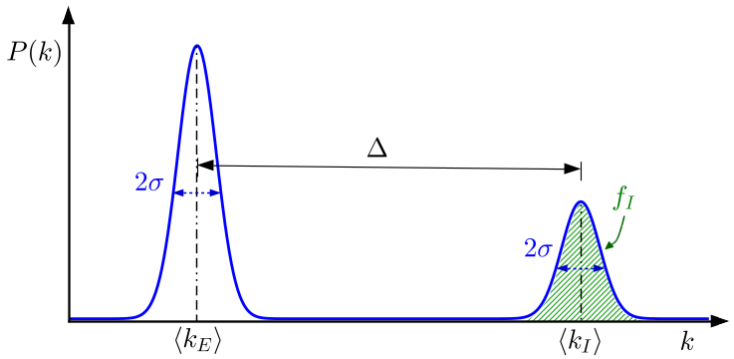

FIGURE 5.1: Example of a double Gaussian distribution $P(k)$. The left Gaussian corresponds to the excitatory connectivity, while the left Gaussian to the inhibitory connectivity. Both Gaussian have the same standard deviation. The distance between the central values of these two Gaussian is Δ and it controls the hub character of the inhibitory neurons: small values of Δ mean that the inhibitory population connectivity is not so large with respect to the excitatory population, while large values of Δ mean that the network include big hubs. The green-dashed area represents the inhibitory fraction f_I: the larger f_I, more inhibitory neurons are present in the network. In particular, in our simulations we fix $\langle k_E \rangle = 100$ and $\sigma = 10$ and we vary Δ and f_I.

hubs) are unlocked with a quasiperiodic dynamics. The plot of the $\langle ISI_k \rangle$ as a function of k, corresponding to this dynamics, is reported in Fig. 5.2(a) and its inset with the same colour code.

For larger values of f_I , the network synchronization grows, since the plateau of locked classes in Fig. 5.2(a) in the excitatory region stretches, while a new inhibitory plateau also appears. Then, the network achieves a total synchronization regime for a single value of f_I (which for $\Delta = 250$ is 0.22), where all neurons are locked, as shown in the central raster plot of Fig. 5.2(b), and $\langle ISI_k \rangle$ of both excitatory and inhibitory population belong to two identical plateaus. Finally, for even larger inhibitory fractions the network starts lose coherence and becomes more and more asynchronous.

As in the previous Chapter, in order to quantify the synchronization level of the network, we compute the Kuramoto parameter R, as a function of the inhibitory fraction f_I and in particular for each value of Δ, we vary f_I from 0 to a value that corresponds to the totally asynchronous regime and we plot in Fig. 5.3 the parameter $1 - R$ vs f_I in a semilogarithm scale, which let us to make synchronizations transitions more evident as peaks.

For all values of $\Delta \geq 0$, we observe that R first increases towards 1, meaning that, at small values of f_I, increasing the fraction of inhibitory neurons really improves the synchronization of the whole network. Then, the synchronization level reaches a peak, where the network is totally synchronized and R is very close to 1. Note that for different values of Δ this peak corresponds to a different and specific value for the inhibitory fraction. Finally, R quickly decays towards 0 and the network becomes asynchronous.

When inhibitory neurons do not feature a higher connectivity with respect to the excitatory ones, that is when $\Delta = 0$, it turns out that the inhibitory-driven synchronous regime is observed only for high values of f_I, that is for $f_I \sim 0.5$. Nevertheless, as reported in Section 5.1, experimental observations suggest that the fraction of inhibitory neurons is much smaller ($f_I \sim 10 - 30\%$) [9, 81, 141, 142]. Actually, in our networks, we show how by increasing the hub character of inhibitory neurons, namely by increasing Δ, one can observe such highly synchronized regime for smaller and smaller values of f_I, reaching phenomenological values (grey-shaded region in Fig. 5.3) for $2 \times 10^2 \lesssim \Delta \lesssim 10^3$.

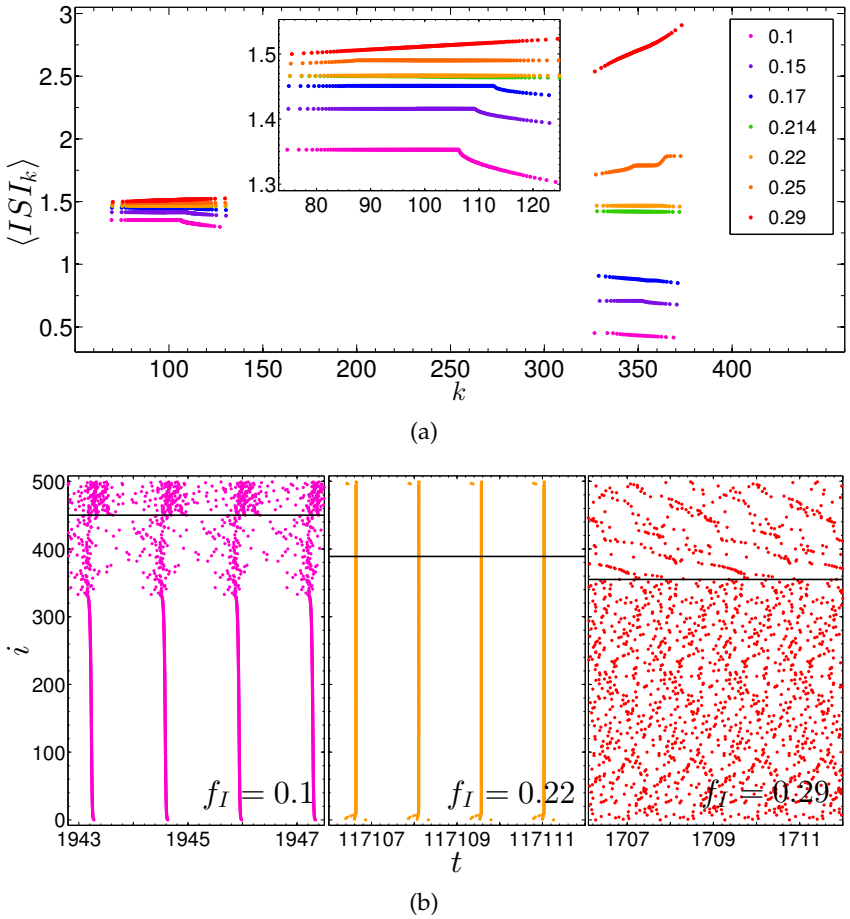

FIGURE 5.2: (a) $\langle ISI_k \rangle$ as a function of the degree k for networks with different inhibitory fractions f_I (see the legend). Δ is fixed at 250 and the number M of connectivity classes is 500. In the inset we show a zoom of the excitatory plateau. In panel (b) we display snapshots of the raster plots for different inhibitory fractions, to represent the three main dynamical regimes: partial synchronization for $f_I = 0.1$, total synchronization for $f_I = 0.22$, and an asynchronous state for $f_I = 0.29$.The degree classes below (above) the black line are excitatory (inhibitory). These plots refer to different dynamical regimes, however a time unit in the abscissa axis corresponds to about one global oscillation of the network (after this time interval all neurons have fired at least once). Image from [115].

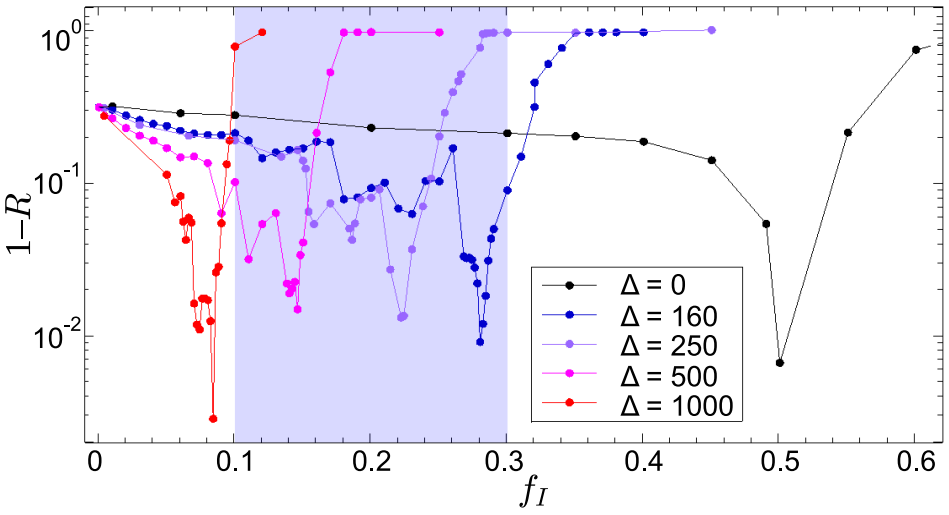

FIGURE 5.3: Network synchronization from the measure of $1 - R$ (where R is the Kuramoto parameter) as a function of f_I for different values of Δ (see the legend), in semilogarithmic scale. In all networks M is equal to 500. The closer to 0 the parameter $1 - R$ is, the more synchronous the network. The grey-shaded area represents the interval of inhibitory fractions, which has been really observed in some brain tissues. Without hub nodes ($\Delta = 0$, black data), the network reaches a high synchronization level out of this region, differently from $160 \lesssim \Delta \lesssim 500$. Therefore, if we want to build synchronous networks with inhibitory fractions close to real values, the inhibitory neurons should be hubs, with an average degree 3-6 times greater than the excitatory average degree. Image from [115].

Apart from the quantitative reliability of our results with respect to the experimentally suggested fractions of inhibitory neurons, Fig. 5.3 shows how the hub character of inhibitory neurons is a fundamental ingredient to allow a small fraction of inhibitory nodes to drive the synchronization of the overall network, thus underlining the importance of inhibitory neurons connectivity in affecting network synchronization.

5.3 Balance regime

One of the main argument presented in the previous Section is that for each value of Δ there always exists a narrow region for the inhibitory fraction, where the network is highly synchronized. This is a consequence of a dynamical balance between the excitatory and the inhibitory mechanisms, which actually emerges in real neural ensembles when both populations are present.

Since many neural systems are known to work in that regime, the role of this dynamical balance has been largely investigated and it seems to be related to specific neural diseases, such as autism and schizophrenia. For instance, it has been observed in mice prefrontal cortex that a modification of the cellular excitatory/inhibitory balance highly influence the cellular information processing and produce specific behavioural disorders [153]. Some theoretical analyses show that the temporally irregular spiking patterns [154], chaotic dynamics [155] of network even in the presence of external inputs and the memory capability of the network [145, 156] could be directly determined by the balance . Moreover, dynamical transitions driven by the balance between different activity states in excitatory and inhibitory networks emerge also in [157] or in a set of coupled cortical macrocolumns, as shown in [158].

Concerning our neural networks model, in order to make the totally synchronous phase emerge, it is necessary that all neurons follow the same dynamics and therefore that the evolution of $v_k(t)$, expressed in Eqs. (3.49), no longer depends on the degree k. This implies that the last term in the potential equation has to be 0. Applying the definition in Eqs. (3.47) of synaptic fields received by both the excitatory and the inhibitory population, it turns out that the excitatory and the inhibitory contributions in producing that fields cancel each other out. Considering a neuron of type † (where † can be E or I) and writing its synaptic field $Y_\dagger(t)$ according to Eqs. (3.47), we obtain a perfect field subtraction, that is

$$Y_{\dagger,E}(t) - Y_{\dagger,I}(t) = 0, \tag{5.2}$$

which using the definition in Eq. (3.48) becomes

$$\int \frac{P_E(k)\, k\, y_k^{(\dagger,*)}}{\langle k \rangle}\, dk = \int \frac{P_I(k)\, k\, y_k^{(\dagger,*)}}{\langle k \rangle}\, dk. \tag{5.3}$$

Now, since in the totally synchronous regime all microscopic variables are equal, we have $y_k^{(\dagger,*)} = y\ \forall k$ and we can factorized them out of the integrals:

$$\frac{y}{\langle k \rangle} \int P_E(k)\, k\, dk = \frac{y}{\langle k \rangle} \int P_I(k)\, k\, dk. \tag{5.4}$$

Simplifying $y/\langle k \rangle$, we obtain that the left (right) integral represents the average value of $P_E(k)$ ($P_E(k)$) multiplied by the excitatory (inhibitory) fraction f_E (f_I), as defined in Eq. (5.1). Finally, replacing $f_E = 1 - f_I$ and $\langle k_I \rangle = \Delta + \langle k_E \rangle$, we get the final balance condition as follows

$$\langle k_E \rangle f_E = \langle k_I \rangle f_I \Rightarrow \langle k_E \rangle (1 - f_I) = (\Delta + \langle k_E \rangle) f_I. \tag{5.5}$$

Solving this last equation for f_I we can compute for each Δ and $\langle k_E \rangle$ the inhibitory fraction f_I^B for the balance regime, where we expect to find the total synchronization. Actually, we have verified that, by fixing the inhibitory fraction to the predicted balance value, we obtain the synchronous peaks, shown in Fig. 5.3, and the maximum Kuramoto parameter R, which is very close to 1 ($R = 0.987 - 0.997$), for all the considered values of Δ. Furthermore, in the balance regime all neurons are locked and characterized by the same period, equal to the period of the free LIF oscillator, that can be computed from Eq. (3.10) with $a = 1.3$, yielding $\langle ISI_k \rangle = 1.466,\ \forall k$.

Out of this balance phase, we naturally expect that one of the two mechanics, excitatory or inhibitory, exceeds the other. In order to better quantify the relative weight of the excitatory and the inhibitory component in driving the overall dynamics, we introduce the following quantities:

$$\begin{aligned} W_E &= \left\langle \frac{Y_{EE}(t) - Y_{EI}(t)}{Y_{EE}(t) + Y_{EI}(t)} \right\rangle, \\ W_I &= \left\langle \frac{Y_{IE}(t) - Y_{II}(t)}{Y_{IE}(t) + Y_{II}(t)} \right\rangle, \end{aligned} \tag{5.6}$$

where the angle brackets represent the temporal average over a sufficiently large number of map integration steps. W_E refers to the field received by an excitatory neuron, while W_I refers to the field received by an inhibitory neuron. If $W_E \simeq W_I \simeq 1$, this means that the dynamics of the whole network is purely excitatory and inhibitory neurons do not substantially contribute to the global fields. Otherwise, in the limit of $W_E \simeq W_I \simeq -1$ the dynamics is totally driven by

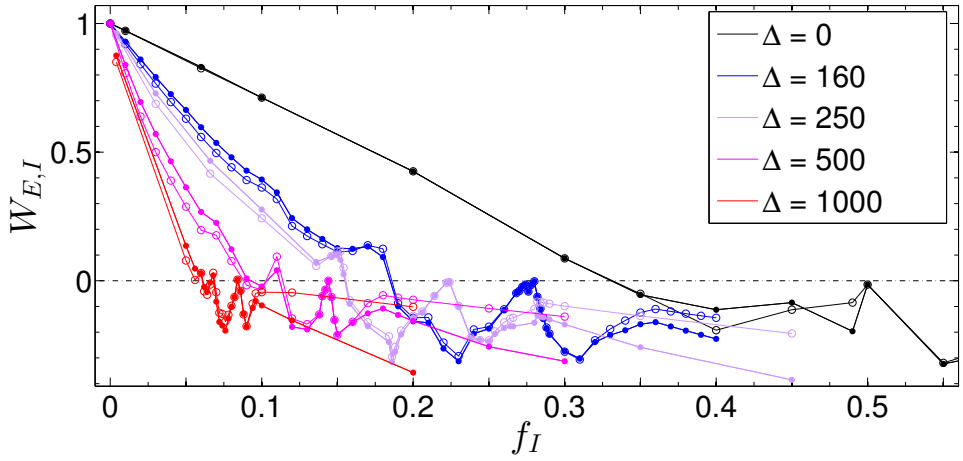

FIGURE 5.4: Relative weights of the excitatory and the inhibitory component in driving the networks dynamics with $M = 500$ connectivity classes, from the measure of W_E and W_I for different values of Δ (see the legend) and f_I. The balance value f_I^B of the inhibitory fraction for which $W_E = W_I = 0$ is 0.5 for $\Delta = 0$, 0.28 for $\Delta = 160$, 0.22 for $\Delta = 250$, 0.143 for $\Delta = 500$ and 0.083 for $\Delta = 1000$. Image from [115].

the inhibitory mechanism, even though this limit is theoretical, since a purely inhibitory network is not in a spiking regime. In Fig. 5.4 we plot W_E (with filled circles) and W_I (with empty circles) as a function of f_I for the values of Δ considered inFig. 5.3. Comparing what emerge in these two plots, we immediately observe that for the balance value f_I^B of the inhibitory fraction we get $W_E = W_I = 0$ and this corresponds to the maximum synchronization displayed by the Kuramoto parameter.

For each value of Δ, as the fraction of inhibitory hubs increases, the network dynamics becomes more inhibitory (in Fig. 5.4 W_E and W_I are indeed decreasing), while the synchronization improves (in Fig. 5.3 R is indeed increasing), starting from a partially synchronous regime, until the totally synchronous state is reached for the balance value of f_I. However, we see that the increase of f_I does not necessarily lead to a monotonous increase in the inhibitory contribution, but some unexpected oscillations Fig. 5.4 appear, due to nontrivial equilibrium mechanisms between the excitatory and the inhibitory dynamics outside the balance region.

After the balance regime, the further increase of f_I leads to the prevalence of the inhibitory dynamics, since both W_E and W_I become negative, and it gives rise to asynchronous regimes. Note that this synchronization transition is repeated for all the considered values of Δ, although it occurs in a narrower interval of f_I as Δ enhances.

In particular, when Δ has intermediate values, i.e. $150 < \Delta < 500$, the region which precedes the balance (for example $0.2 < f_I < 0.214$ for $\Delta = 250$) is characterized by a highly metastable regime of partial synchronization, where almost all excitatory neurons are locked with very similar frequencies but different phases and therefore they split into different synchronized clusters, as we can see in the raster plots in Fig. 5.5. In this regime, inhibitory neurons are unlocked, even if they spike almost simultaneously with one of the excitatory locked groups, but the group varies in time. Moreover, the system is highly metastable, since the configuration of the synchronous excitatory clusters changes on very long-time scales, typically of thousands of global oscillations: looking for instance at Fig. 5.5 the raster plots are different snapshots taken during an evolution of the same network.

As one can expect, the structure of these metastable states depends on the initial conditions of the microscopic variables. In particular, if one imposes synchronous initial conditions, that is potentials and synaptic resources equal for all neurons, the dynamics reaches a configuration where a single cluster of synchronous neurons is present and still some are unlocked.

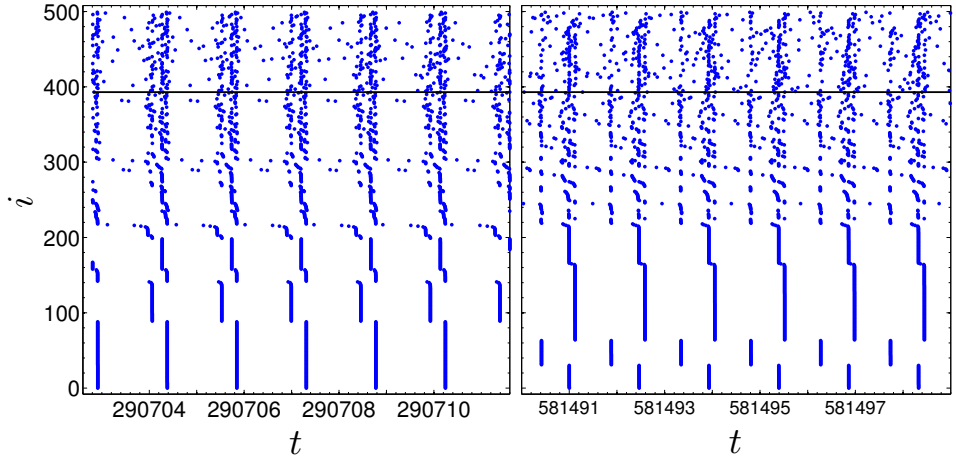

FIGURE 5.5: Raster plots of a metastable partially synchronous state for the network with $M = 500$, $\Delta = 250$, and $f_I = 0.214$, starting from random initial conditions. These plots are two snapshots, taken at different times during the same dynamical evolution. The degree classes below (above) the black line are excitatory (inhibitory). Image from [115].

This configuration seems to be the asymptotic stable situation since, at variance with Fig. 5.5, we do not observe a system metastability on long-time scales. However, we never reach such a total synchronous configuration when the system starts from random initial conditions, an evidence of the slow dynamics. For this reason, we point out that in Fig. 5.3, the value of the Kuramoto parameter of networks with this metastable dynamics has been computed referring to the total synchronous state, namely to the state the network assumes using total synchronized initial conditions. The robustness of the metastable dynamics is also preserved, even when we modify the discretization of the continuous distribution $P(k)$ and therefore the amount of the simulated connectivity classes.

In the next Section we see an important feature of these metastable states, which emerges when an external stimulus is applied to the network.

5.4 Long-time memory after an external stimulus

The metastable states which, as we have shown in the previous Section, in some cases precedes the balance regime are considered to play an important role for the cognitive functions performed by the network. For instance, metastability, which somehow can measure the dynamical flexibility of a neural ensemble, seems to be a crucial feature when the system undergoes lesions or hubs removals on both global and local connectivity [159].

In our networks, we suppose that these metastable partially synchronous states, like those in Fig. 5.5, are more efficient than other dynamical configurations in storing information, such as for example information coming from an external stimulus applied to the network, as due to their slow dynamics they can be affected by the external perturbation longer than the other regimes. Indeed, since the configuration of the synchronous excitatory clusters depends on the initial conditions and changes on long-time scales, an external synchronous stimulus, creating a new group, can produce an alteration of the network dynamics for long-time intervals.

This is why, in order to investigate the reaction of our system to external inputs and therefore its input processing capability, we particularly focus on the transient dynamics at the stimulus offset. Moreover, the space trajectory of the system in this transient has been supposed to be crucial for the stimulus detection. More precisely, the longer the time to return to the unperturbed state is, the better the system is able to detect and distinguish the input, as it has

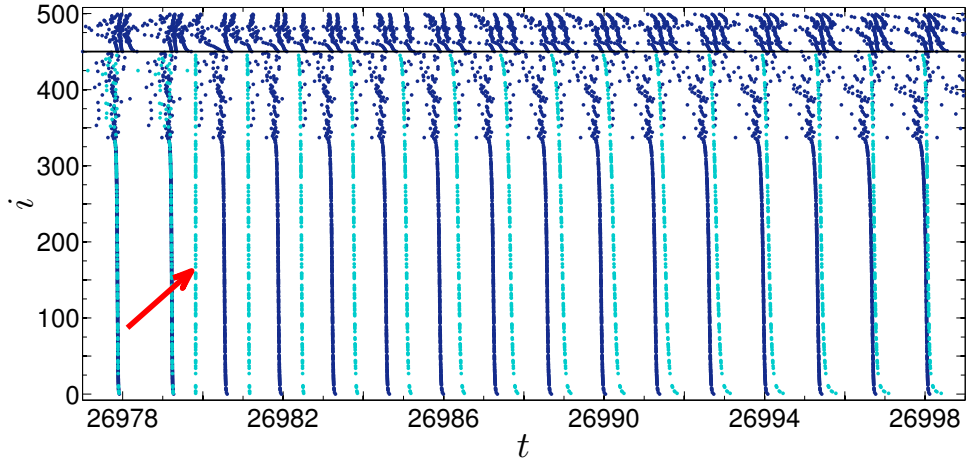

FIGURE 5.6: Raster plot of a network with $M = 500$ connectivity classes, $\Delta = 250$ and $f_I = 0.1$. At a given time (see the red arrow), we apply a synchronizing external stimulus to 30% of excitatory neurons, randomly chosen. After about ten global oscillations, the stimulated nodes recover the initial dynamics. The degree classes below (above) the black line are excitatory (inhibitory). Light (dark) blue dots represent the spike events of stimulated (not stimulated) nodes. Image from [115].

been shown in [160], or to optimize inputs representations in a sensory networks, as reported in [161] in particular for what concerns odour stimuli.

Now, let's consider a fixed value for $\Delta = 250$ and vary f_I, so that all the different dynamical regimes, including in particular the metastable partially synchronous states, can be explored as a function of the increasing inhibitory fraction. We choose to stimulate only the excitatory nodes, since they are the most abundant in real networks, as it has been experimentally observed, and therefore they are more likely affected by external perturbations with respect to inhibitory cells. In all networks, after the stationary state has been achieved, we randomly perturb 30% of the excitatory neurons, synchronizing them artificially: indeed, we can easily force the simultaneous firing of these selected neurons setting their potential variable to 1. As a rule, in order to better compare transient dynamics, we apply the stimulus when the excitatory field $Y_E(t)$ reaches its minimum value (see Fig. 5.6). Such forced synchronization and in particular the amount of stimulated neurons, that actually may represent external visual or odour inputs, could encode the intensity of the stimuli: the higher the number of synchronous units the higher the release of neurotransmitters resources y_k due to the spiking of forced excitatory neurons. In fact, synchronous firing activity in a neural population is a typical response to different stimuli, such as visual [162], odorous [163] or tactile stimuli [164].

After the perturbation, we compute as a function of time the reduced Kuramoto parameter R(t) of the neurons which has been initially boosted to 1 by the input. Then we measure the time required to return to the original value and therefore how long the network takes to absorb the external stimulus and come back to the original dynamical scenario. In Fig. 5.7 we plot the evolution of the parameter $1 - R(t)$ as a function of time, for different f_I. At the beginning, $1 - R(t)$ is close to 0, because the stimulus artificially improves the phase coherence of the stimulated cluster; then it increases, in a fast or slow way depending on the inhibitory fraction which is present, and it returns to the original value, represented by the plateau on the right of Fig. 5.7.

We observe that, when the inhibitory fraction is too small or too high, the network quickly destroys the new synchronization imposed by the stimulus and after about ten oscillations, namely at $t \sim 10$, the initial state is recovered. In the network with the metastable dynamics, the duration of the perturbation is 20 times longer. Therefore, we can state that in a partially

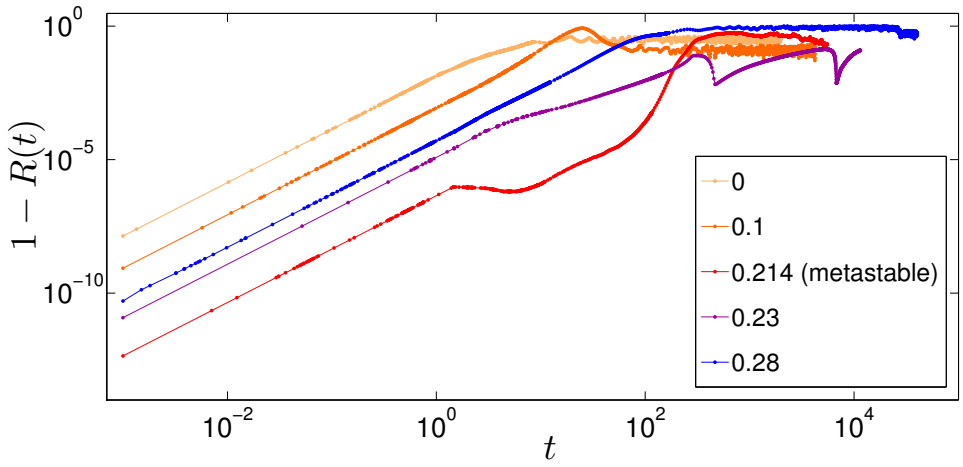

FIGURE 5.7: Transient dynamics at the stimulus offset: return to the original synchronization level after the application of an external input. We plot the parameter $1 - R(t)$ of the stimulated nodes as a function of time, for networks with $M = 500$, $\Delta = 250$, and different values of f_I (see the legend). The external synchronous stimulus is always applied at $t = 0$ to 30% of excitatory neurons, randomly chosen. Image from [115].

synchronized configuration, the metastable dynamics of the network stores information of a synchronous perturbation for long-time scales.

The initial growth of the reduced Kuramoto parameter, shown Fig. 5.7, in which seems to follow a simple power law, namely $1 - R(t) \sim t^2$, can be directly explained by expanding $R(t)$ for small t. Written the reduced Kuramoto parameter as

$$R(t) = \left| \frac{1}{M} \sum_{k=1}^{M} e^{i \frac{t - t_{k,n}}{t_{k,n+1} - t_{k,n}}} \right|, \tag{5.7}$$

where the sum runs only on the nodes which have received the synchronous stimulus. For those nodes $t_{k,n} = 0$ and in the limit for $t \to 0$, we get

$$\begin{aligned} R(t) &\approx \left| \frac{1}{M} \sum_{k=1}^{M} \left(1 + i \frac{t}{t_{k,n+1}} - \frac{1}{2} \frac{t^2}{(t_{k,n+1})^2} \right) \right| \\ &\approx \sqrt{1 - \frac{t^2}{M} \left(\sum \frac{1}{(t_{k,n+1})^2} \right) + \frac{t^2}{M^2} \left(\sum \frac{1}{t_{k,n+1}} \right)^2} \\ &\approx 1 - \frac{t^2}{2} \left(\left\langle \frac{1}{(t_{k,n+1})^2} \right\rangle - \left\langle \frac{1}{t_{k,n+1}} \right\rangle^2 \right), \end{aligned} \tag{5.8}$$

as we expected from Fig. 5.7.

Similar plots can be obtained also for different connectivities of the inhibitory hubs, since we repeated the same analysis on network with $\Delta = 160$ and $\Delta = 500$: when the prebalance regime is characterized by partially synchronous metastable states, the time required to return to the original synchronization level for those states is at least an order of magnitude longer than for the other regimes displayed by each network, as Fig. 5.7.

We also verify the robustness of our results with respect to the specific time we choose to switch on the perturbation: the response of the network to a given stimulus is indeed independent of the time when the stimulus is applied, as we show in Fig. 5.8(a). Here, we randomly

choose four different times to apply the same stimulus to the same network, so now the perturbation does not necessarily occur at the minimum of the excitatory fields $Y_E(t)$. In all trials we obtain similar transient dynamics and the relaxation times are consistent.

The robustness of out results has also been proved with respect to the number of stimulated neurons, since the same qualitative results have been obtained considering different fractions of excitatory neurons, as shown in Fig. 5.8(b).

Note that we always exclude stimuli larger than 50%, as these cannot be considered a perturbation of the system dynamics. Moreover, though different stimuli will generally correspond to different responses of the system, as the release of neurotransmitters y_k produced by the external input depends on the intensity of the input itself, it should be underlined that we are allowed to compare data obtained in different stimulations, because the quantity $1 - R(t)$ refers only to the perturbed neurons. We observe that,independently of the input intensity, from a qualitative point of view the metastable states are always affected by the external perturbation for times that are an order of magnitude longer than the other dynamical regimes of partial synchronization.

Let us point out that an intriguing result of this analysis is that, in order for the system to work in such an efficient regime for storing information, the network should be closed to the balance state where the connectivity ratio between inhibitory and excitatory neurons is equal to the inverse of the corresponding balances fractions, as shown in Eq. (5.5). This result clearly depends on the nature of our model and on the specific distribution of network connectivity we have chosen, but nonetheless it is an interesting prediction that might be tested experimentally.

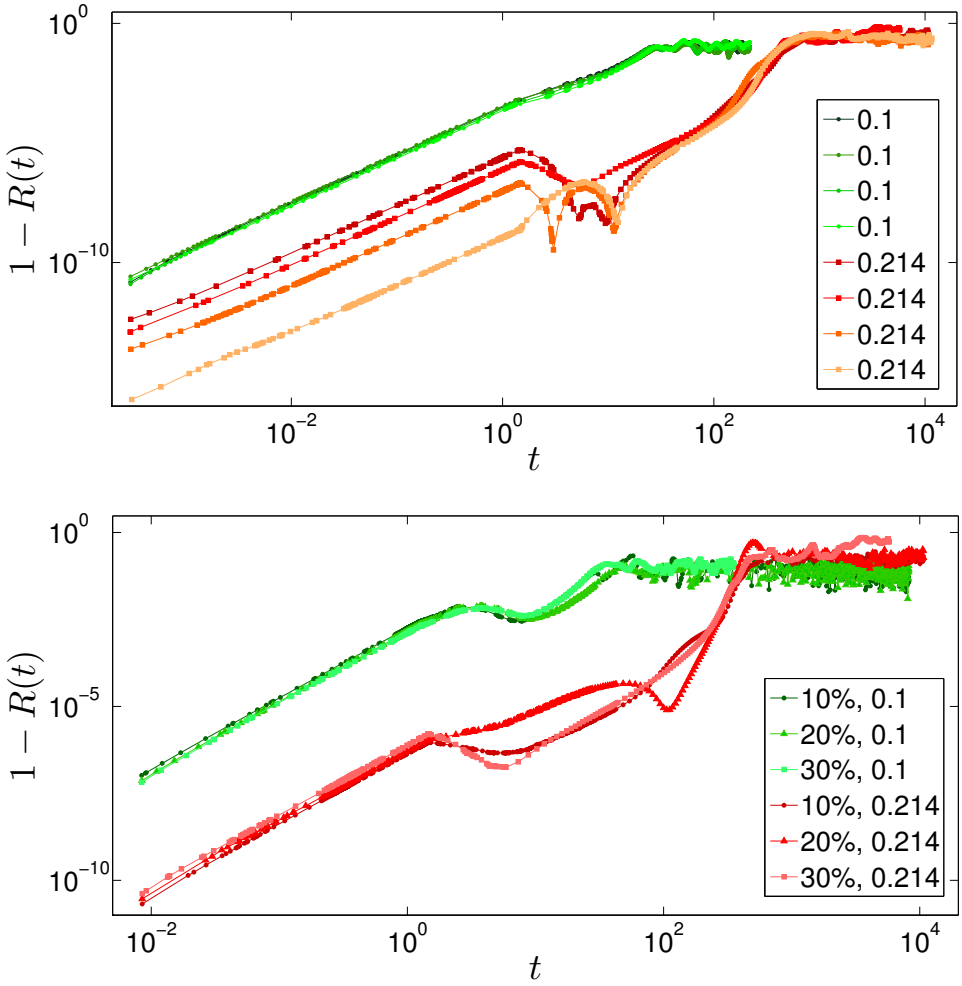

FIGURE 5.8: Response of the network to external stimuli applied at different times and with different intensity. In both figures, we plot the parameter $1 - R(t)$ of the stimulated nodes as a function of time and we consider networks with $M = 500$ and $\Delta = 250$. Green (red) shades data refer to $f_I = 0.1(0.214)$. Upper panel: for each network, we choose four different times to switch on a stimulus with the same intensity, i.e., on 30% of excitatory neurons, randomly chosen. All data are shifted so that the onset of the perturbation is at $t = 0$. Lower panel: we compare the transient dynamics for stimuli applied on 10%, 20%, and 30% of the excitatory neurons at $t = 0$. Image from [115].

General conclusions

In this work we have discussed the role of heterogeneity in the network connectivity and the cooperation between heterogeneity and inhibition in defining the synchronization transitions and the input processing capacity of neural networks. As a model of neural network, we have considered purely excitatory and excitatory/inhibitory networks with identical leaky integrate-and-fire neurons (LIF) with short term synaptic plasticity, where the input and the output connectivities are the same for each neuron. Indeed, especially for the hub nodes, that is nodes with a much larger number of connections than the average connectivity of the whole system, it is natural to expect a high connectivity both in the incoming and the outcoming links.

We have taken advantage of an efficient heterogeneous mean field (HMF) formulation of this model, which lets us speed up numerical computations and emphasize the role of connectivity. In this approach, the structural heterogeneity of the network is primarily encoded by the degree distribution $P(k)$ for the nodes.

In the purely excitatory case, network synchronization is analyzed as a function of the synaptic coupling strength. Fixing a Gaussian degree distribution, the network initial displays a quasisynchronous regime, where neurons with low degree are locked or periodic and neurons with high degree are unlocked, and a singular limit appears for very small and null synaptic couplings. As coupling increases, a synchronization phase transition occurs from this configuration to a totally asynchronous one, while increasing the Gaussian width, that is the connections heterogeneity, the network becomes less and less synchronizable. This can be somehow read as an evidence of the paradox of heterogeneity, initially proposed by Motter and colleagues [13] in totally different systems.

However, heterogeneity seems not to be the only determinant factor in driving networks synchronization, as clearly emerges in scale-free topologies (power law distributions). Similarly to what has been observed in the Gaussian case, with power law distributions the network still shows synchronization transitions as coupling increases. As a function of the exponent α of the distribution, which in literature has always been considered as the main parameter which influences the system properties, synchronization generally lowers, until for a given value of the exponent the system is everywhere asynchronous.

Nevertheless, the initial cutoff imposed on the distribution seems to play a fundamental role. Indeed, from our analyses, it turns out that in distributions with a single peak it is necessary to keep that peak well separate from $k = 0$. For the distributions which we have considered, this can be translated into a "Gaussian synchronization condition", which tells us that the distribution should be approximated with a sufficiently narrow Gaussian peak, in order to have synchronizable networks.

However, also this condition is not sufficient, as emerges when we discuss the complete phase diagram of synchronization transitions for distributions with a Gaussian peak and a power law tail. In this case, we can tune the exponent of the tail and its weight with respect to the Gaussian peak and we mainly classify synchronizable or not-synchronizable networks,

considering as synchronizable those networks which display a synchronization transition for a given critical value of the coupling. As we have verified, what allows us to better discriminate to which group a system belongs is the height of the Gaussian peak. Indeed, only distributions with a sufficiently high peak, namely which contain enough neurons with similar degrees, can synchronize. From one side, we need a bulk of neurons with homogeneous connectivity, represented by a well-defined peak; on the other side, synchronization properties do not substantially depend on the shape of the distribution at large connectivity, that is on the exponent of the power law tail. This can be expressed as a "homogeneity constraint", different from those which are usually applied to analyze distributions and in particular power law distributions. A better characterization of this constraint will be the subject of future works, where we plan to analyze the final phase diagram, reported in Fig. 4.9(b), also as a function of the standard deviation of the Gaussian peak.

In the second part of this work we have added inhibitory hub neurons to the network, to investigated the interplay between heterogeneity and inhibition in driving synchronization transitions, since some experimental evidences show that hub neurons are typically inhibitory and they are mostly responsible of the synchronous properties of the neural populations. In particular, we can control both the fraction f_I of inhibitory neurons present in the network and their hub character, quantified by their relative connectivity with respect to the rest of the network. Synchronization transitions are now discussed as a function of the inhibitory fraction, with a fixed the synaptic coupling.

Inhibitory hubs turn out to be strongly effective in driving the network synchronization: if their hub character is high, a small fraction of inhibitory neurons is able to increase network synchronization, starting from a quasisynchronous regime towards a total synchronization, where the frequency of all neurons is equal to that of the isolated LIF neuron, to asynchronous states if f_I further increases. Total synchronization is a consequence of a dynamical balance between excitation and inhibition, which actually is a widespread regime for neural ensembles of brain cortex. Note that, in this setup, we have also compared the results of the HMF formulation of the model with the dynamics of finite connectivity networks, showing that the mean field approximation reproduce correctly the system dynamics by increasing network connectivity, as expected, although this limit is not trivial, especially in the balance regime.

What clearly emerges in our networks is that the hub character of inhibitory neurons is a fundamental ingredient to allow a small fraction of inhibitory nodes to drive the synchronization of the overall network and in particular to produce a balance synchronous regime in correspondence of an inhibitory fraction equal to $10 - 30\%$, which is the experimentally observed range of values, almost constant in all species. Indeed, if these inhibitory neurons were not hubs, this highly synchronous states would appear only at too high inhibitory fraction, but as soon as the connectivity of the inhibitory component grows with respect to the excitatory one, the balance regime emerges for lower and lower inhibitory fractions.

Furthermore, around this regime of complete synchronization we have found an interesting metastable dynamical phase, where excitatory neurons are locked in clusters of different size, whose composition changes on very long time scales and it is dependent on initial conditions. Interestingly, this metastable dynamical regime is the most appropriate, with respect to all the other observe states, for storing information of an external input applied to the network. Although, this result depends on the nature of the model and on the specific distribution of network connections, it is an interesting prediction that might be tested experimentally.

In conclusion, future works will concern a further analysis of this model, where the correlation between the input and the output degree of each neurons is reduced or where inhibitory hubs are identified only by a high in- or out-degree.

Appendix A

A short introduction to graph theory and complex networks

Nowadays, graph theory and networks analyses play an extremely important role in dealing with problems and situations of our everyday life, as many relevant systems in nature, in technology and in social interactions are made by large numbers of densely interconnected dynamical units, producing very complex structures and phenomena. Besides neural networks, let's think for example to social networks, to the World Wide Web or to transportation networks. Modeling these highly complicated networks as graphs, whose nodes represent for instance neurons or individuals and whose links reproduce the interactions among them, is a very useful approach, which is largely used, since in many cases it provides a simple and tractable representation of the entire system.

Traditionally, the beginning of graph theory corresponds to the finding of the solution to the famous Königsberg bridge problem, published in 1736 by the Swiss mathematician Leonhard Euler, who found a way to cross all the bridges of that city, without passing twice through the same bridge. Since that first step, graph theory has been developed from the mathematical point of view and its concepts and results have been applied to study networks which belong to many different frameworks. Also social networks began to be analyzed in the 1920s with tools from graph theory and currently these tools are still largely used to examine for example communication patterns, information or diseases spreading in a group of people or trades and economic transactions in financial markets [32].

In particular, these social and financial networks, as well as the phone call networks, the transportation networks, Internet and the World Wide Web, the neural networks, the metabolic and protein networks, are called complex networks, because of their huge dimension (sometimes thousands or millions of highly interconnected dynamical nodes or coupled degrees of freedom), the complex dynamical processes which involve them and their highly irregular structures, which typically evolve in time [32]. The study of these complex networks has renewed the interest, mainly in the physicists community, in the research field of graph theory, thanks also to an increasing availability of computing resources and facilities, to the possibility of access to large databases of real networks and the development of powerful data analysis tools.

In such systems emergent collective behaviors of the whole system cannot be explained as a simply linear sum of the microscopic behavior of its single units. This concept can be expressed using the famous sentence of P.W. Anderson "More is different" [165]. Moreover, these systems are usually chaotic, that is their dynamics highly depends on the initial conditions: even small perturbations in the initial state produce totally different final states [25]. Also this concept can be summarized with a famous expression, the "butterfly effect". Neuronal ensembles, which are in our nervous tissues and in our brain, are paradigmatic examples of a complex system: although we know how a single neuron works, how the interaction among macroscopic groups of these cells gives rise to many different cognitive functions is still not clear.

In this Appendix, we briefly present some general definitions and basic concepts about networks and graph theory, focusing on what is most useful to read and understand the results presented in this thesis. In the last decades, many books and reviews have been published about these topics and complex networks in general. In particular, the main bibliographical references to which we were inspired in writing this Appendix are: [11, 32, 106, 166–169].

Graph theory is the branch of mathematics which concerns the study of networks. Each system which can be schematically represented as a graph, that is as a set of points (nodes or vertices) and of links (edges or lines) among them, is a network. A wide range of systems can be treated as a graph: the single units of the system will be the graph nodes, while the edges will symbolize the interactions among single elements [11].

In particular, also a neural ensemble can be represented as a network, whose nodes are the nerve cells and whose links correspond to the synapses among neurons. As we explain in Section 2.1, each electrical spike or action potential generated by the cell membrane is transmitted to another cell through a synapse. Since this synaptic transmission can travel only in one direction, a neural network is precisely a directed graph.

From a mathematical point of view, a directed (undirected) graph is denoted as $\mathcal{G} = (\mathcal{N}, \mathcal{L})$, where $\mathcal{N}$ and $\mathcal{L}$ are two non-empty countable sets: $\mathcal{N} = \{n_1, n_2, ..., n_N\}$ is the ordered list of graph nodes, generally identified by a numeric index, and $\mathcal{L} = \{l_1, l_2, ..., l_K\}$ is a list of ordered (unordered) pairs of elements of $\mathcal{N}$. The generic $k-$th element l_k of the links set can also be written as (i, j) or l_{ij}, where i and j form the couple of nodes connected by that link. N is the total number of nodes, while K is the total number of links. Although in graph theory the graph size is represented by K, in our physical context we will defined N as the network size.

A graph is directed (Fig. A.1(a)) if its links are oriented, so that the generic link l_{ij} starts from the $i-$th node and arrives to the $j-$th node and it can be crossed only in this direction. In the representation of this kind of graphs, links are actually arrows among couples of points and, in general, if a link exists from i to j, not necessarily also the inverse link from j to i exists. Otherwise, in an undirected graph (Fig. A.1(b)), links are not oriented and can be represented as solid lines.

In both cases of a directed or an undirected graph, if two nodes are connected by a link, we will say that they are adjacent or (nearest) neighbors and the set of all neighbors of a fixed node i will be called the neighborhood set $\mathcal{V}(i)$ of i.

The set of all links of a graph defines its topology and the most convenient way to describe it is through the adjacency matrix $\mathcal{A} = \{\epsilon_{ij}\}$, which is a $N \times N$ matrix with

$$\epsilon_{ij} = \begin{cases} 1, & \text{if } (i,j) \in \mathcal{L} \\ 0, & \text{if } (i,j) \notin \mathcal{L}. \end{cases} \tag{A.1}$$

The definition of an undirected graph implies that its adjacency matrix is symmetric, $\epsilon_{ij} = \epsilon_{ji}$, while in a directed graph the adjacency matrix is not symmetric.

The set of N eigenvalues $\{\mu_1, \mu_2, ..., \mu_N\}$ of the adjacency matrix $\mathcal{A}$ is the graph spectrum. This is a set of real numbers only if the graph is undirected and, as $Tr(\mathcal{A}) = 0$ (there are no self-links), the eigenvalues sum is 0. Many other less intuitive topological features and connectivity properties of the graph can be obtained looking at the matrix eigenvalues and the corresponding eigenvectors [32].

We can also define the Laplacian matrix as $\Lambda = \mathcal{D} - \mathcal{A}$, where D is the diagonal matrix with elements $D_{ii} = \sum_j \epsilon_{ij} = k_i$. For an undirected network, it is a symmetric positive semi-definite matrix and its eigenvalues $\{\lambda_1, \lambda_2, ..., \lambda_N\rangle$ are real and non-negative, corresponding to N orthogonal eigenvectors. In particular there always exists a null eigenvalue $\lambda_1 = 0$, which is the lowest one. As for the adjacency matrix spectrum, the eigenvalues and eigenvectors of Λ can give a direct characterization of the network. In Appendix C, we see how the stability

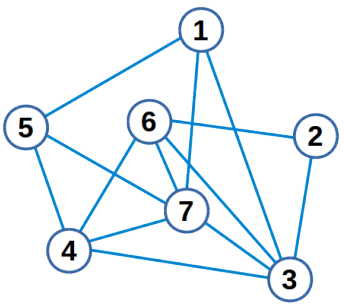

ϵ_{ij}	1	2	3	4	5	6	7
1	0	0	1	0	1	0	1
2	0	0	1	0	0	1	0
3	1	1	0	1	0	1	1
4	0	0	1	0	1	1	1
5	1	0	0	1	0	0	1
6	0	1	1	1	0	0	1
7	1	0	1	1	1	1	0

(a)

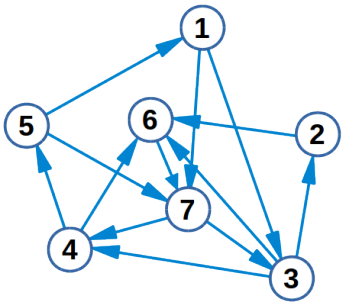

ϵ_{ij}	1	2	3	4	5	6	7
1	0	0	1	0	0	0	1
2	0	0	0	0	0	1	0
3	0	1	0	1	0	1	0
4	0	0	0	0	1	1	0
5	1	0	0	0	0	0	1
6	0	0	0	0	0	0	1
7	0	0	1	1	0	0	0

(b)

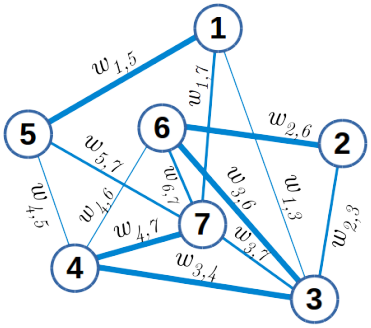

(c)

FIGURE A.1: (a) Undirected graph with $N = 7$ nodes, labelled with increasing integers, and $K = 13$ links, represented as solid lines. This graph does not contain loops or self-links, i.e. links from a node to itself, nor multiple links, i.e. nodes pairs connected by more than one link. Graphs with these non standard structures are called multigraphs. Below the graph, its corresponding (symmetric) adjacency matrix is reported. (b) Directed graph with the same number of nodes and links and its corresponding (non symmetric) adjacency matrix. The edges now are represented as arrows, since they correspond to directional connections. (c) Weighted (undirected) graph with the same number of nodes and links (solid line without arrows). The value $w_{i,j}$ reported on each edge denotes the weight of the corresponding connection, graphically represented by the line thicknesses.

of synchronization of linearly coupled oscillators is related to the Laplacian eigenvalues and more precisely to the ratio λ_N/λ_2.

Besides the directed and the undirected graphs, there exists a third kind of networks with a more heterogeneous nature: the weighted networks [170] (Fig. A.1(b)). In these networks, each link can be more or less strong and it is characterized by a numerical value to measure this connection intensity. A real social network is an example of a weighted network, because typically we cannot simply say to have or not have a friend, but among our friends we have more strong relationships with someone than with others. Other examples of weighted networks are the predator-prey interactions in food webs, data traffic on Internet or passengers flights in airline networks. A weighted graph $\mathcal{G}^W$ is defined by three sets, that is $\mathcal{G}^W = (\mathcal{N}, \mathcal{L}, \mathcal{W})$, where $\mathcal{N}$ and $\mathcal{L}$ are the same of the directed and the undirected networks and $\mathcal{W} = \{w1, w2, ..., w_K\}$ is a new set of real positive values which represent the weights associated to all links. Besides the adjacency matrix, a weighted graph needs a second $N \times N$ matrix, whose entry w_{ij} is the weight of the link connecting node i to node j ($w_{ij} = 0$ if there is no link, $w_{ij} > 0$ if $\epsilon_{ij} = 1$). For undirected (directed) weighted graphs, weights are symmetric (asymmetric), that is $w_{ij} = (\neq) w_{ji}$. Other quantities useful to characterize this networks are the weight distribution $Q(w)$, which defines the probability that a link has weight w, and the node strength s_i or node weight, which is a sum of the weights of all links incident on node i:

$$s_i = \sum_{j=1}^{N} w_{ij}. \tag{A.2}$$

Since we do not consider our neural networks as weighted graphs, we do not go further in discussing definitions and properties of these kind of networks; a more complete description of weighted networks can be found in [11, 32, 170].

Coming back to consider unweighted networks, we need to define some other concepts, which are useful to describe networks.

Connectivity. Regarding the total number of nodes and edges, we will say that a network is sparse if $K \ll N^2$ or more generally if $K \sim N^\alpha$, with $\alpha < 2$ (the adjacency matrix of such a graph will be also sparse), and dense if $K = \mathcal{O}(N^2)$.

In an undirected network, we get a complete $N-$graph if $K = \binom{N}{2} = N(N-1)/2$, which is the maximum number of edges allowed in a network of N nodes. As in a complete graph each node is connected with all the others, this is also called all-to-all or fully connected network. On the other hand, the minimum number of necessary links to build a connected graph, that is a graph with no disconnected parts, is $N-1$.

In a directed network the total number of edges K can range from $N-1$ to $N(N-1)$. In general, in order to compare the level of sparseness or connectance of two different networks, we need to define the graph density $\mathcal{D}$ as the number of existing edges divided by the maximum possible number, $\mathcal{D} = K/[N(N-1)/2]$.

Paths and distances. We can analyze the connectivity of a graph also defining some quantities linked to the paths among nodes.

The path $\mathcal{P}_{i_a,i_b}$ which connects the nodes i_a and i_b on a graph $\mathcal{G} = (\mathcal{N}, \mathcal{L})$ is an ordered set of nodes $\{i_a, i_{a+1}, ..., i_b\}$ and edges $\{(i_a, i_{a+1}), (i_{a+1}, i_{a+2}), ..., (i_{b-1}, i_b)\}$, such that $i_\alpha \in \mathcal{N}$ and $(i_{\alpha-1}, i_\alpha) \in \mathcal{L}$, for all $\alpha \in [a, b]$. The length of this path $\mathcal{P}_{i_a,i_b}$ is $b-a$. In particular, if $i_a = i_b$ and all the other nodes and edges are distinct, the path becomes a loop or a cycle. Using this concept of paths, we can now better define the connected graph, above mentioned: if randomly chosen two vertices of the graph there exists a path connecting them, the graph will be said connected.

Although a graph is described by its topology, without introducing any metric, we can define the distance between two nodes as the shortest path length: among all the possible paths $\mathcal{P}_{i,j}$ to go from node i to node j and all their lengths, the minimum length is called shortest path length ℓ_{ij} between nodes i and j. Because of its symmetric properties, in a undirected graph also the shortest path length is symmetric, that is $\ell_{ij} = \ell_{ji}$, but in general this is not true in a directed graph. In both cases, the maximum value of the shortest path length computed over all the possible pairs of nodes, that is

$$d_{\mathcal{G}} = \max_{i,j} \ \ell_{ij} \tag{A.3}$$

is called diameter of the network. The average value over all the ℓ_{ij}, called average shortest path length or characteristic path length, is

$$\langle \ell \rangle = \frac{1}{N(N-1)} \sum_{i,j=1}^{N} \ \ell_{ij}. \tag{A.4}$$

The two previous definitions imply that $\langle \ell \rangle \leq d_{\mathcal{G}}$.

Embedding a graph with a metric definition requires that all its nodes occupy a precise position in a $d-$dimensional Euclidean space and therefore, as in the real space, all links becomes physical connections, whose length really represents the distance between nodes. These graphs are called spatial networks. Typical examples of spatial networks are communication

networks, electric power grids, transportation systems on airport, street or railway networks [32]. In such networks, we need to define the spatial distribution of the nodes, taking into account any geographical constraints of the considered physical space: this could yield a fractal spacing for those networks which continuously evolve in a limited space, as power grids, or limit the number of links connected to a single node, as in street networks. Moreover, due to the cost of edges, the more distant two nodes are, the less likely they will be connected. As the weighted networks, since we do not consider our neural ensembles as spatial networks, here we do not describe them in details. An exhaustive review on these networks can be found in [171].

Centrality. To measure the importance of a node in a directed graph, let's say the importance of an individual in a social network, we can compute its centrality parameter using different centrality definitions, depending on what we are interested in the most. For example, the closeness centrality

$$c_i = \frac{1}{\sum_{i,j=1;i\neq j}^{N} \ell_{ij}} \tag{A.5}$$

is a sort of average distance of node i to all the others, so that a node characterized by short distances has a high closeness centrality. The betweenness centrality can also be used and it is defined as follows:

$$b_i = \sum_{i\neq j\neq k} \frac{n_{jk}(i)}{n_{jk}}, \tag{A.6}$$

where n_{jk} is the number of shortest paths connecting j and k, while $n_{jk}(i)$ is the number of shortest paths connecting j and k and passing through i. Both definitions imply that the more a node belongs to shortest paths, the more central it is.

Node degree. One of the most relevant properties of the single node in our networks is its degree and the degree distribution. In a undirected graph, the degree k_i of a node i corresponds to the number of links incident on it. In a directed graph, we need to distinguish between the input degree or in-degree $k_{in,i}$ of node i, which is the number of links entering i, and the output degree or out-degree $k_{out,i}$, which is the number of links exiting from i. The total degree k_i will be then determined as the sum of the input and output degrees, $k_i = k_{in,i} + k_{out,i}$. Considering the adjacency matrix of this directed graph, we can also give the following definitions:

$$k_{in,i} = \sum_{j=1}^{N} \epsilon_{ji}; \quad k_{out,i} = \sum_{j=1}^{N} \epsilon_{ij}. \tag{A.7}$$

If we consider large-scale networks, the individual measure of the node degree in that graph becomes useless to analyze global properties, but we need to consider some statistical measures on the whole system. Therefore we define the degree distribution $P(k)$: in undirected graphs it is a probability density distribution, which gives the probability that any randomly chosen node has degree k. For directed graphs we typically have two distributions, the in-degree or input distribution $P(k_{in})$ and out-degree or output distribution $P(k_{out})$, defined as the probability that a randomly chosen node has in-degree k_{in} and out-degree k_{out}, respectively. Given

these distributions, the average network degree is computed as

$$\langle k \rangle = \frac{1}{N} \sum_{i=1}^{N} k_i = \sum_k k P(k) = \frac{2K}{N} \tag{A.8}$$

$$\langle k_{in} \rangle = \sum_{k_{in}} k_{in} P(k_{in}) = \frac{\langle k \rangle}{2} \tag{A.9}$$

$$\langle k_{out} \rangle = \sum_{k_{out}} k_{out} P(k_{out}) = \frac{\langle k \rangle}{2}. \tag{A.10}$$

In a directed network, the average in-degree has to be equal to the average out-degree, as a link departing from any node must arrive at another node. While in general the average degree is the first moment of the distribution $P(k)$, the generic $n-$th moment can be written as

$$\langle k^n \rangle = \sum_k k^n P(k) \xrightarrow[N \to \infty]{} \int k^n P(k)\, dk. \tag{A.11}$$

Note that the second moment measures the fluctuations of the connectivity distribution.

Many real networks are correlated systems, where the probability that a node of degree k is connected to another node of degree k' depends on k. For these correlated systems, besides the degree distribution $P(k)$, a conditional probability $P(k'|k)$ has to be defined, which satisfies the normalization $\sum_{k'} P(k'|k) = 1$ and the degree detailed balance condition $kP(k'|k)P(k) = k'P(k|k')P(k')$. Starting from the definition of the average degree of nearest neighbors of a node i, that is

$$k_{nn,i} = \frac{1}{k_i} \sum_{j \in \mathcal{V}(i)} k_j = \frac{1}{k_i} \sum_{j=1}^{N} a_{ij} k_j, \tag{A.12}$$

where the first sum runs on the nodes belonging to neighborhood $\mathcal{V}(i)$ of node i, one can also introduce the average degree of the nearest neighbors of nodes with degree k, denoted as $k_{nn}(k)$, in terms of the conditional probability:

$$k_{nn}(k) = \sum_{k'} k' P(k'|k). \tag{A.13}$$

In a correlated network, $k_{nn}(k)$ can be either an increasing or a decreasing function of k: in the first case the graph is assortative and nodes are mostly connected to those with similar degrees, while in the second case the graph is disassortative and nodes with low degree are more likely connected with highly connected ones. The most used measure of the degree correlation in a graph is the slope value ν of $k_{nn}(k)$ as a function of k, as reported in Table A.1. In an uncorrelated network we expect that $k_{nn}(k)$ is independent of k and it can be easily proved that $k_{nn}(k) = \langle k^2 \rangle / \langle k \rangle$. Indeed, in this case the functional form of $P(k'|k)$ is written as a function of the probability that a link is connected to a node of degree k'. This is simply the total number of edges departing from all nodes of degree k' (if there are $N_{k'}$ nodes with degree k', this number will be $k'N_{k'}$) divided by the number of all edges departing from nodes of any degree:

$$P_{unc}(k'|k) = \frac{k' N_{k'}}{\sum_{k''} k'' N_{k''}} = \frac{k'}{\frac{\sum_{k''} k'' N_{k''}}{N}} \cdot \frac{N_{k'}}{N} = \frac{k'}{\langle k \rangle} P(k'), \tag{A.14}$$

where we set a uniform probability $P(k') = N_{k'}/N$. This correlated probability implies that a randomly chosen link is more likely connected to a node with large degree, which is trivial if you think that the more connected you are, the easier it is to find you. Then, replacing the

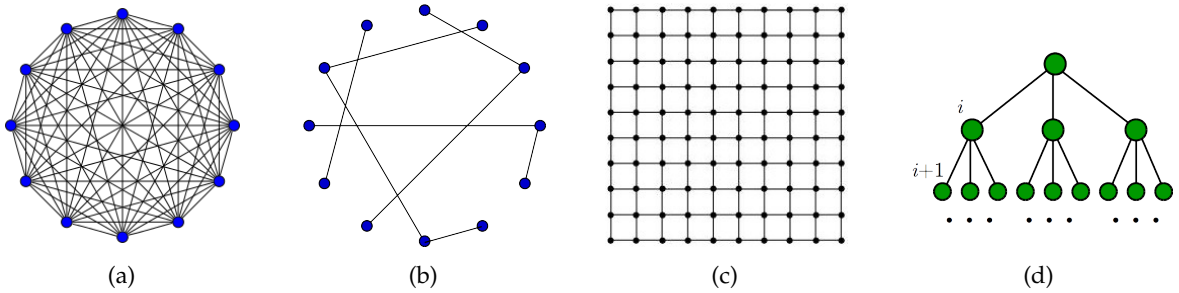

FIGURE A.2: (a) All-to-all or complete undirected graph: each node is connected to all other nodes. (b) A sparse undirected graph: compared to the previous graph, quite less links are present. (c) A regular $2D$ graph or lattice network: each node has a fixed number $d = 4$ of nearest neighbors. (d) A hierarchical graph: each node of the $i-$th order is the child of the $(i-1)-$th order and the parent of the $(i+1)-$th order.

distribution Eq. (A.14) in Eq. (A.13), one gets the final expression for the uncorrelated average degree $k_{nn}(k)$.

Clustering in undirected networks. Once defined the node degree, the clustering coefficient $C(i)$ of node i gives a quantitative measure of the cohesiveness of the neighborhood of i and it is usually defined as the ratio of the number of links between the neighbors of i and the maximum possible number of such links:

$$C(i) = \frac{e_i}{k_i(k_i-1)/2}, \tag{A.15}$$

where e_i is the numbers of existing links among the k_i (degree of i) neighboring nodes of i. If $k_i = 1$, $C(i)$ is set to 0, which is its minimum value, while the maximum one is 1. If we compute the clustering coefficient $C(i)$ of all nodes of the graph, then we can measure the average clustering coefficient as

$$\langle C \rangle = \frac{1}{N}\sum_{i=1}^{N} C(i). \tag{A.16}$$

Let's consider now some simple examples of undirected networks. In an all-to-all graph (Fig. A.2(a)) of size N, each node has degree $k_i = N-1$ and maximum clustering coefficient $C(i) = 1$, therefore the average degree scales as $\langle k \rangle \sim N$, the average shortest path length $\langle \ell \rangle$ and the average clustering coefficient are both 1. On the contrary, in a sparse graph (Fig. A.2(b)), all the degrees are almost null or very small, as the average clustering coefficient, and the average degree is much smaller than the size N. However, the average shortest path length could diverge, since for definition $l_{ij} \to \infty$ if nodes i and j are not connected. In a regular hypercubic lattice (Fig. A.2(c)) in D dimensions with N nodes, all nodes have the same number of nearest neighbors and, due to the graph regularity, the same clustering coefficient, while the average shortest path length scales as $\langle \ell \rangle \sim N^{1/D}$. Another interesting type of undirected networks is the hierarchical graph (Fig. A.2(d)), where each node (child) is linked to only one node of the previous order (parent), as if it was originated by that parent, except for the initial root node, from which the graph starts. Because of its peculiar structure, this graph is also called (rooted) tree. In such a network, in general we can state that N is equal to $K+1$. The shortest path length is constant, if we choose any pair of nodes, one belonging to order i and one to order j, and it increases as we go down in the tree structure.

Moving to more complex networks, recent results and measures of path length, clustering coefficient and other quantities have proved that real networks belonging to different contexts show similar topological features, such as small characteristic path length, high clustering coefficient, degree distribution with tails and degree correlations. Some of these measures are reported in Table A.1.

In the following we briefly describe the three main and most common models of networks: random graphs, small-world networks and scale-free networks.

Network	N	$\langle k \rangle$	$\langle \ell \rangle$	$\langle C \rangle$	α	ν
AS2001	11174	4.19	3.62	0.24	2.38	< 0
Routers	228263	2.80	9.5	0.03	2.18	> 0
WWW	$\sim 2 \times 10^8$	7.5	16	0.11	2.1/2.7	unknown
Protein	2115	6.80	2.12	0.07	2.4	< 0
Metabolic	778	3.2	7.40	0.7	2.2/2.1	< 0
Math1999	57516	5.00	8.46	0.15	2.47	> 0
Actors	225226	61	3.65	0.79	2.3	> 0
E-mail	59812	2.88	4.95	0.03	1.5/2.0	unknown

TABLE A.1: Properties of some real networks. The measured quantities are: number of nodes N, average degree $\langle k \rangle$, characteristic path length $\langle \ell \rangle$, clustering coefficient $\langle C \rangle$, exponent of the degree distribution α and type of correlation ν . All networks, except the WWW, metabolic (Escherichia coli) and e-mail networks, are undirected; for the directed networks the two values for α are the in/out-degree exponents, respectively. The first example (AS2001) represents the Internet network as autonomous system (AS) in 2001 (the nodes are the hosts and the links are the physical connections among them). The second network represents the Internet network at the routers level. The third example refers to the the World Wide Web as a network formed by the hyperlinks among Web pages. The fourth and the fifth networks represents the protein-protein interaction network in the yeast (its nodes are proteins and they are linked if the corresponding proteins physically interact) and a network of metabolic reactions (its nodes are chemicals, connected to each other through the existence of metabolic reactions). The last three rows refer to social networks: the collaborations graph of mathematicians defined by paper co-authorships, the movie actors collaboration network and a network of e-mail exchanges. Table adapted from [32].

Random graphs. One of the most used graph models, which has been systematically analyzed, is the random graph, where "random" means that links are randomly distributed among nodes. This model was first proposed by Erdös and Rényi in 1959. The Erdös-Rényi (ER) model correspond to a static uncorrelated and undirected random graph, denoted as $\mathcal{G}^{ER}_{N,K}$, where N is the (fixed) graph size, K the number of links and the probability that two vertices are connected is equal to p. In its original formulation, this graph is built starting from N disconnected nodes and then adding links between randomly chosen pairs, avoiding multiple connections, until the number of edges is equal to K [172]. According to this procedure, many topologically different but statistically equivalent graphs can finally be obtained, so that it would be more rigorous to describe the entire statistical ensemble of all possible realizations. Otherwise, one could draw the ER graph without the constraint of fixed number of links, but connecting each

couple of nodes with a probability $0 < p < 1$. In this case the graph will be denoted as $\mathcal{G}^{ER}_{N,p}$. Clearly, $\mathcal{G}^{ER}_{N,K} \approx \mathcal{G}^{ER}_{N,p}$ in the thermodynamic limit $N \to \infty$, where $\langle k \rangle$ is kept fixed.

Erdös and Rényi proved that the connectivity of these graphs and, in particular, the size of the largest connected component displays a second order phase transition as a function of p:

- if $p < p_c = \frac{1}{N}$, then the graph has no connected component of size greater than $\mathcal{O}(\ln N)$;
- if $p = p_c$, then the largest connected component has size $\mathcal{O}(N^{2/3})$;
- if $p > p_c$, the graph has a connected component of size $\mathcal{O}(N)$ and no other component has a size greater than $\mathcal{O}(\ln N)$.

In particular, if $p \geq lnN/N$, the graph is almost totally connected and both the diameter d_G and the average shortest path length $\langle \ell \rangle$ can be written as a function of N as $\ln N / \ln(pN) = \ln N / \ln\langle k \rangle$. The clustering coefficient is equal to $C = p = \langle k \rangle / N$ and it tends to zero in the limit of $N \to \infty$.

Finally, to write the degree distribution $P(k)$ of ER networks, we first note that the probability for a node i to be connected to other k nodes is the binomial distribution $P(k) = \binom{N-1}{k} p^k (1-p)^{N-1-k}$. Now, since all nodes in a random graph are statistically equivalent, the probability that a randomly chosen node has degree k is the same for all nodes, equal to the previous binomial probability $P(k)$. Therefore, for $N \to \infty$ and $\langle k \rangle = const$, the degree distribution tends to a Poisson distribution:

$$P(k) = e^{-\langle k \rangle} \frac{\langle k \rangle^k}{k!} \tag{A.17}$$

Although ER graphs have been largely studied, they rarely can be applied to real networks, unless one considers to extend them, for example embedding in the graph different degree distributions. Random graphs with an arbitrary degree distribution $P(k)$, also called generalized random graphs, can be obtained following the configuration model introduced by Bender and Canfield in 1978 [173]. According to this procedure, given the N nodes of am undirected graph, a degree sequence, that is a list of N integer numbers $D = \{k_1, k_2, ..., k_N\}$, sets the degree of each node (k_i is the degree of node i), such that $\sum_{i=1}^{N} k_i = 2K$ and the fraction of nodes with degree equal to k will tend to $P(k)$, in the limit of large N. Then, the graph is built choosing randomly, with uniform probability, couples of nodes, which will be connected by a link. Some constraints have to be kept: multiple links and self-links are not allowed and for each node i we must allocate a number of connections towards other nodes equal to $k_i/2$, so that at the end of the procedure all nodes will have a number of connections exactly equal to their assigned degree k_i. As seen above, many topologically different networks can be obtained following this method, since each configuration can be obtained in $\prod_{i=1}^{N}(k_i!)$ different ways, where $k_i!$ are the permutations of the k_i links of node i. Defining $\mathcal{G}^{conf}_{N,D}$ as the ensemble of all graphs with N nodes and degree sequence D, all these graphs are statistically equivalent [174, 175].

Concerning in particular our work, this configuration model assumes a quite important role, since we have exactly followed this procedure to built our neural networks with finite connectivity, as explained in Section 3.4.

Small-world networks. As we show in Table A.1, many real networks are characterized by relatively small average path length $\langle \ell \rangle$, as random graphs, and high clustering coefficient $\langle C \rangle$, as regular lattices. Such networks belong to the class of the so-called small-world networks $\mathcal{G}^{WS}_{N,K}$. They were rigorously described for the first time in 1998 by Watts and Strogatz [176], who also proposed a method to build them, the Watts and Strogatz or WS model. According to this model, a small-world graph can be obtain starting from a regular ring-like lattice, that is a graph whose N nodes lie on a ring and are symmetrically connected to its $2m$ nearest

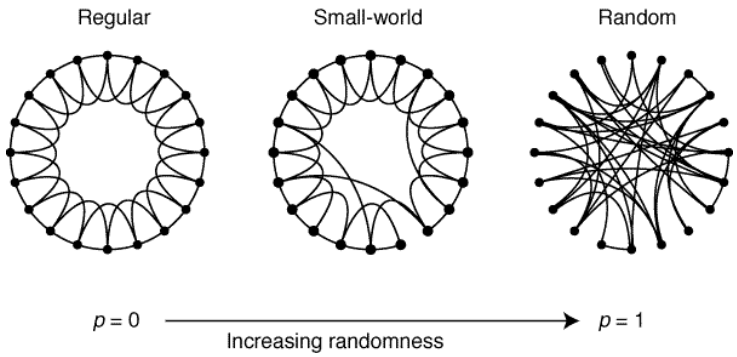

FIGURE A.3: Representation of Watts and Strogatz random rewiring procedure for obtaining a small-world graph starting from a regular ring lattice, without changing the number of nodes or links in the graph. We start with a ring of $N = 20$ nodes, each connected to its $k = 4$ nearest neighbors by undirected edges. Then, we choose a node and one of its edge: with probability p we reconnect this edge to a new randomly chosen node (multiples links are forbidden) and with probability $1 - p$ we do not modify it. We repeat this process by moving clockwise around the ring, until each node and each link has been considered once. If $p = 0$, the original regular ring is unchanged; as p increases, the graph becomes increasingly disordered (small-world graph), until for $p = 1$, all edges are rewired randomly and a totally random graph is obtained. Image from [176].

neighbors. In such a network, each "regular" link is rewired to a new randomly chosen node with probability p, as shown in Fig. A.3. As a function of the rewiring probability p, for small value of p the characteristic path length $\langle \ell(p) \rangle$ significantly decreases, since the rewiring of links creates many new shortcuts links among nodes, while the average clustering coefficient $\langle C(p) \rangle$ is weakly influenced by the rewiring procedure. Actually, in this region of small values of p, characterized by both small $\langle \ell(p) \rangle$ and high $\langle C(p) \rangle$ (see Fig. A.4), we have a small-world network.

Thanks to numerical and analytical results, it has been proved that the small-world transition is a continuous phase transition, which occurs when the density of shortcuts tends to zero with a characteristic length diverging as p^{-1}.

Finally, it is simple to show that for $p = 0$ the degree distribution $P(k)$ is equal to the distribution of a regular lattice, which is a Dirac δ function centered at $k = 2m$, while for $p = 1$ it tends to be the ER distribution. For intermediate p, the degree distribution can be written as [32]

$$P(k) = \begin{cases} 0, & \text{if } k < m \\ \sum_{i-0}^{min(k-m,m)} \binom{m}{i} (1-p)^i \, p^{m-i} \, \frac{(pm)^{k-m-i}}{(k-m-i)!} \, e^{-pm}, & \text{if } k \geq m, \end{cases} \tag{A.18}$$

In this case, the model generates graphs with the small-world property and a non-trivial clustering coefficient.

Scale-free networks. The last class of networks we present are the scale-free networks, which are in particular considered in Section 4.3. Besides the small-world property shown in the previous paragraph, a wide variety of real networks are represented by graphs with power law degree distributions. Such networks can be seen as special cases of generalized random graphs with a power law degree distribution:

$$P(k) = \begin{cases} 0, & \text{if } k < k_{min} \\ \mathbb{N} k^{-\alpha}, & \text{if } k \geq k_{min}, \end{cases} \tag{A.19}$$

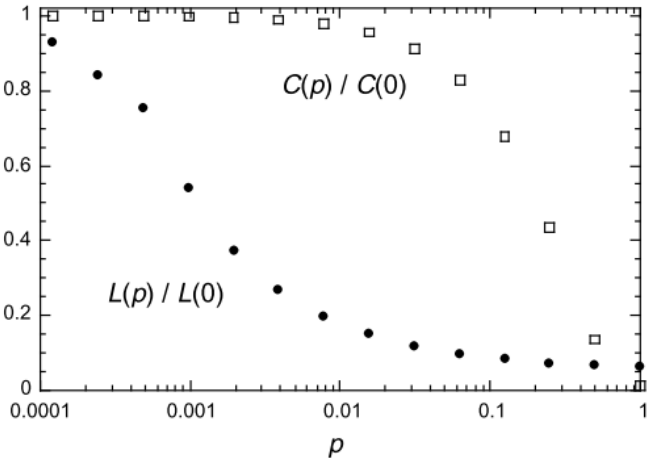

FIGURE A.4: Characteristic path length $L(p)$ and clustering coefficient $C(p)$ normalized by the values $L(0)$ and $C(0)$ of the regular lattice for randomly rewired graphs, as a function of the rewiring probability p (logarithmic horizontal scale). All the graphs have $N = 1000$ nodes and an average degree of $\langle k \rangle = 10$. The initial interval of p, for which $L(p)$ decreases, while $C(p)$ remains almost constants, corresponds to the small-world phenomenon: here, we have graphs with small characteristic path lengths, as for random graphs, and relatively high clustering coefficient, as for regular graphs. Image from [176].

where $\alpha > 0$, $\mathbb{N}$ is the normalization constant and the condition $k = k_{min} > 0$ is the lowest possible degree in the network, necessarily to remove the divergence in zero. These networks are typically called (static) scale-free networks, because of the scale invariance of their degree distributions with respect to a variable rescaling: indeed, if we applied a coarse graining procedure defining a new variable $k \to \lambda k$, where λ is a magnification/reduction factor, the distribution would still appear as a power law, only multiplied by a constant factor. This property is also known as self-similarity and it implies that the distribution always looks the same at all length scales.

The clustering coefficient of scale-free networks has been first computed by Newman [168], giving the following result:

$$\langle C \rangle \sim N^{-\frac{3\alpha-7}{\alpha-1}}. \tag{A.20}$$

If $\alpha > 7/3$, $\langle C \rangle$ decreases as N grows. At $\alpha = 7/3$, $\langle C \rangle$ remain constant, while for $\alpha < 7/3$ it increases with the size. Concerning the average path length $\langle \ell \rangle$, it scales as $\log N$ if $\alpha > 3$ and as $\mathcal{O}(\log \log N)$ if $2 < \alpha < 3$.

Due to the power law distribution, scale-free graphs are characterized by a high level of heterogeneity in the topology, since many nodes will have low degree and only few of them, called hubs, will have a very high degree. In many real networks, the presence of these hub nodes is actually a consequence of some optimization factors. Here, in order to give a heuristic measure of heterogeneity of the network, we need to compute the first two moments of the distribution. We consider for simplicity k as a continuous variable, so that the distribution moments can be written as integrals and the final result can be explicitly computed:

$$\langle k \rangle = \int_{k_{min}}^{\infty} kP(k)\, dk = \mathbb{N} \int_{k_{min}}^{\infty} k^{1-\alpha}\, dk \tag{A.21}$$

$$\langle k^2 \rangle = \int_{k_{min}}^{\infty} k^2 P(k)\, dk = \mathbb{N} \int_{k_{min}}^{\infty} k^{2-\alpha}\, dk. \tag{A.22}$$

The first moment is the average value and the second moment is necessary to compute the

variance $\sigma^2 = \langle k^2 \rangle - \langle k \rangle^2$ or the normalized variance $\sigma^2 / \langle k \rangle^2$, which measures the statistical fluctuations present in our system. Analogous expressions can be written in the discrete case, where the integrals are replaced with discrete sums. Since the previous functions are analytically integrable, we get

$$\langle k \rangle = \frac{\mathbb{N}\, k_{min}^{2-\alpha}}{\alpha - 2} \text{ for } \alpha > 2 \tag{A.23}$$

$$\langle k^2 \rangle = \frac{\mathbb{N}\, k_{min}^{3-\alpha}}{\alpha - 3} \text{ for } \alpha > 3. \tag{A.24}$$

The first result converges only for $\alpha > 2$, while the second one for $\alpha > 3$. This implies that in the interval $2 < \alpha \leq 3$, to which most of the computed power law exponents for real networks belong (see Table A.1), the average degree is well defined and bounded, but the variance diverges, that is degree fluctuations depend on the network size. In that case $\langle k \rangle$ cannot be considered a characteristic scale for the system. For $\alpha > 2$ the level of heterogeneity of networks are described by the parameter

$$\kappa = k_{min} \frac{\alpha - 2}{\alpha - 3}. \tag{A.25}$$

In scale-free (heterogeneous) networks, κ is typically much larger than $\langle k \rangle$, while in homogeneous networks $\kappa \sim \langle k \rangle$. For uncorrelated networks, looking at Eq. (A.13) it follows that $\kappa = k_{nn}(k)$.

Since many real networks seem to self-organize in order to create scale-free topologies during their temporal evolution, we now need to take into account a class of model which can explain how these power law distributions arise from growing procedures or aging processes. In this framework, the first model of network growth was proposed by Barabási and Albert in 1999 and it is therefore called Barabási-Albert (BA) model [177]. While the previous models are based on a fixed network size N, here we assume to have an growing system, where new nodes and links are continuously added. Such a network is also called evolving network. This is what actually occurs in real networks, as for example in a social network or in the World Wide Web. In addition to their possibility to grow, another natural property of evolving real networks is that a node with a high degree typically acquires new links faster than small nodes (this is the so-called "rich-gets-richer" or preferential attachment phenomenon). Both growth and preferential attachment are included in the undirected BA graph $\mathcal{G}_{N,K}^{BA}$, which is built as follows:

1. It starts with m_0 isolated nodes.

2. At each time step $t = 1, 2, ..., N - m_0$ a new node with a given degree $m \leq m_0$ is added and all its links to m previously existing nodes are drawn. At time t we expect to have $N = m_0 + t$ nodes and $K = mt$ links.

3. The probability that a link will connect a node j to a node i is linearly proportional to the actual degree of i, or $p_{j \to i} = k_i / \sum_l k_l$ (preferential attachment)

This procedure is represented in Fig. A.5.

Solving this model in the mean-field approximation [178] and in the limit of $t \to \infty$, the resulting degree distribution is $P(k) \sim k^{-\alpha}$, where the exponent α is independent of m and equal to 3 (see Fig. A.6). Moreover, $P(k)$ is independent of time and consequently of the network size N, as if the system actually self-organized into a scale-free stationary state during throughout its growth.

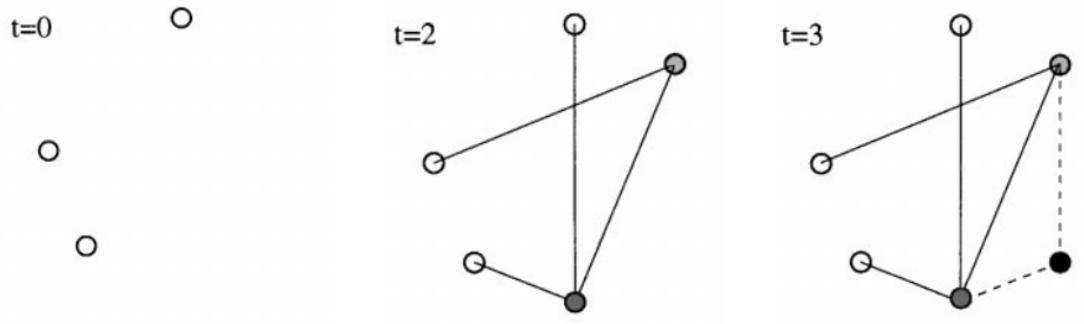

FIGURE A.5: Representation of the Barabási-Albert model with $m_0 = 3$ and $m = 2$. (a) At $t = 0$ there are $m_0 = 3$ isolated nodes. At each time, a new node with $m = 2$ new links is added. Each new node preferentially attaches to those vertices with higher connectivity. (b) At $t = 2$ there are $m_0 + t = 5$ nodes and $mt = 4$ links. (c) At $t = 3$ the sixth vertex is added and its two new edges are represented by dashed lines. Images from [178].

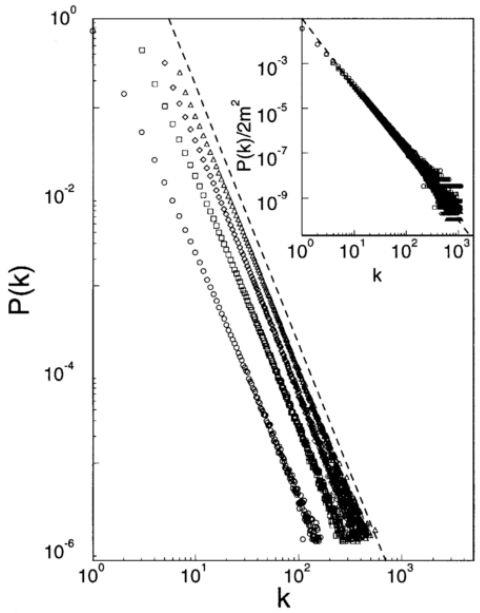

FIGURE A.6: Degree distribution $P(k)$ of the BA model, with $N = m_0 + t = 300000$ nodes and $m_0 = m = 1$ (circles), $m_0 = m = 3$ (squares), $m_0 = m = 5$ (diamonds) and $m_0 = m = 7$ (triangles). The slope of the dashed line is $\alpha = 2.9$. The inset shows a rescaled distribution $P(k)/2m^2$ for the same values of m and the slope of the dashed line is $\alpha = 3$, proving that the final degree distribution does not depend on m. Image from [178].

Finally, the analytic expressions for the average clustering coefficient and for the average shortest path length can be written as [11]

$$\langle C \rangle = \frac{m}{8N} (\ln N)^2 \tag{A.26}$$

$$\langle \ell \rangle \sim \frac{\log N}{\log \log N}. \tag{A.27}$$

The first result implies that the clustering coefficient decays slower than in an ER random graph and than in a small-world graph (where $\langle C \rangle$ is a constant), while the last result implies that the average distance in the BA model is smaller than in a ER random graph with same N and K.

After the first works of Barabási and Albert [177], many variants and generalizations of the BA scale-free networks [166] have subsequently appeared in literature, as models with different preferential attachment procedures, with dynamic rewiring, fitness models, hierarchically and deterministically growing models, extensions to directed scale-free graphs or alternative methods to generate degree correlations.

Appendix B

Master stability function approach

This Appendix is an extension of Section 1.5 and concerns the *master stability function* [11, 30, 32, 117] approach for analyzing the stability of synchronization states in systems of N coupled oscillators.

Starting from Eq. (1.16) and its the global synchronization solution, $\phi_i(t) = s(t),\ \forall i$, with $\dot{s}(t) = F(s)$, we consider a small perturbation $\phi_i = s+\xi_i$ with $\xi_i \ll s$ and its time derivative $\dot{\phi}_i = F(s) + \dot{\xi}_i$. If after this perturbation the system is able to come back to the original synchronous state and ξ_i decreases, then the synchronized solution is stable. Applying this perturbation also to $F(\phi_i)$ and to $q(\phi_j)$ in Eq. (1.16), we get respectively $F(\phi_i) \approx F(s) + \xi_i F'(s)$ and $q(\phi_j) \approx q(s) + \xi_j q'(s)$, where $F'(s)$ and $q'(s)$ are the derivatives with respect to s. Now, if we replace all the terms of Eq. (1.16) with their perturbed expressions, we obtain the following equation for the perturbations $\xi_i(t)$

$$\dot{\xi}_i(t) = \xi_i F'(s) + g \sum_{j=1}^{N} L_{ij} q'(s) \xi_j, \tag{B.1}$$

which can be decoupled, computing the eigenvalues λ_i ($i = 1, ..., N$) of the Laplacian matrix and its eigenvectors ζ_i, as follows:

$$\dot{\zeta}_i(t) = \left[F'(s) + g\lambda_i q'(s)\right] \zeta_i. \tag{B.2}$$

Let's note that, since the Laplacian matrix is symmetrical, all the eigenvalues are real and non-negative and they can be sorted, as $0 = \lambda_1 \leq \lambda_2 \leq ... \leq \lambda_N = \lambda_{max}$. In the limit for t that tends to zero, solutions of these uncoupled equations are simply

$$\zeta_i(t) = \zeta_i^0 e^{\Lambda_i t}, \tag{B.3}$$

where ζ_i^0 is the initially imposed perturbation and $\Lambda_i = [F'(s) + g\lambda_i q'(s)]$. If $\Lambda_i < 0$ for all the components of the perturbation ζ_i ($i = 1, ..., N$) and for all values of $s(t)$, then the synchronous solution is stable.

In particular, one can consider the maximum value which $s(t)$ assumes during its trajectory and define the *master stability function* $\Lambda(\alpha)$:

$$\Lambda(\alpha) = \max_s \left(F'(s) + \alpha q'(s)\right), \tag{B.4}$$

where $\alpha = g\lambda_i$. If $\alpha > 0$ and $\Lambda(\alpha) > 0$ (curve I in Fig. B.1(a)), the synchronized state is never stable. If $\Lambda(\alpha)$ becomes negative for $\alpha > \alpha_c$ (curve II in Fig. B.1(a)), we could have a stable synchronization for a given $g > g_c$. If $\Lambda(\alpha)$ is negative for $\alpha_1 < \alpha < \alpha_2$ (curve III in Fig. B.1(a) and Fig. B.1(b)), we need that $g\lambda_i \in [\alpha_1, \alpha_2]$ for $i = 2, ..., N$ and consequently the coupling constant turns out to be inferiorly and superiorly bounded. The lower bound implies that $g\lambda_2 \geq \alpha_1$, being λ_2 the smallest non-null eigenvalue, while the upper bound is $g\lambda_{max} \leq \alpha_2$,

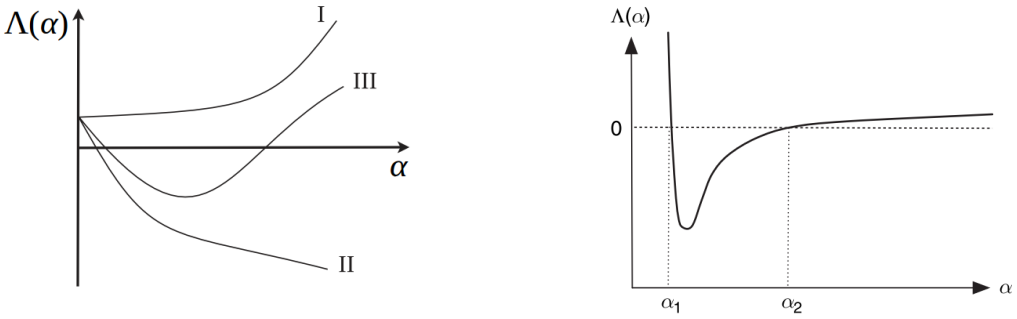

(a) (b)

FIGURE B.1: (a) Three different cases of the master stability function for systems of N coupled oscillators. In all cases $\Lambda(\alpha = 0) > 0$ is the maximum Lyapunov exponent. Case I does not admit a stable synchronous solution, case II gives a stable solution from a certain value on, while case III corresponds to a finite range of negative values for Λ. Image adapted from [32]. (b) A more precise representation of case III: here, the synchronized state is stable for $\alpha \in [\alpha_1, \alpha_2]$ for $i = 2, ..., N$. Image adapted from [117].

so that the synchronous solution is stable if [30]

$$\frac{\alpha_1}{\lambda_2} \leq g \leq \frac{\alpha_2}{\lambda_{max}} \quad \rightarrow \quad \frac{\lambda_{max}}{\lambda_2} \leq \frac{\alpha_2}{\alpha_1}. \tag{B.5}$$

The last stability condition is particular useful, as it associates the spectral properties of the connections network, given by the eigenvalues ratio, with the properties of the oscillators, represented by α_1 and α_1. This means that if we consider a particular class of oscillators with given properties and we only change the connectivity network among them, we could directly influence the emergence of synchronization, as if the nature of the oscillators in a system was not as significant as network topology [14].

Appendix C

More about the Kuramoto model

This appendix is an extension of Section 1.6 and, as stated in that part, the main bibliographical references on which it is based are [2, 11, 15, 30–36].

The first mathematical formulation of synchronization problem on a system of N coupled oscillators was proposed by Arthur Winfree in 1967 [27]. According to his model, which is actually a mean field approximation, each oscillator is characterized by a phase $\phi_i(t)$ and a natural frequency ω_i and it is coupled to the collective signal generated by the whole population:

$$\dot{\phi}_i = \omega_i + \left(\sum_{j=1}^{N} X(\phi_j) Z(\phi_i) \right), \quad i = 1, ..., N. \tag{C.1}$$

To apply the mean field formulation, the underlying connections scheme among the oscillators is assumed to be an all-to-all network: therefore all the j oscillators influence the i-th element through a phase-dependent function $X(\phi_j)$ and the corresponding response of oscillator i is represented by the function $Z(\phi_i)$, which depends on its phase ϕ_i.

Starting from this formulation, Kuramoto preserved the all-to-all topology, but he rewrote the coupling term of the previous equation defining an interaction function Γ_{ij}, which involves some terms of the Winfree model and which depends on a phase difference (see Section 5.2 of [31] for more details):

$$\dot{\phi}_i = \omega_i + \sum_{i,j=1}^{N} \Gamma_{ij}(\phi_j - \phi_i). \tag{C.2}$$

In particular, the simplest case treated by Kuramoto was with equally weighted purely sinusoidal coupling, that is

$$\Gamma_{ij}(\phi_j - \phi_i) = \frac{g}{N} \sin(\phi_j - \phi_i). \tag{C.3}$$

With these interaction functions, Eq. (C.2) turns into Eq. (1.17):

$$\dot{\phi}_i = \omega_i + \frac{g}{N} \sum_{j=1}^{N} \sin(\phi_j - \phi_i), \tag{C.4}$$

where the frequencies ω_i are distributed according to the probability density $P(\omega)$ with the same properties described in Section 1.6: a mean frequency Ω equal to zero (so that the values ω_i correspond to the deviations from 0) and $P(\omega) = P(-\omega)$ for all ω. We also want a decreasing function on $[0; \infty]$, that is $P(\omega) \geq P(\nu)$ whenever $\omega \leq \nu$.

As shown in Section 1.6, defining the Kuramoto parameter

$$R(t)e^{i\psi(t)} = \frac{1}{N} \sum_{j=1}^{N} e^{i\phi_j(t)}, \tag{C.5}$$

the mean-field evolution equation of oscillator i becomes:

$$\dot{\phi}_i = \omega_i + gR \sin(\psi - \phi_i), \tag{C.6}$$

where without loss of generality we can set $\psi = 0$. Indeed we are looking for steady solutions of this model, characterized by a constant amplitude $R(t)$ and a phase $\psi(t)$ which rotates uniformly at frequency Ω, and in the rotating frame where $\Omega = 0$, if we choose correctly the origin of this frame, we get a null phase ψ. In this way, the Kuramoto model expressed by Eq. (C.6) can be written as

$$\dot{\phi}_i = \omega_i - gR \sin \phi_i. \tag{C.7}$$

As in Section 1.4, in order to have a phase locking we need that $\dot{\phi}_i = 0$, but this implies as a condition that $|\omega_i| \leq gR$:

$$\dot{\phi}_i = 0 \;\rightarrow\; \omega_i - gR \sin \phi_i = 0 \tag{C.8}$$

$$\rightarrow\; \phi_i = \arcsin\left(\frac{\omega_i}{gR}\right) \tag{C.9}$$

$$\rightarrow\; \left|\frac{\omega_i}{gR}\right| \leq 1 \tag{C.10}$$

$$\rightarrow\; |\omega_i| \leq gR. \tag{C.11}$$

This condition splits the oscillators population into two groups. The oscillators whose natural frequency satisfies this request (or it is around the mean frequency $\Omega = 0$) approach a stable fixed point defined by $\omega_i = gR \sin \phi_i$ and they are locked. The remaining oscillators with $|\omega_i| > gR$ are called unlocked or drifting. Their natural frequencies belong to the tails of the probability density $P(\omega)$, while their phases evolve in an incoherent way and they produce a stationary uniform distribution around the reference circumference (see for example Fig. 1.6(b)), keeping $R(t)$ constant as requested for the steady solutions, also in the presence of drifting oscillators.

It is now natural to extend this model to the thermodynamic limit $N \to \infty$, where N is the number of oscillators in the system, whose frequency ω_i becomes a continuous variable ω, sampled from the distribution function $P(\omega)$. In this case, we need to define a probability density function $\rho(\phi, \omega, t)$ of the oscillators: $\rho(\phi, \omega, t)d\phi$ gives the fraction of oscillators with natural frequency ω and phase between ϕ and $\phi + d\phi$ at time t, while $\int_o^\gamma \int_{\omega_1}^{\omega_2} \rho(\phi, \omega, t)P(\omega)d\omega d\phi$ denotes the fraction of oscillators which at time t have natural frequency between ω_1 and ω_2 and phase between 0 and γ. Since ρ is a positive and a 2π-periodic function in ϕ, its normalization condition is the following:

$$\int_0^{2\pi} \rho(\phi, \omega, t)d\phi = 1, \tag{C.12}$$

while the continuity equation for its evolution is

$$\frac{\partial \rho}{\partial t} + \frac{\partial}{\partial \phi}[\rho \nu] = 0, \tag{C.13}$$

where

$$\nu(\phi, \omega, t) = \dot{\phi} = \omega - gR \sin \phi \tag{C.14}$$

is the continuous limit of Eq. (C.7) and it represents the instantaneous velocity at time t of a given oscillator with phase ϕ and natural frequency ω. The order parameter is now defined as follows:

$$R(t)e^{i\psi(t)} = R(t) = \int_0^{2\pi} \int_{-\infty}^{+\infty} e^{i\phi} \rho(\phi, \omega, t)P(\omega)d\omega d\phi, \tag{C.15}$$

where as in Eq. (C.5), $\psi(t)$ can be set to 0. The discrete finite-dimensional case of Eq. (C.5) can be recovered by setting $\rho(\phi,\omega,t) = \frac{1}{N}\sum_{j=1}^{N}\delta(\phi - phi_j)$, where $\delta(\cdot)$ is the Dirac δ distribution.

The requested stationary solutions of the continuity equation Eq. (C.13) imply that $\partial\rho/\partial t = 0$ and consequently

$$\frac{\partial}{\partial\phi}\left[\rho\nu\right] = 0, \tag{C.16}$$

or rather $\rho\nu = \rho\cdot(\omega - gR\sin\phi) = C(\omega)$, where $C(\omega)$ is a generic function, not depending on phase ϕ. For $C(\omega)\neq 0$, we get that

$$\rho(\phi,\omega) = \frac{C(\omega)}{|\omega - gR\sin\phi|}, \tag{C.17}$$

where the module in the denominator is added to keep a positive probability function and $C(\omega) = \frac{1}{2\pi}\sqrt{\omega^2 - (gR)^2}$ is computed from the normalization condition Eq. (C.12). The final functional form of $\rho(\phi,\omega)$ depends on the synchronization regime reached by the system.

In the limit for $g\to 0$, that is uncoupled oscillators, each units rotates with its own natural frequency according to the following equation

$$\dot{\phi} = \omega, \tag{C.18}$$

whose the solution is

$$\phi(t) = \omega t + \phi(0), \tag{C.19}$$

being $\phi(0)$ the initial condition. If in this case we define $\phi = \omega t$ ($d\phi = \omega dt$) and we replace it in Eq. (C.15), we obtain

$$R(t) = \int_{-\infty}^{+\infty} e^{i\omega t} f(\omega)d\omega, \tag{C.20}$$

where $f(\omega) = \int_0^{2\pi/\omega}\omega\rho(t,\omega)P(\omega)dt$. By the Riemann-Lebesgue lemma, this integral goes to zero for $t\to\infty$. Therefore, in an uncoupled oscillators system we have that $R(t)\xrightarrow[t\to\infty]{} 0$ and the dynamics is asymptotically asynchronous (see Fig. 1.7(a)). In this incoherent state, as no phase locked group can arise, the phase ϕ of the oscillators is a uniformly distributed variable on the interval $[0;2\pi]$ (Fig. 1.6(b)) and $\rho(\phi,\omega)$ is a constant, equal to $1/2\pi$ (computed through the normalization condition of Eq. (C.12)).

In the limit of strong coupling ($g\to\infty$), each oscillator rotates according to the average phase $\psi = 0$ and it is locked with the mean natural frequency $\omega = \Omega = 0$. This full phase locking implies that $\dot{\phi} = 0$ and consequently, from Eq. (C.14), $\omega - gR\sin\phi = \Omega - gR\sin\phi = 0$, leading $\phi = 0$ for all oscillators. Eq. (C.15) then becomes

$$R(t) = \int_0^{2\pi}\int_{-\infty}^{+\infty}\delta(\omega-\Omega)\rho(\phi,\omega)d\omega d\phi, \tag{C.21}$$

where $P(\omega)$ is simply a Dirac δ function $\delta(\omega-\Omega)$. This yields $\int_{-\infty}^{+\infty}\delta(\omega-\Omega)\rho(\phi,\omega)d\omega = \rho(\phi,\Omega = 0)$ and the final expression

$$R(t) = \int_0^{2\pi}\rho(\phi,\Omega=0)d\phi. \tag{C.22}$$

is exactly the initial normalization condition (Eq. (C.12)): therefore, in the limit of strong coupling we have actually proved that $R(t)\xrightarrow[t\to\infty]{} 1$, which corresponds to the total synchronous state (Fig. 1.6(d) and Fig. 1.7(a)).

In the intermediate region between uncoupled and strongly coupled oscillators, we observe that some oscillators are phase locked to the average phase ($\dot{\phi} = 0$), while all the other elements

are unlocked. Such a regime is a partial synchronization, where $0 < R(t) < 1$, and in particular it appears for $g > g_c$ (Fig. 1.7(b)). As shown above in Eq. (C.11)), the locked (unlocked) group includes those oscillators, whose natural frequency ω obeys the condition $|\omega| \leq (>) gR$. This allows us to split Eq. (C.15) into two contributions:

$$R(t) = \int_0^{2\pi} \int_{|\omega| \leq gR} e^{i\phi} \rho(\phi, \omega) P(\omega) d\omega d\phi + \int_0^{2\pi} \int_{|\omega| > gR} e^{i\phi} \rho(\phi, \omega) P(\omega) d\omega d\phi, \tag{C.23}$$

where the first part refers to the locked oscillators, the second one to the unlocked or drifting oscillators and the probability density distribution is:

$$\rho(\phi, \omega) = \begin{cases} \delta \left[\phi - \sin^{-1} \left(\frac{\omega}{gR} \right) \right] H(\cos \phi), & |\omega| \leq gR \\ \frac{\sqrt{\omega^2 - (gR)^2}}{2\pi |\omega - gR \sin \phi|}, & |\omega| > gR \end{cases} \tag{C.24}$$

(see also Eq. (C.17)) where $H(x)$ is the Heaviside unit step function ($H(x) = 1$ if $x > 0$, $H(x) = 0$ if $x \leq 0$). Due to the symmetry properties of $P(\omega)$ ($P(\omega) = P(-\omega)$) and the periodicity of ρ ($\rho(\phi + \pi, -\omega) = \rho(\phi, \omega)$), one can easily prove that the second contribution of Eq. (C.23) is null.

The first contribution can be read as an average phase of the locked population (angular brackets notation):

$$\begin{aligned} R(t) &= \langle e^{i\phi} \rangle = \langle \cos \phi \rangle + i \langle \sin \phi \rangle \\ &= \int_0^{2\pi} \int_{-gR}^{+gR} \cos \phi \rho(\phi, \omega) P(\omega) d\omega d\phi + i \int_0^{2\pi} \int_{-gR}^{+gR} \sin \phi \rho(\phi, \omega) P(\omega) d\omega d\phi, \end{aligned} \tag{C.25}$$

where we use the Euler's formula for complex number ($e^{iz} = \cos z + i \sin z$) to write $e^{i\phi}$ and to split further the integral. Here, since $P(\omega) = P(-\omega)$, we can reasonably assume that also the phase distribution of locked oscillators is symmetric about $\phi = 0$ or equivalently that there are as many oscillators with phase ϕ^* as with phase $-\phi^*$): indeed for the locked population $\omega = gR \sin \phi$, as we have stated above (odd function), for example in Eq. (C.8). Taking advantage again of the symmetry properties of the integrand function in the second integral of previous equation, we get $\langle \sin \phi \rangle = 0$, while thanks to Eq. (C.24) the first integral reads:

$$R(t) = \langle \cos \phi \rangle = \int_0^{2\pi} \int_{-gR}^{+gR} \cos \phi \delta \left[\phi - \sin^{-1} \left(\frac{\omega}{gR} \right) \right] H(\cos \phi) P(\omega) d\omega d\phi. \tag{C.26}$$

With a variable change $\omega = gR \sin \phi$ ($d\omega = gR \cos \phi d\phi$, with $\phi \in [-\pi/2; \pi/2]$), we finally achieve the self-consistency condition of the Kuramoto model in the thermodynamic limit:

$$R = gR \int_{-\pi/2}^{+\pi/2} \cos^2 \phi P(gR \sin \phi) d\phi, \tag{C.27}$$

where for simplicity we omit the time dependency of the Kuramoto parameter $R(t)$.

Again, a trivial solution corresponds to $R = 0$ and to the complete asynchronous state. For $R > 0$ we get the partially synchronous regime, whose solutions have to satisfy the self-consistency equation

$$1 = g \int_{-\pi/2}^{+\pi/2} \cos^2 \phi P(gR \sin \phi) d\phi. \tag{C.28}$$

This branch bifurcates continuously from $R = 0$ at a given mean field critical value g_c for the coupling, which can be computed taking the limit with $R \to 0$, as close to that critical point R is expected to be small. Expanding $P(\omega)$ in powers of R $\left(P^{(k)}(0) = \frac{dP(\omega)}{d\omega}\Big|_{\omega=0} \right)$, we get

$$
\begin{aligned}
1 &= g\int_{-\pi/2}^{+\pi/2}\cos^2\phi\left(P(0)+gR\sin\phi P'(0)+\frac{g^2R^2\sin^2\phi}{2}P''(0)+o(R^3)\right)d\phi \\
&= gP(0)\int_{-\pi/2}^{+\pi/2}\cos^2\phi d\phi + g^2RP'(0)\int_{-\pi/2}^{+\pi/2}\cos^2\phi\sin\phi d\phi \\
&+ \frac{g^3R^2P''(0)}{2}\int_{-\pi/2}^{+\pi/2}\cos^2\phi\sin^2\phi d\phi + o(R^3) \\
&= gP(0)\frac{\pi}{2}+\frac{g^3R^2P''(0)}{2}\frac{\pi}{8}+o(R^4),
\end{aligned}
\tag{C.29}
$$

and in particular

$$
1-gP(0)\frac{\pi}{2}=0. \tag{C.30}
$$

From this last line we read the Kuramoto result for the critical coupling g_c at the onset of synchronization:

$$
g=g_c=\frac{2}{\pi P(0)}. \tag{C.31}
$$

Now, if we define the bifurcation parameter $\mu=\frac{g-g_c}{g_c}$ ($g=\mu g_c+g_c$), where $\mu<(>)0$ represents the weak (strong) coupling regime with the stable (unstable) null solution, and we replace it in Eq. (C.29), we have

$$
1-\frac{\pi}{2}(\mu g_c+g_c)P(0)-\frac{\pi}{16}(\mu g_c+g_c)^3R^2P''(0)=0. \tag{C.32}
$$

Setting $\mu\approx 0$, as we are close to the critical point, so that we can neglect all terms proportional to μ^2 or μ^3, the previous equation becomes

$$
\frac{\pi}{2}\mu g_cP(0)-\frac{\pi}{16}g_c^3R^2P''(0)=0, \tag{C.33}
$$

from where the amplitude of the bifurcating branch can be finally written as

$$
R=\sqrt{\left|\frac{8P(0)\mu}{g_c^2P''(0)}\right|}=\sqrt{\left|\frac{8P(0)(g-g_c)}{g_c^3P''(0)}\right|}. \tag{C.34}
$$

If $P(\omega)$ is concave at $\omega=0$ ($P''(0)\leq 0$), then we have a supercritical bifurcation and the solution is stable: once a small group of oscillators get locked initiated, a positive feedback is established and more and more elements join the group, until a full synchronization of the whole system is reached. Such a transition in represented in Fig. C.1(a) or in Fig. 1.7(b). If otherwise $P(\omega)$ is convex at $\omega=0$ ($P''(0)\geq 0$), then we have a subcritical bifurcation (Fig. C.1(b)) and the solution is unstable: the synchronous nucleation process is inhibited and the growth of the locked subset is suppressed.

In particular for the supercritical case, if we join the asynchronous simple solution $R=0$ and the partially synchronous one written in Eq. (C.34), we get that for a general frequency distribution $P(\omega)$ in the limit of $N\to\infty$ and $t\to\infty$, the synchronization order parameter behaves as

$$
R=\begin{cases}0, & g<g_c\\ s\sqrt{g-g_c}, & g\geq g_c,\end{cases} \tag{C.35}
$$

where $g_c=\frac{2}{\pi P(0)}$ and s is a constant, which depends on g_c and on the properties of $P(\omega)$. The typical graph of this analytical function is what actually appears in Fig. 1.7(b) or in Fig. C.1(a).

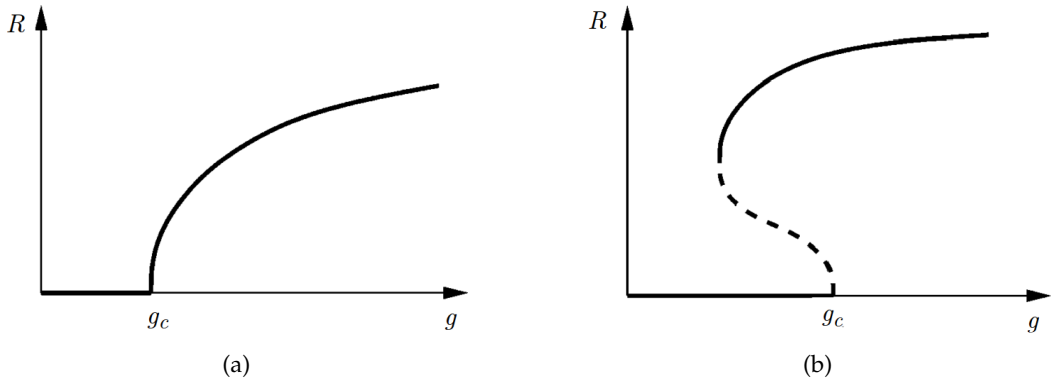

FIGURE C.1: (a) Supercritical bifurcation of R as a function of the coupling g. Image adapted from [33]. (b) Supercritical bifurcation of R as a function of the coupling g. Image adapted from [33].

Since all these analytical results are based on specific more or less strict assumptions, from the publication of Kuramoto results onwards massive numerical simulations have been performed to better investigate and prove the synchronization transition of Kuramoto model on complex networks.

Starting from this final result, Kuramoto himself and other researchers, as for example Nancy Kopell [179] from a theoretical point of view or Daido [180] and Nishikawa [181] through computer simulations and physical arguments and many other in the following years, tried to repeat same analyzes for large but finite N, in order to prove a convergence of these results for $N \to \infty$. Although this is still an open and debated problem, up to now it is reasonably to state that finite$-N$ fluctuations remain of order $O(N^{-1/2})$.

Another issue concerns how to embed the Kuramoto model on a complex networks characterized by a specific topology, rather than an all-to-all connectivity as supposed at the beginning of this Appendix for the original Kuramoto analysis. Unlike the fully connected graph case, the Kuramoto model has no exact solutions in heterogeneous networks, as the corresponding evolution equations cannot be decoupled through the mean field quantities of Eq. (C.5), but we should take into account some approximations.

To add topology information in the initial system of N coupled oscillators, we need to rewrite Eq. (C.4) with the adjacency matrix elements ϵ_{ij}, which tell us how the oscillators are coupled, and we get

$$\dot{\phi}_i = \omega_i + \frac{g}{C_N} \sum_{j=1}^{N} \epsilon_{ij} \sin(\phi_j - \phi_i), \tag{C.36}$$

Here, the normalization constant N is replaced with a more general factor C_N, as now it must be properly chosen based on the scaling of the connectivity matrix with the system size, to keep the model well defined in the thermodynamic limit. A correct choice of this normalization factor let us also to better compare synchronization in different network topologies, to determine the onset of synchronization and to properly investigate the interplay between topology and coherent dynamics. In the fully connected network, C_N has been set equal to N, since the coupling strength among the oscillators grows linearly with the size N, but such a prescription implies that the coupling goes to zeros for those oscillators whose connections number with other nodes, or degree, scales with N. Note that those nodes exist with a very small probability only if we consider scale-free networks, that is networks with a power-law degree distribution $P(k) \sim k^{-\alpha}$.

Another possible choice is $C_N = k_i$, where k_i id the degree of oscillator i, proposed by Motter et al. [13] to deal with the so-called "paradox of heterogeneity" (see Section 4.1). The

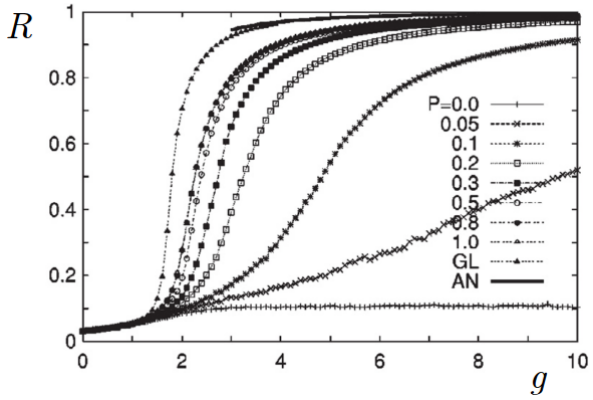

FIGURE C.2: Order parameter R as a function of coupling g for SW networks with size $N = 800$ and with different values of the rewiring probability p. GL and AN respectively correspond to the globally coupled network and its respective analytical solution. Image adapted from [182].

prescriptions $C_N = \langle k \rangle$, where $\langle k \rangle$ is the average connectivity of the graph, or $C_N = k_{max}$, where k_{max} is the maximum degree, or any other quantity related to the topology are also suitable, provided the thermodynamics limit remains well-defined: from a physical point of view, they correspond to a rescaling of the temporal scales in the system dynamics.

Now, let us consider a small-world network (SW, see Appendix A) of oscillators built on a 1D ring with natural frequencies distributed according to a Gaussian distribution and $C_N = \langle k \rangle$. Numerically computing the order parameter R as a function the coupling strength for different value of the rewiring probability p, it has been found [182] that even a small p is able to highly improve network synchronization in comparison to the completely regular case and for $p = 0.5$ the synchronization of SW networks is substantially similar to the all-to-all topology results ($p = 1$), as shown in Fig. C.2. In this case, the scaling form of the order parameter R is

$$R = N^{-\beta/\nu} F\left[(g - g_c) N^{1/\nu}\right], \tag{C.37}$$

where F is a scaling function, β is the transition critical exponent and ν is the correlation length exponent, whose values are compatible with the mean-field (fully connected topology) results $\beta \approx 0.5$ and $\nu \approx 2.0$.

Also in scale-free networks generated through the BA model (see Appendix A) with uniform frequency distribution, a similar square-root behavior of R has been shown [129], finding $\beta \sim 0.46$, as what we have described in the original mean-field Kuramoto model.

A vary interesting and quite general result for uncorrelated random networks with arbitrary degree distribution was obtained by Ichinomiya in 2004 [128], who finds that the critical coupling is given by the expression

$$g_c = c \frac{\langle k \rangle}{\langle k^2 \rangle} \tag{C.38}$$

where the distribution second moment $\langle k^2 \rangle$ measures the degree fluctuations and the constant c depends on the frequency distribution $P(\omega)$. In particular, if $\langle k^2 \rangle$ diverges, as for example in power-law degree distributions $P(k) \sim k^{-\alpha}$ with $0 < \alpha < 3$, g_c goes towards zero in the limit of $N \to \infty$. Finally, in this last case of scale-free topology, the critical behavior of the order parameter R at the onset of synchronization has been computed [127] using the mean

field approach, obtaining that $R \sim [(g - g_c)/g_c]^{\beta}$, where

$$R \sim \begin{cases} \frac{1}{2}, & \alpha > 5 \\ \frac{1}{\alpha - 3}, & 3 < \alpha < 5. \end{cases} \tag{C.39}$$

Since its first formulation, the Kuramoto model has been intensively investigated from many points of view, showing a large variety of synchronization patterns, and nevertheless many open questions still deserve a special attention. From one side, its simplicity let us achieve a rigorous mathematical analysis, at least in the mean field formulation and, from the other side, it has gained a remarkable success thanks to its capacity of understanding and explaining synchronization phenomena in large populations of phase oscillators and in many different contexts.

Appendix D

Beyond the heterogeneous mean field formulation

This Appendix is an extension of the results presented in Chapter 5. Here, we compare the dynamics in the HMF formulation, introduced in Section 3.5, with the dynamics on a network with finite connectivity and in particular in an excitatory and inhibitory network, whose dynamics is described by Eqs. (3.28).

Starting from the event-driven map of a purely excitatory network, which is reported in Eqs. (3.30-3.34), in the excitatory/inhibitory case the map will read

$$
\begin{aligned}
y_{i,E}(n+1) &= y_{i,E}(n)e^{-\frac{\tau(n)}{\tau_{in}}} + U\left[1 - \frac{\tau_r^E}{\tau_r^E - \tau_{in}} y_{i,E}(n)\left(e^{-\frac{\tau(n)}{\tau_r^E}} - \frac{\tau_{in}}{\tau_r^E}e^{-\frac{\tau(n)}{\tau_{in}}}\right) - z_{i,E}(n)e^{-\frac{\tau(n)}{\tau_r^E}}\right]\delta_{i,s} \\
y_{i,I}(n+1) &= y_{i,I}(n)e^{-\frac{\tau(n)}{\tau_{in}}} + u_i(n)\left[1 - \frac{\tau_r^I}{\tau_r^I - \tau_{in}} y_{i,I}(n)\left(e^{-\frac{\tau(n)}{\tau_r^I}} - \frac{\tau_{in}}{\tau_r^I}e^{-\frac{\tau(n)}{\tau_{in}}}\right) - z_{i,I}(n)e^{-\frac{\tau(n)}{\tau_r^I}}\right]\delta_{i,s} \\
z_{i,E}(n+1) &= z_{i,E}(n)e^{-\frac{\tau(n)}{\tau_r^E}} + \frac{\tau_r^E}{\tau_r^E - \tau_{in}} y_{i,E}(n)\left[e^{-\frac{\tau(n)}{\tau_r^E}} - e^{-\frac{\tau(n)}{\tau_{in}}}\right] \\
z_{i,I}(n+1) &= z_{i,I}(n)e^{-\frac{\tau(n)}{\tau_r^I}} + \frac{\tau_r^I}{\tau_r^I - \tau_{in}} y_{i,I}(n)\left[e^{-\frac{\tau(n)}{\tau_r^I}} - e^{-\frac{\tau(n)}{\tau_{in}}}\right] \\
v_i(n+1) &= 0, \text{ if } i = s \\
v_i(n+1) &= v_i(n)e^{-\tau(n)} + b(1 - e^{-\tau(n)}) + \frac{g}{\langle k \rangle} F_i(n), \text{ if } i \neq s \\
u_i(n+1) &= \left[u_i(n)(1-U)e^{-\frac{\tau(n)}{\tau_f}}\right] + U, \text{ if } i = s \\
u_i(n+1) &= u_i(n)e^{-\frac{\tau(n)}{\tau_f}}, \text{ if } i \neq s \\
&\text{with } F_i(n) = \frac{\tau_{in}\left(e^{-\frac{\tau(n)}{\tau_{in}}} - e^{-\tau(n)}\right)}{\tau_{in} - 1} \cdot \sum_{j=1}^{N} \epsilon_{ij} y_{j,E}(n), \text{ if } i \text{ is } E \\
&\text{or } F_i(n) = \frac{\tau_{in}\left(e^{-\frac{\tau(n)}{\tau_{in}}} - e^{-\tau(n)}\right)}{\tau_{in} - 1} \cdot \sum_{j=1}^{N} \epsilon_{ij} y_{j,I}(n), \text{ if } i \text{ is } I,
\end{aligned}
\tag{D.1}
$$

where ϵ_{ij} are the elements of the adjacency matrix, s is the index of the neuron which at the $n-$th integration step has emitted a spike and $\delta_{i,s}$ is the Kronecker δ function; $y_{i,\dagger}$ are the active resources of node i towards a node of type $\dagger = E, I$ (E for excitatory and I for inhibitory) and similarly for all the other resources. See Section 3.4 for more details on the other variables.

Once defined this integration map, the algorithm simulation is the same which we have exposed in Section 3.4. Then, given the size N of the network, we extract the degree k_i (remember

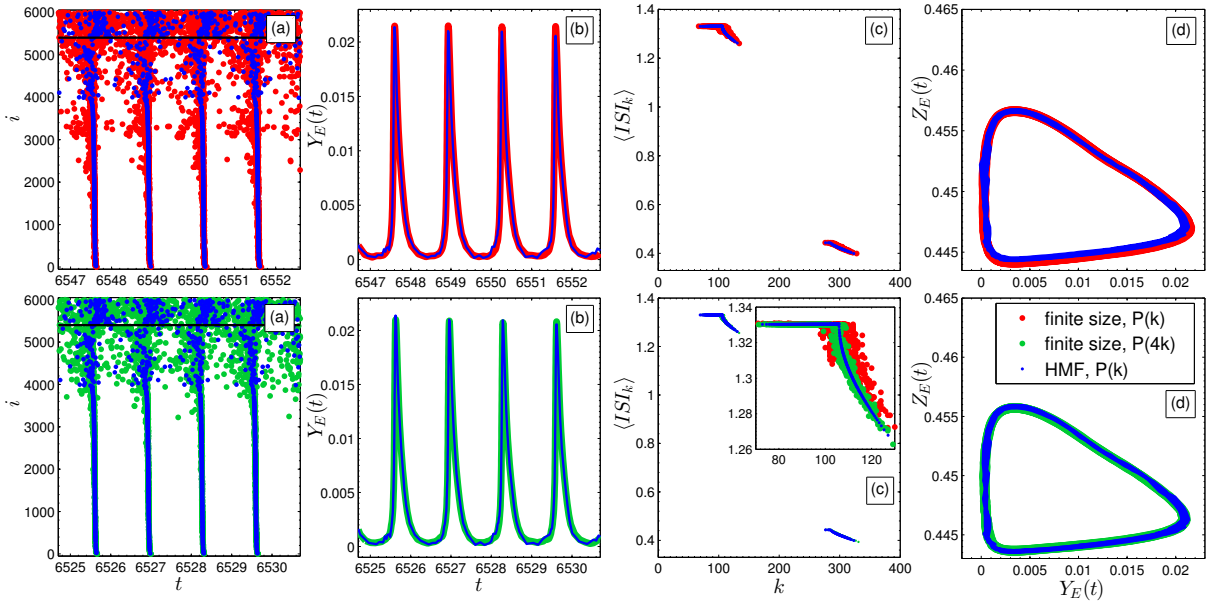

FIGURE D.1: Comparison of the dynamics of a network with $f_I = 0.1$, simulated through both the finite connectivity and the HMF approach. In the upper figures red data are produced evolving the finite connectivity equations with $N = 6000$ neurons, and blue data the HMF ones with $M = 500$ connectivity classes. The p.d.f. is characterized in both cases by $\langle k_E \rangle = 100$, $\Delta = 200$, and $\sigma = 10$. In the lower figures we show how the HMF approximation improves as we approach the limit of $k_i \to \infty$. Again, green (blue) data evolve according to the finite connectivity (HMF) approach, but for the finite connectivity network we have quadrupled the degrees (new p.d.f. parameters: $\langle k_E \rangle = 400$, $\Delta = 800$, $\sigma = 40$). Thanks to this higher connectivity, the finite connectivity dynamics better converges to the same HMF network. In panels (a) we compare the raster plots. As in the HMF figures M is equal to 500, the HMF indices have been opportunely rescaled for a better overlap with the red and green data. Data below (above) the black line refer to excitatory (inhibitory) nodes. (b) Field $Y_E(t)$ as a function of time. The comparison of $Y_I(t)$ gives similar results. (c) $\langle \text{ISI}_k \rangle$ as a function of the degree k. In the lower panel, we divided the degrees of green data by 4, to overlap finite size data with HMF points. The inset is a zoom of the $\langle \text{ISI}_k \rangle$ only for the excitatory neurons and for all three sets of data. (d) Attractors $Y_E(t)$ vs $Z_E(t)$. Image from [115].

that this is both the input and the output degree) of each node from the same Gaussian distributions $P_E(k)$ and $P_I(k)$, used in Chapter 5, and we build a class of random graphs, writing its adjacency matrix of elements ϵ_{ij} through the configuration model (see Appendix A). Self-link, that is link from a neuron to itself, or multiple links are forbidden. Note that, since the transmission direction of an action potential through a synapse is well-defined by the synaptic morphological features, we will deal with directed graphs.

We clearly expect the result to improve as the graph connectivities grow. In order to verify that, we set $\langle k_I \rangle = 3\langle k_E \rangle$ (where $\angle k_E \rangle$ and $\langle k_I \rangle$ are the average of the excitatory and and the inhibitory Gaussian, respectively, and $\Delta = \langle k_I \rangle - \langle k_E \rangle = 2\langle k_E \rangle$) and the standard deviation $\sigma = \langle k_E \rangle / 10$ for both excitatory and inhibitory neurons, so that by varying the values of $\langle k_E \rangle$ we get finite graphs with different average connectivity, which will be approximated by the same HMF equations. Finally, fixing the fraction f_I, we can consider the different dynamical regimes observed in Section 5.2: quasisynchronous, synchronous with balance and asynchronous.

In Fig. D.1 we consider $f_I = 0.1$, which corresponds to the regime of partial synchronization, emerging when f_I is (much) smaller than its balance value f_I^B. In all the panels of that

figure, the blue data are obtained from the simulation of the HMF equations. The upper panels refer to $k_E = 100$, while the lower panels to $k_E = 400$. Panels (a) represent the raster plots and panels (b) the synaptic fields $Y_E(t)$, which in the finite connectivity formulation can be defined as Eq. (3.24) or as

$$Y_E(t) = +Y_{EE}(t) - Y_{EI}(t) = \frac{1}{L}\Big(\sum_{i,j\in E,E} y_{ij}k_i - \sum_{i,j\in E,I} y_{ij}k_i \Big), \tag{D.2}$$

where L is the total number of links in the network, $\sum_{i,j\in E,I}$ means that the sum is restricted to the y_{ij} resources from an inhibitory node to an excitatory one and similarly for $\sum_{i,j\in E,E}$. Panels (c) show the time average $\langle ISI_k \rangle$ of interspike interval as a function of the connectivity and finally in panels (d) we plot the microscopic attractors $Y_E(t)$ vs $Z_E(t)$[1].

Figure D.1 shows that HMF and finite connectivity networks display a similar behavior and the main effect of finite connectivity is to superimpose on the HMF dynamics a noise, which is clearly vanishing by increasing the connectivity of the graph. Analogous conclusions can be found for all the dynamical regimes where the fraction of inhibitory neurons is much smaller than the balance value. A similar accordance can be observed also in the asynchronous regime, when $f_I > f_I^B$. However, as in that regime the network activity is aperiodic and the fluctuations are dominant both for the synaptic fields and for the attractors, we do not show the comparison plots.

A substantial difference emerges in the balance regime, where the HMF approach is characterized by a totally synchronous dynamics, while the asymptotic stable state for the finite connectivity system seems to be asynchronous. Indeed, the synchronization in the mean-field formulation is a consequence of a perfect field subtraction, as we have seen in Section 5.3, but in networks with finite connectivity fluctuations dominate and destroy the phases locking inducing the synchronization. However, the totally synchronous state characterizing the HMF dynamics emerges in the finite connectivity system as a metastable state, whose lifetime increases with the network connectivity.

In Fig. D.2 we consider the balance regime $f_I = f_I^B = 0.25$ for $\langle k_E \rangle = 100$ or $\Delta = 200$: the lower panel shows the raster plots of three different networks, taken from time $t = 100$ after that a stimulus synchronized the whole dynamics. In the first network, with lower connectivity, the synchronous configuration is for the most part destroyed and the dynamics is quickly returning to the asynchronous state, but in the other raster plots, where the degree is two or four times larger, the network still remains quite synchronous, showing that the lifetime of the periodic dynamics diverges with the connectivity. The synchronization of the system can be measured using the same parameter $1 - R(t)$ used in Section 5.4 and plotting it as a function of time (the totally synchronous stimulus is applied at t = 0). The behavior of $1 - R(t)$ is illustrated in the upper panel of Fig. D.2, underlining that the larger the connectivity in the network is, the more stable the synchronous state is.

Eventually, we show that, even if the HMF and finite connectivity dynamics have different attractors, the conclusions we have drawn regarding the high performance for input detection in this dynamical regime are still valid also in finite connectivity samples. For this purpose, let us consider the response of the finite connectivity network to the application of an external stimulus, in analogy with the results for the HMF approach shown in Section 5.4. As previously, we synchronize a fraction equal to $S = 0.3$ of the excitatory nodes, following the same procedure of the HMF simulations, and we measure the stimulus perturbation through the difference between the excitatory fields produced by the nonsynchronized and synchronized

[1] in the finite connectivity network $Z_E(t)$ is defined analogously to Eq. (D.2), using the resources z_{ij} instead of y_{ij}, while in the HMF simulation it is computed similarly to Eqs. (3.48) and 3.47, using $z_k^{(\dagger,*)}$ instead of $y_k^{(\dagger,*)}$.

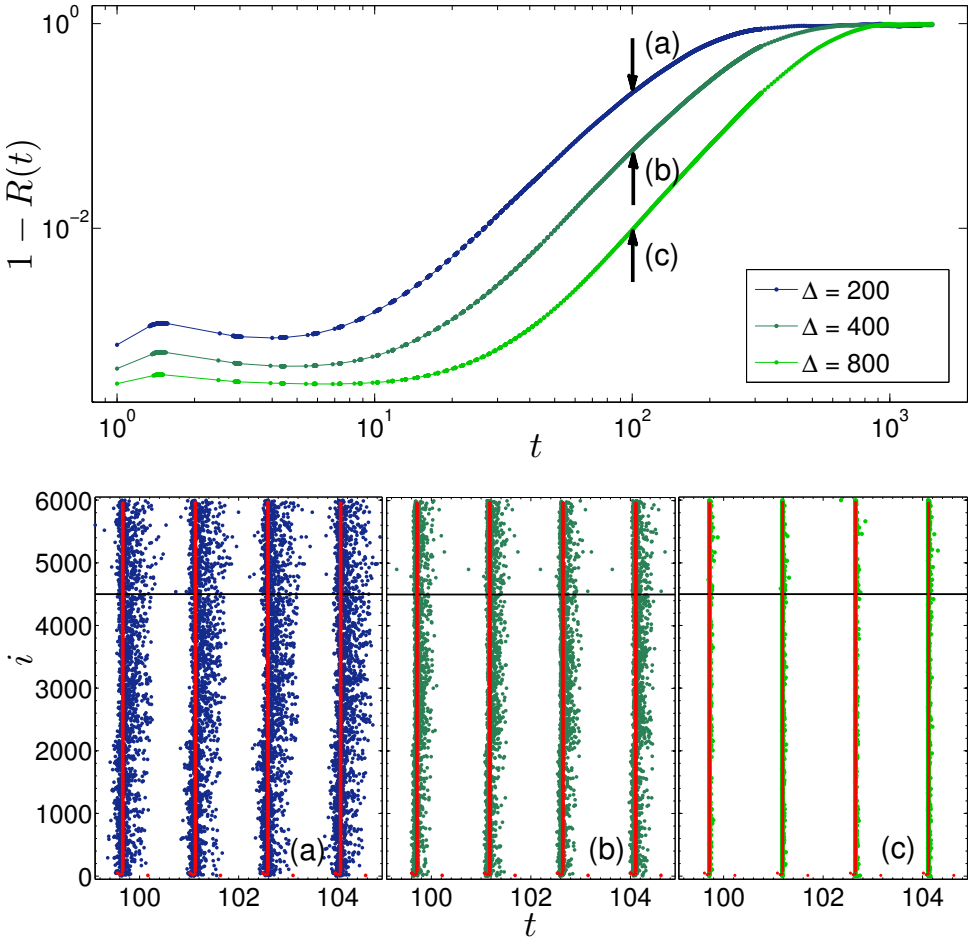

FIGURE D.2: Stability of the synchronous state in finite connectivity simulations. In the upper panel we compare the time evolution of the parameter $1 - R(t)$ (in logarithmic scale) in three different networks with $N = 6000$ neurons and $f_I = 0.25$. The p.d.f. of the first network (blue data) is characterized by $\Delta = 200$, $\langle k_E \rangle = 100$, $\sigma = 10$; the p.d.f. of the second network is doubled (dark green data, $\Delta = 400$, $\langle k_E \rangle = 200$, $\sigma = 20$); the p.d.f. of the last network is quadrupled (light green data, $\Delta = 800$, $\langle k_E \rangle = 400$, $\sigma = 40$). The external stimulus is applied at time $t = 0$ to all neurons. At the beginning $1 - R(t)$ is almost null, because the system is totally synchronous, but then due to the finite connectivity fluctuations it returns to 1, that is the network evolves towards its stable asynchronous state. In correspondence of the black arrows, we show in the three lower figures the microscopic dynamics of the networks through their raster plots. The indices below (above) the black line refer to excitatory (inhibitory) neurons. Image from [115].

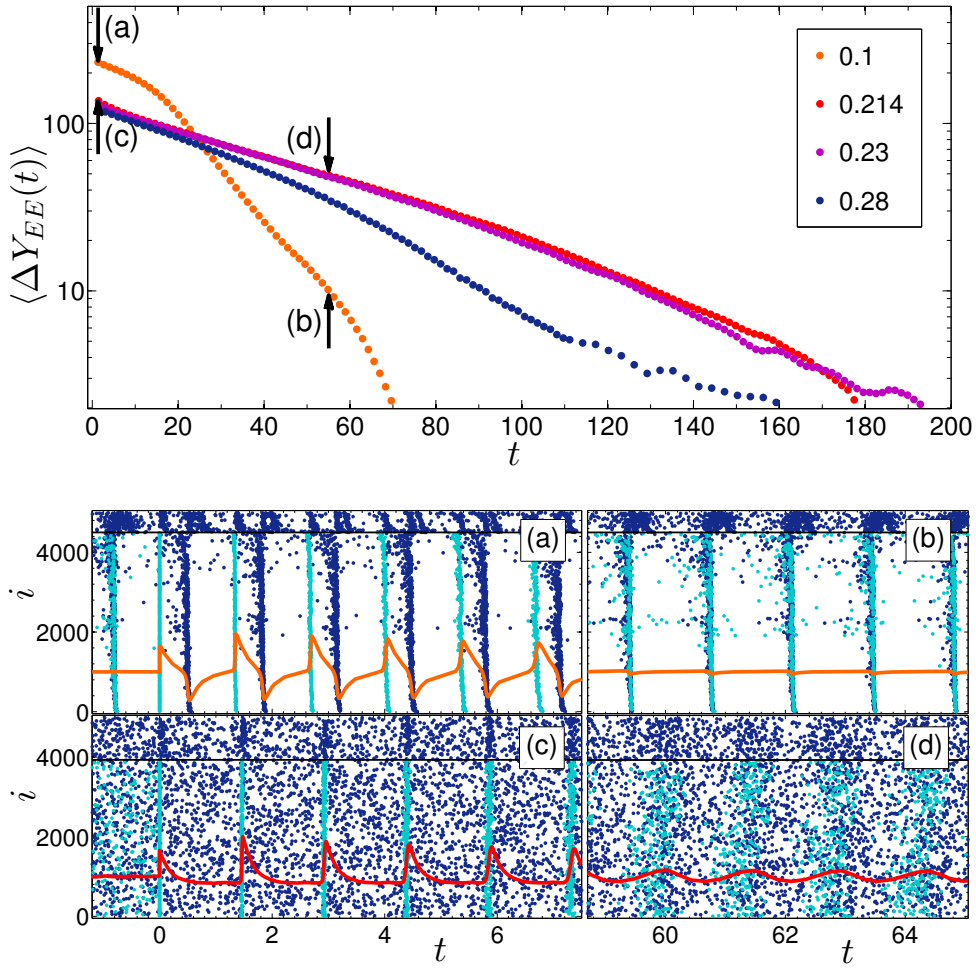

FIGURE D.3: Dynamics of finite connectivity networks after the application of an external stimulus at time $t = 0$ to 30% of excitatory neurons, randomly chosen, with $N = 5000$ neurons, $\Delta = 250$, $\langle k_E \rangle = 100$, $\sigma = 10$ and different inhibitory fractions f_I (see the legend). For each network we plot in the upper panel (in semilogarithmic scale) the temporal average values $\langle \Delta Y_{EE}(t) \rangle$ as a function of time, starting from $t = 0$. In correspondence of the black arrows, in the lower panels we show snapshots of the raster plot taken at different times for the network with $f_I = 0.1$ [(a) and (b)] and with $f_I = 0.214$ [(c) and (d)]. The spike events of stimulated (nonstimulated) nodes are represented by light (dark) blue dots, while the orange and red lines are the signals defined in Eq. (D.3). To better overlap signals with raster plots, we shifted them adding a positive constant: this is why they are not null before the stimulus. After the stimulus, signals turn on sharply and then decay. The indices below (above) the black line refer to excitatory (inhibitory) neurons. Image from [115].

nodes respectively, as follows:

$$\Delta Y_{EE}(t) = S\, Y_{EE}^{not-st}(t) - (1-S)\, Y_{EE}^{st}(t), \tag{D.3}$$

where $Y_{EE}^{not-st}(t)$ and $Y_{EE}^{st}(t)$ are computed according to the first sum in Eq. (D.2), limiting it to the excitatory neurons which have been respectively not stimulated and stimulated. We also add the normalization factors S and $1-S$, as the first and the second field are produced by a different number of neurons: in this way, before the stimulus, $\Delta Y_{EE}(t)$ fluctuates around zeros. The temporal evolution of such variable is plotted with orange and red lines on the raster plots in Fig. D.3. As we have periodic signals, in order to better describe their decays, we compute the average value for each period and we plot the results in the upper panel of Fig. D.3.

In the initial dynamical regime of partial synchronization ($f_I = 0.1$), the perturbation produced by the stimulus decays fast and after few oscillations the system returns to the initial configuration (see the raster plots in Fig. D.3(a) and (b)). In the metastable and in the totally synchronous regime, when the inhibitory fraction is around the balance value ($f_I = 0.214$ and $f_I = 0.23$), the time required to return to the original synchronization level is longer and the signal decay is slower. Then the decay rate increases again if we consider the asynchronous states after the balance regime ($f_I = 0.28$ for example).

These results point out that the long response time of the system to an external stimulus is an effect which is present not only in the HMF approach but also in finite connectivity networks, though in this case the balance regime is asymptotically asynchronous.

Bibliography

[1] G. Buzsaki. *Rhythms of the brain* (Oxford University Press, 2006).

[2] A. Pikovsky, M. Rosenblum and J. Kurths. *Synchronization: a universal concept in nonlinear sciences*, Vol. 12 (Cambridge university press, 2003).

[3] E. Kandel, J. Schwartz and T. Jessell. *Principles of neural science (4th edition)* (McGraw-Hill, New York, 2000).

[4] W. Klimesch. Memory processes, brain oscillations and eeg synchronization. *International journal of psychophysiology* **24**, 61–100 (1996).

[5] A. Schnitzler and J. Gross. Normal and pathological oscillatory communication in the brain. *Nature reviews. Neuroscience* **6**, 285 (2005).

[6] J. McAuley and C. Marsden. Physiological and pathological tremors and rhythmic central motor control. *Brain* **123**, 1545–1567 (2000).

[7] E. Bullmore and O. Sporns. Complex brain networks: graph theoretical analysis of structural and functional systems. *Nature reviews. Neuroscience* **10**, 186 (2009).

[8] M. P. van den Heuvel and O. Sporns. Network hubs in the human brain. *Trends in cognitive sciences* **17**, 683–696 (2013).

[9] H. Markram, M. Toledo-Rodriguez, Y. Wang, A. Gupta, G. Silberberg and C. Wu. Interneurons of the neocortical inhibitory system. *Nature reviews neuroscience* **5**, 793–807 (2004).

[10] M. Tsodyks, A. Uziel, H. Markram et al. Synchrony generation in recurrent networks with frequency-dependent synapses. *J Neurosci* **20**, 825–835 (2000).

[11] A. Barrat, M. Barthelemy and A. Vespignani. *Dynamical processes on complex networks* (Cambridge university press, 2008).

[12] M. di Volo, R. Burioni, M. Casartelli, R. Livi and A. Vezzani. Heterogeneous mean field for neural networks with short-term plasticity. *Physical Review E* **90**, 022811 (2014).

[13] A. E. Motter, C. Zhou and J. Kurths. Network synchronization, diffusion, and the paradox of heterogeneity. *Physical Review E* **71**, 016116 (2005).

[14] A. Balanov, N. Janson, D. Postnov and O. Sosnovtseva. *Synchronization: from simple to complex* (Springer-Verlag Berlin Heidelberg, 2009).

[15] G. Osipov, J. Kurths and C. S. Zhou. *Synchronization in oscillatory networks* (Springer Science & Business Media, 2007).

[16] S. Boccaletti, J. Kurths, G. Osipov, D. L. Valladares and C. S. Zhou. The synchronization of chaotic systems. *Physics reports* **366**, 1–101 (2002).

[17] C. Huygens. *Christiaan Huygens' the pendulum clock, or, Geometrical demonstrations concerning the motion of pendula as applied to clocks* (Iowa State Pr, 1986).

[18] E. Kaempfer. *The History of Japan (with a description of the kingdom of Siam)*, Vol. 1727 (Sloan, London, 1906).

[19] W. H. Eccles and J. H. Vincent, *British Patent Spec. clxiii* (1920).

[20] E. V. Appleton. Automatic synchronization of triode oscillators. *Proc. Cambridge Phil. Soc* **21**, 231 (1922).

[21] B. Van Der Pol. Vii. Forced oscillations in a circuit with non-linear resistance. (reception with reactive triode). *The London, Edinburgh, and Dublin Philosophical Magazine and Journal of Science* **3**, 65–80 (1927).

[22] J. W. S. Rayleigh. *The Theory of Sound* (Dover Publications, New York, USA, 1945).

[23] J. Simonet, M. Warden and E. Brun. Locking and arnold tongues in an infinite-dimensional system: the nuclear magnetic resonance laser with delayed feedback. *Physical Review E* **50**, 3383 (1994).

[24] S. H. Strogatz. *Nonlinear dynamics and chaos: with applications to physics, biology, chemistry, and engineering* (Westview press, 2014).

[25] M. Cencini, F. Cecconi and A. Vulpiani. *Chaos: from simple models to complex systems* (World Scientific, 2010).

[26] N. Wiener. *Cybernetics: control and communication in the animal and the machine* (Wiley New York, 1948).

[27] A. T. Winfree. Biological rhythms and the behavior of populations of coupled oscillators. *Journal of theoretical biology* **16**, 15–42 (1967).

[28] A. A. Andronov, A. A. Vitt and S. E. Khaikin. *Theory of oscillators*, International series of monographs in physics (Pergamon Press; U.S.A. ed. distributed by Addison-Wesley Pub. Co., Reading, Mass., 1966).

[29] E. M. Izhikevich. *Dynamical systems in neuroscience* (MIT press, 2007).

[30] A. Arenas, A. Díaz-Guilera, J. Kurths, Y. Moreno and C. Zhou. Synchronization in complex networks. *Physics reports* **469**, 93–153 (2008).

[31] Y. Kuramoto. *Chemical oscillations, waves, and turbulence* (Springer Berlin Heidelberg, 1984).

[32] S. Boccaletti, V. Latora, Y. Moreno, M. Chavez and D.-U. Hwang. Complex networks: structure and dynamics. *Physics reports* **424**, 175–308 (2006).

[33] J. A. Acebrón, L. L. Bonilla, C. J. P. Vicente, F. Ritort and R. Spigler. The kuramoto model: a simple paradigm for synchronization phenomena. *Reviews of modern physics* **77**, 137 (2005).

[34] F. Dörfler and F. Bullo. Synchronization in complex networks of phase oscillators: a survey. *Automatica* **50**, 1539–1564 (2014).

[35] F. A. Rodrigues, T. K. D. Peron, P. Ji and J. Kurths. The kuramoto model in complex networks. *Physics Reports* **610**, 1–98 (2016).

[36] S. H. Strogatz. From kuramoto to crawford: exploring the onset of synchronization in populations of coupled oscillators. *Physica D: Nonlinear Phenomena* **143**, 1–20 (2000).

[37] F. A. C. Azevedo, L. R. B. Carvalho, L. T. Grinberg, J. M. Farfel, R. E. L. Ferretti, R. E. P. Leite, R. Lent, S. Herculano-Houzel et al. Equal numbers of neuronal and nonneuronal cells make the human brain an isometrically scaled-up primate brain. *Journal of Comparative Neurology* **513**, 532–541 (2009).

[38] S. Herculano-Houzel. The human brain in numbers: a linearly scaled-up primate brain. *Frontiers in human neuroscience* **3** (2009).

[39] D. Pelvig, H. Pakkenberg, A. Stark and B. Pakkenberg. Neocortical glial cell numbers in human brains. *Neurobiology of aging* **29**, 1754–1762 (2008).

[40] P. Dayan and L. Abbott. *Theoretical neuroscience: computational and mathematical modeling of neural systems*, Computational Neuroscience (Massachusetts Institute of Technology Press, 2005).

[41] W. Gerstner and W. M. Kistler. *Spiking neuron models: single neurons, populations, plasticity* (Cambridge University Press, 2002).

[42] A. L. Hodgkin and A. F. Huxley. Resting and action potentials in single nerve fibres. *The Journal of physiology* **104**, 176–195 (1945).

[43] H. C. Tuckwell. *Introduction to theoretical neurobiology: volume 1, linear cable theory and dendritic structure* (Cambridge University Press, 1988).

[44] http://www.differencebetween.com/difference-between-chemical-and-vs-electrical-synapse/.

[45] D. O. Hebb. *The organization of behavior: a neuropsychological theory* (John Wiley And Sons, Inc., New York, 1949).

[46] M. Abeles. *Corticonics: neural circuits of the cerebral cortex* (Cambridge University Press, 1991).

[47] R. Q. Quiroga and S. Panzeri. Extracting information from neuronal populations: information theory and decoding approaches. *Nature reviews. Neuroscience* **10**, 173 (2009).

[48] E. Niedermeyer and F. L. da Silva. *Electroencephalography: basic principles, clinical applications, and related fields* (Lippincott Williams & Wilkins, 2005).

[49] H. Berger. Über das elektrenkephalogramm des menschen. *European Archives of Psychiatry and Clinical Neuroscience* **87**, 527–570 (1929).

[50] A. Grinvald and R. Hildesheim. Vsdi: a new era in functional imaging of cortical dynamics. *Nature reviews. Neuroscience* **5**, 874 (2004).

[51] M. Penttonen and G. Buzsáki. Natural logarithmic relationship between brain oscillators. *Thalamus & Related Systems* **2**, 145–152 (2003).

[52] G. Buzsáki and A. Draguhn. Neuronal oscillations in cortical networks. *Science* **304**, 1926–1929 (2004).

[53] W. Singer. Neuronal synchrony: a versatile code for the definition of relations?, *Neuron* **24**, 49–65 (1999).

[54] N Kopell, G. Ermentrout, M. Whittington and R. Traub. Gamma rhythms and beta rhythms have different synchronization properties. *Proceedings of the National Academy of Sciences* **97**, 1867–1872 (2000).

[55] A. Von Stein and J. Sarnthein. Different frequencies for different scales of cortical integration: from local gamma to long range alpha/theta synchronization. *International journal of psychophysiology* **38**, 301–313 (2000).

[56] P. Fries. A mechanism for cognitive dynamics: neuronal communication through neuronal coherence. *Trends in cognitive sciences* **9**, 474–480 (2005).

[57] F. Varela, J.-P. Lachaux, E. Rodriguez and J. Martinerie. The brainweb: phase synchronization and large-scale integration. *Nature reviews. Neuroscience* **2**, 229 (2001).

[58] R. R. Llinás. The intrinsic electrophysiological properties of mammalian neurons: insights into central nervous system function. *Science* **242**, 1654–1664 (1988).

[59] V. Shusterman and W. C. Troy. From baseline to epileptiform activity: a path to synchronized rhythmicity in large-scale neural networks. *Physical Review E* **77**, 061911 (2008).

[60] P. R. Roelfsema, A. K. Engel, W. Singer et al. Visuomotor integration is associated with zero time-lag synchronization among cortical areas. *Nature* **385**, 157 (1997).

[61] V. N. Murthy and E. E. Fetz. Oscillatory activity in sensorimotor cortex of awake monkeys: synchronization of local field potentials and relation to behavior. *Journal of neurophysiology* **76**, 3949–3967 (1996).

[62] W. H. Miltner, C. Braun, M. Arnold, H. Witte and E. Taub. Coherence of gamma-band eeg activity as a basis for associative learning. *Nature* **397**, 434 (1999).

[63] J. Sarnthein, H. Petsche, P Rappelsberger, G. Shaw and A Von Stein. Synchronization between prefrontal and posterior association cortex during human working memory. *Proceedings of the National Academy of Sciences* **95**, 7092–7096 (1998).

[64] J. Fell and N. Axmacher. The role of phase synchronization in memory processes. *Nature reviews neuroscience* **12**, 105–118 (2011).

[65] E Rodriguez, N George, J. Lachaux, J Martinerie, B Renault, F. Varela et al. Perception's shadow: long-distance synchronization of human brain activity. *Nature* **397**, 430–433 (1999).

[66] A. Engel, P Fries and W Singer. Dynamic predictions: oscillations and synchrony in top-down processing. *Nature Reviews Neuroscience* **2**, 704–716 (2001).

[67] E. A. Stern, D. Jaeger and C. J. Wilson. Membrane potential synchrony of simultaneously recorded striatal spiny neurons in vivo. *NATURE* **394**, 475 (1998).

[68] G. Buzsaki, Z. Horvath, R. Urioste, J. Hetke and K. Wise. High-frequency network oscillation in the hippocampus. *Science* **256**, 1025–1027 (1992).

[69] R. D. Traub. Fast oscillations and epilepsy. *Epilepsy currents* **3**, 77–79 (2003).

[70] P. Jiruska, M. de Curtis, J. G. Jefferys, C. A. Schevon, S. J. Schiff and K. Schindler. Synchronization and desynchronization in epilepsy: controversies and hypotheses. *The Journal of physiology* **591**, 787–797 (2013).

[71] R. E. Mirollo and S. H. Strogatz. Synchronization of pulse-coupled biological oscillators. *SIAM Journal on Applied Mathematics* **50**, 1645–1662 (1990).

[72] W. Gerstner, R. Ritz and J. L. van Hemmen. A biologically motivated and analytically soluble model of collective oscillations in the cortex. *Biological cybernetics* **68**, 363–374 (1993).

[73] C. Van Vreeswijk, L. Abbott and G. B. Ermentrout. When inhibition not excitation synchronizes neural firing. *Journal of computational neuroscience* **1**, 313–321 (1994).

[74] U Ernst, K Pawelzik and T Geisel. Synchronization induced by temporal delays in pulse-coupled oscillators. *Physical review letters* **74**, 1570 (1995).

[75] D. Golomb and J. Rinzel. Dynamics of globally coupled inhibitory neurons with heterogeneity. *Physical review E* **48**, 4810 (1993).

[76] D. Hansel, G. Mato and C. Meunier. Synchrony in excitatory neural networks. *Neural computation* **7**, 307–337 (1995).

[77] B. Ermentrout. Type i membranes, phase resetting curves, and synchrony. *Neural computation* **8**, 979–1001 (1996).

[78] M. di Volo, R. Burioni, M. Casartelli, R. Livi and A. Vezzani. Neural networks with excitatory and inhibitory components: direct and inverse problems by a mean-field approach. *Physical Review E* **93**, 012305 (2016).

[79] M. di Volo, R. Livi, S. Luccioli, A. Politi and A. Torcini. Synchronous dynamics in the presence of short-term plasticity. *Physical Review E* **87**, 032801 (2013).

[80] R. Burioni, M. Casartelli, M. Di Volo, R. Livi and A. Vezzani. Average synaptic activity and neural networks topology: a global inverse problem. *Scientific reports* **4** (2014).

[81] W. Gerstner, W. M. Kistler, R. Naud and L. Paninski. *Neuronal dynamics: from single neurons to networks and models of cognition* (Cambridge University Press, 2014).

[82] T. P. Vogels, K. Rajan and L. F. Abbott. Neural network dynamics. *Annu. Rev. Neurosci.* **28**, 357–376 (2005).

[83] O. Sporns, D. R. Chialvo, M. Kaiser and C. C. Hilgetag. Organization, development and function of complex brain networks. *Trends in cognitive sciences* **8**, 418–425 (2004).

[84] I. M. Raman, A. E. Gustafson and D. Padgett. Ionic currents and spontaneous firing in neurons isolated from the cerebellar nuclei. *Journal of Neuroscience* **20**, 9004–9016 (2000).

[85] A. L. Hodgkin and A. F. Huxley. A quantitative description of membrane current and its application to conduction and excitation in nerve. *The Journal of physiology* **117**, 500–544 (1952).

[86] P. Ashwin, S. Coombes and R. Nicks. Mathematical frameworks for oscillatory network dynamics in neuroscience. *The Journal of Mathematical Neuroscience* **6**, 2 (2016).

[87] R. FitzHugh. Impulses and physiological states in theoretical models of nerve membrane. *Biophysical journal* **1**, 445–466 (1961).

[88] J. Nagumo, S. Arimoto and S. Yoshizawa. An active pulse transmission line simulating nerve axon. *Proceedings of the IRE* **50**, 2061–2070 (1962).

[89] C. Morris and H. Lecar. Voltage oscillations in the barnacle giant muscle fiber. *Biophysical journal* **35**, 193–213 (1981).

[90] L. Lapicque. Recherches quatitatives sur l'excitation electrique des nerfs traitee comme polarisation. *J. Physiol. Pathol. Gen.* **9**, 620–635 (1907).

[91] L. F. Abbott. Lapicque's introduction of the integrate-and-fire model neuron (1907). *Brain research bulletin* **50**, 303–304 (1999).

[92] M. V. Tsodyks and H. Markram. The neural code between neocortical pyramidal neurons depends on neurotransmitter release probability. *Proceedings of the National Academy of Sciences* **94**, 719–723 (1997).

[93] L. F. Abbott, J. Varela, K. Sen and S. Nelson. Synaptic depression and cortical gain control. *Science* **275**, 221–224 (1997).

[94] M Tsodyks, K Pawelzik and H Markram. Neural networks with dynamic synapses. *Neural computation* **10**, 821 (1998).

[95] V. Volman, I. Baruchi, E. Persi and E. Ben-Jacob. Generative modelling of regulated dynamical behavior in cultured neuronal networks. *Physica A: Statistical Mechanics and its Applications* **335**, 249–278 (2004).

[96] V. Volman, I. Baruchi and E. Ben-Jacob. Manifestation of function-follow-form in cultured neuronal networks. *Physical biology* **2**, 98 (2005).

[97] E. Fuchs, A. Ayali, E. Ben-Jacob and S. Boccaletti. The formation of synchronization cliques during the development of modular neural networks. *Physical biology* **6**, 036018 (2009).

[98] F. Pittorino, M. Ibáñez-Berganza, M. di Volo, A. Vezzani and R. Burioni. Chaos and correlated avalanches in excitatory neural networks with synaptic plasticity. *Physical Review Letters* **118**, 098102 (2017).

[99] C.-C. Chen and D. Jasnow. Event-driven simulations of a plastic, spiking neural network. *Physical Review E* **84**, 031908 (2011).

[100] R. Brette. Exact simulation of integrate-and-fire models with exponential currents. *Neural Computation* **19**, 2604–2609 (2007).

[101] R. Brette. Exact simulation of integrate-and-fire models with synaptic conductances. *Neural Computation* **18**, 2004–2027 (2006).

[102] R. Brette, M. Rudolph, T. Carnevale, M. Hines, D. Beeman, J. M. Bower, M. Diesmann, A. Morrison, P. H. Goodman, F. C. Harris et al. Simulation of networks of spiking neurons: a review of tools and strategies. *Journal of computational neuroscience* **23**, 349–398 (2007).

[103] R. Zillmer, R. Livi, A. Politi and A. Torcini. Stability of the splay state in pulse-coupled networks. *Physical Review E* **76**, 046102 (2007).

[104] A. Vespignani. Modelling dynamical processes in complex socio-technical systems. *Nature physics* **8**, 32 (2012).

[105] R. Pastor-Satorras and A. Vespignani. Epidemic dynamics and endemic states in complex networks. *Physical Review E* **63**, 066117 (2001).

[106] S. N. Dorogovtsev, A. V. Goltsev and J. F. F. Mendes. Critical phenomena in complex networks. *Reviews of Modern Physics* **80**, 1275 (2008).

[107] M. Rubinov and O. Sporns. Complex network measures of brain connectivity: uses and interpretations. *Neuroimage* **52**, 1059–1069 (2010).

[108] O. Sporns and J. D. Zwi. The small world of the cerebral cortex. *Neuroinformatics* **2**, 145–162 (2004).

[109] V. M. Eguiluz, D. R. Chialvo, G. A. Cecchi, M. Baliki and A. V. Apkarian. Scale-free brain functional networks. *Physical review letters* **94**, 018102 (2005).

[110] S. Achard, R. Salvador, B. Whitcher, J. Suckling and E. Bullmore. A resilient, low-frequency, small-world human brain functional network with highly connected association cortical hubs. *Journal of Neuroscience* **26**, 63–72 (2006).

[111] O. Sporns, C. J. Honey and R. Kötter. Identification and classification of hubs in brain networks. *PloS one* **2**, e1049 (2007).

[112] B Wang, T Zhou, Z. Xiu and B. Kim. Optimal synchronizability of networks. *The European Physical Journal B-Condensed Matter and Complex Systems* **60**, 89–95 (2007).

[113] J. C. Vasquez, A. R. Houweling and P. Tiesinga. Simultaneous stability and sensitivity in model cortical networks is achieved through anti-correlations between the in-and out-degree of connectivity. *Frontiers in computational neuroscience* **7** (2013).

[114] L. R. Varshney, B. L. Chen, E. Paniagua, D. H. Hall and D. B. Chklovskii. Structural properties of the caenorhabditis elegans neuronal network. *PLoS computational biology* **7**, e1001066 (2011).

[115] E. Bertolotti, R. Burioni, M. di Volo and A. Vezzani. Synchronization and long-time memory in neural networks with inhibitory hubs and synaptic plasticity. *Physical Review E* **95**, 012308 (2017).

[116] J. Gómez-Gardeñes, Y. Moreno and A. Arenas. Synchronizability determined by coupling strengths and topology on complex networks. *Physical Review E* **75**, 066106 (2007).

[117] M. Barahona and L. M. Pecora. Synchronization in small-world systems. *Physical review letters* **89**, 054101 (2002).

[118] T. Nishikawa, A. E. Motter, Y.-C. Lai and F. C. Hoppensteadt. Heterogeneity in oscillator networks: are smaller worlds easier to synchronize?, *Physical review letters* **91**, 014101 (2003).

[119] C. C. Chow. Phase-locking in weakly heterogeneous neuronal networks. *Physica D: Nonlinear Phenomena* **118**, 343–370 (1998).

[120] I. Belykh, E. de Lange and M. Hasler. Synchronization of bursting neurons: what matters in the network topology. *Physical review letters* **94**, 188101 (2005).

[121] S. Olmi, R. Livi, A. Politi and A. Torcini. Collective oscillations in disordered neural networks. *Physical Review E* **81**, 046119 (2010).

[122] L. Tattini, S. Olmi and A. Torcini. Coherent periodic activity in excitatory erdös-renyi neural networks: the role of network connectivity. *Chaos: An Interdisciplinary Journal of Nonlinear Science* **22**, 023133 (2012).

[123] S. Luccioli, S. Olmi, A. Politi and A. Torcini. Collective dynamics in sparse networks. *Physical review letters* **109**, 138103 (2012).

[124] R. L. DeVille and C. S. Peskin. Synchrony and asynchrony for neuronal dynamics defined on complex networks. *Bulletin of mathematical biology* **74**, 769–802 (2012).

[125] A. Roxin. The role of degree distribution in shaping the dynamics in networks of sparsely connected spiking neurons. *Frontiers in computational neuroscience* **5** (2011).

[126] R. Burioni, S. Di Santo, M. di Volo and A. Vezzani. Microscopic mechanism for self-organized quasiperiodicity in random networks of nonlinear oscillators. *Physical Review E* **90**, 042918 (2014).

[127] D.-S. Lee. Synchronization transition in scale-free networks: clusters of synchrony. *Physical Review E* **72**, 026208 (2005).

[128] T. Ichinomiya. Frequency synchronization in a random oscillator network. *Physical Review E* **70**, 026116 (2004).

[129] Y. Moreno and A. F. Pacheco. Synchronization of kuramoto oscillators in scale-free networks. *EPL (Europhysics Letters)* **68**, 603 (2004).

[130] X. F. Wang and G. Chen. Synchronization in scale-free dynamical networks: robustness and fragility. *IEEE Transactions on Circuits and Systems I: Fundamental Theory and Applications* **49**, 54–62 (2002).

[131] T. Zhou, M. Zhao, G. Chen, G. Yan and B.-H. Wang. Phase synchronization on scale-free networks with community structure. *Physics letters A* **368**, 431–434 (2007).

[132] C. Batista, A. Batista, J. De Pontes, R. Viana and S. Lopes. Chaotic phase synchronization in scale-free networks of bursting neurons. *Physical Review E* **76**, 016218 (2007).

[133] I Sendiña-Nadal, I Leyva, A Navas, J. Villacorta-Atienza, J. Almendral, Z Wang and S Boccaletti. Effects of degree correlations on the explosive synchronization of scale-free networks. *Physical Review E* **91**, 032811 (2015).

[134] J. Gómez-Gardeñes, S. Gómez, A. Arenas and Y. Moreno. Explosive synchronization transitions in scale-free networks. *Physical review letters* **106**, 128701 (2011).

[135] T. K. D. Peron and F. A. Rodrigues. Determination of the critical coupling of explosive synchronization transitions in scale-free networks by mean-field approximations. *Physical Review E* **86**, 056108 (2012).

[136] M. Aldana and H. Larralde. Phase transitions in scale-free neural networks: departure from the standard mean-field universality class. *Physical Review E* **70**, 066130 (2004).

[137] K. Huang. Statistical mechanics, 2nd. *Edition (New York: John Wiley & Sons)* (1987).

[138] N. A. Crossley, A. Mechelli, J. Scott, F. Carletti, P. T. Fox, P. McGuire and E. T. Bullmore. The hubs of the human connectome are generally implicated in the anatomy of brain disorders. *Brain* **137**, 2382–2395 (2014).

[139] M. De Domenico, S. Sasai and A. Arenas. Mapping multiplex hubs in human functional brain networks. *Frontiers in neuroscience* **10** (2016).

[140] T. Klausberger and P. Somogyi. Neuronal diversity and temporal dynamics: the unity of hippocampal circuit operations. *Science* **321**, 53–57 (2008).

[141] J. DeFelipe. Cortical interneurons: from cajal to 2001. *Progress in brain research* **136**, 215–238 (2002).

[142] S. Lefort, C. Tomm, J.-C. F. Sarria and C. C. Petersen. The excitatory neuronal network of the c2 barrel column in mouse primary somatosensory cortex. *Neuron* **61**, 301–316 (2009).

[143] L. J. Borg-Graham, C. Monier and Y. Fregnac. Visual input evokes transient and strong shunting inhibition in visual cortical neurons. *Nature* **393**, 369–373 (1998).

[144] I. Cohen and R. Miles. Contributions of intrinsic and synaptic activities to the generation of neuronal discharges in in vitro hippocampus. *The Journal of physiology* **524**, 485–502 (2000).

[145] V. Capano, H. J. Herrmann and L. De Arcangelis. Optimal percentage of inhibitory synapses in multi-task learning. *Scientific reports* **5** (2015).

[146] C. Börgers and N. Kopell. Synchronization in networks of excitatory and inhibitory neurons with sparse, random connectivity. *Neural computation* **15**, 509–538 (2003).

[147] N. Brunel. Dynamics of sparsely connected networks of excitatory and inhibitory spiking neurons. *Journal of computational neuroscience* **8**, 183–208 (2000).

[148] S. Ostojic. Two types of asynchronous activity in networks of excitatory and inhibitory spiking neurons. *Nature neuroscience* **17**, 594–600 (2014).

[149] D. Angulo-Garcia, S. Luccioli, S. Olmi and A. Torcini. Death and rebirth of neural activity in sparse inhibitory networks. *arXiv preprint arXiv:1610.07181* (2016).

[150] P. Bonifazi, M. Goldin, M. A. Picardo, I. Jorquera, A Cattani, G. Bianconi, A. Represa, Y. Ben-Ari and R. Cossart. Gabaergic hub neurons orchestrate synchrony in developing hippocampal networks. *Science* **326**, 1419–1424 (2009).

[151] P. P. Quilichini, M. Le Van Quyen, A. Ivanov, D. A. Turner, A. Carabalona, H. Gozlan, M. Esclapez and C. Bernard. Hub gaba neurons mediate gamma-frequency oscillations at ictal-like event onset in the immature hippocampus. *Neuron* **74**, 57–64 (2012).

[152] M. A. Picardo, P. Guigue, P. Bonifazi, R. Batista-Brito, C. Allene, A. Ribas, G. Fishell, A. Baude and R. Cossart. Pioneer gaba cells comprise a subpopulation of hub neurons in the developing hippocampus. *Neuron* **71**, 695–709 (2011).

[153] O. Yizhar, L. E. Fenno, M. Prigge, F. Schneider, T. J. Davidson, D. J. O'Shea, V. S. Sohal, I. Goshen, J. Finkelstein, J. T. Paz et al. Neocortical excitation/inhibition balance in information processing and social dysfunction. *Nature* **477**, 171–178 (2011).

[154] A. Morrison, A. Aertsen and M. Diesmann. Spike-timing-dependent plasticity in balanced random networks. *Neural computation* **19**, 1437–1467 (2007).

[155] C. Van Vreeswijk, H. Sompolinsky et al. Chaos in neuronal networks with balanced excitatory and inhibitory activity. *Science* **274**, 1724–1726 (1996).

[156] Y. Roudi and P. E. Latham. A balanced memory network. *PLoS computational biology* **3**, e141 (2007).

[157] S. L. Hill and A. E. Villa. Dynamic transitions in global network activity influenced by the balance of excitation and inhibition. *Network: Computation in Neural Systems* **8**, 165–184 (1997).

[158] D. Malagarriga, A. E. Villa, J. Garcia-Ojalvo and A. J. Pons. Mesoscopic segregation of excitation and inhibition in a brain network model. *PLoS computational biology* **11**, e1004007 (2015).

[159] F. Váša, M. Shanahan, P. J. Hellyer, G. Scott, J. Cabral and R. Leech. Effects of lesions on synchrony and metastability in cortical networks. *Neuroimage* **118**, 456–467 (2015).

[160] O. Mazor and G. Laurent. Transient dynamics versus fixed points in odor representations by locust antennal lobe projection neurons. *Neuron* **48**, 661–673 (2005).

[161] R. W. Friedrich and G. Laurent. Dynamic optimization of odor representations by slow temporal patterning of mitral cell activity. *Science* **291**, 889–894 (2001).

[162] C. M. Gray, P. König, A. K. Engel and W. Singer. Oscillatory responses in cat visual cortex exhibit inter-columnar synchronization which reflects global stimulus properties. *Nature* **338**, 334–337 (1989).

[163] M. Stopfer, S. Bhagavan, B. H. Smith and G. Laurent. Impaired odour discrimination on desynchronization of odour-encoding neural assemblies. *Nature* **390**, 70–74 (1997).

[164] P. N. Steinmetz, A Roy, P. Fitzgerald, S. Hsiao, K. Johnson and E. Niebur. Attention modulates synchronized neuronal firing in primate somatosensory cortex. *Nature* **404**, 187–190 (2000).

[165] P. W. Anderson. More is different. *Science* **177**, 393–396 (1972).

[166] R. Albert and A.-L. Barabási. Statistical mechanics of complex networks. *Reviews of modern physics* **74**, 47 (2002).

[167] S. H. Strogatz. Exploring complex networks. *nature* **410**, 268 (2001).

[168] M. E. Newman. The structure and function of complex networks. *SIAM review* **45**, 167–256 (2003).

[169] S. N. Dorogovtsev and J. F. F. Mendes. Evolution of networks. *Advances in physics* **51**, 1079–1187 (2002).

[170] M. Barthélemy, A. Barrat, R. Pastor-Satorras and A. Vespignani. Characterization and modeling of weighted networks. *Physica a: Statistical mechanics and its applications* **346**, 34–43 (2005).

[171] M. Barthélemy. Spatial networks. *Physics Reports* **499**, 1–101 (2011).

[172] P. Erdös and A. Rényi. On random graphs. *Publicationes Mathematicae Debrecen* **6**, 290–297 (1959).

[173] E. A. Bender and E. R. Canfield. The asymptotic number of labeled graphs with given degree sequences. *Journal of Combinatorial Theory, Series A* **24**, 296–307 (1978).

[174] M. Molloy and B. Reed. A critical point for random graphs with a given degree sequence. *Random structures & algorithms* **6**, 161–180 (1995).

[175] S. Bornholdt and H. G. Schuster. *Handbook of graphs and networks: from the genome to the internet* (John Wiley & Sons, 2006).

[176] D. J. Watts and S. H. Strogatz. Collective dynamics of'small-world'networks. *nature* **393**, 440 (1998).

[177] A.-L. Barabási and R. Albert. Emergence of scaling in random networks. *science* **286**, 509–512 (1999).

[178] A.-L. Barabási, R. Albert and H. Jeong. Mean-field theory for scale-free random networks. *Physica A: Statistical Mechanics and its Applications* **272**, 173–187 (1999).

[179] N. Kopell and G. Ermentrout. Symmetry and phaselocking in chains of weakly coupled oscillators. *Communications on Pure and Applied Mathematics* **39**, 623–660 (1986).

[180] H. Daido. Intrinsic fluctuations and a phase transition in a class of large populations of interacting oscillators. *Journal of Statistical Physics* **60**, 753–800 (1990).

[181] Y. Kuramoto and I. Nishikawa. Statistical macrodynamics of large dynamical systems. case of a phase transition in oscillator communities. *Journal of Statistical Physics* **49**, 569–605 (1987).

[182] H. Hong, M.-Y. Choi and B. J. Kim. Synchronization on small-world networks. *Physical Review E* **65**, 026139 (2002).

Acknowledgements

Se qualcuno mi avesse svelato dove sarei arrivata il giorno che decisi di studiare Fisica, le belle sfide che mi avrebbe presentato questo percorso e le grandi soddisfazioni che ne avrei avuto, probabilmente non ci avrei creduto. Ed ora eccomi qui, alla fine di questo Dottorato, con un piccolo bagaglio di esperienze portate a buon fine e con tanti progetti ancora in testa.

Tante sono le persone che negli anni ho incrociato sulla mia strada e che desidero ringraziare. In primo luogo il mio supervisore, il Dott. Alessandro Vezzani, per essere sempre stato presente e per i preziosi suggerimenti che ha saputo darmi. Insieme a lui, ringrazio la Prof.ssa Raffaella Burioni e il Dott. Matteo di Volo, per la loro esperienza e per il loro entusiasmo.

Desidero rivolgere un ringraziamento anche al coordinatore del Corso di Dottorato, il Prof. Cristiano Viappiani, e alla Prof.ssa Stefania Abbruzzetti, per la bella collaborazione che si è creata nell'ambito di alcune attività di divulgazione scientifica e di sostegno alla didattica svolte durante il mio percorso.

Infine, ringrazio gli amici che ho conosciuto in questi anni a Parma all'interno dell'università e gli amici che conosco da sempre, anche se il grazie più importante va alla mia famiglia, il cui affetto e sostegno sono stati il mio vero punto di forza e, ne sono certa, continueranno ad essere sempre un porto sicuro per il mio futuro.